



UNIVERSITÀ DEGLI STUDI DI MILANO
FACOLTÀ DI SCIENZE MATEMATICHE, FISICHE E
NATURALI
DOTTORATO DI RICERCA IN FISICA, ASTROFISICA E
FISICA APPLICATA

Corrugated feed-horn arrays for future CMB polarization experiments

Settore Scientifico disciplinare FIS/01

Coordinatore: Prof. Marco BERSANELLI

Tutore: Prof. Marco BERSANELLI

Co-Tutore: Dott. Fabrizio VILLA

Tesi di dottorato di:

Francesco DEL TORTO

Ciclo XXIV

Anno Accademico 2011-2012

To my parents

Introduction

The actual most corroborated model of modern cosmology is the “Hot Big Bang Model”, that results in agree with the cosmological scientific discoveries of the last 50 years. The main observational pillars that support the model are: the discovery by Edwin Hubble of the expansion of the Universe, the abundances of the primordial elements and the discovery of the Cosmic Microwave Background (CMB) radiation.

In 1929 Edwin Hubble discovered the linear relationship in distant galaxies between their distance and recession velocity: $v = Hd$. The current value for the Hubble constant is known with very high precision as 72 ± 8 Km/sec/Mpc [1], from the measurements obtained by the Hubble Space Telescope on even far distant galaxies w.r.t. to the Hubble measurements.

According to the Hot Big Bang Model, in the first era of its life, the Universe was constituted by photons, electrons and protons. During this time the firsts primordial elements were produced, i.e. Helium, Deuterium, and Beryllium. The abundances of the primordial elements can be calculated with precision by the Hot Big Bang Model, resulting in good agreement with the measured abundances [2], [3].

In 1965 Arno Penzias and Robert Wilson discovered the CMB, already predicted in 1948 by George Gamow in the framework of an Hot Big Bang Model. Forty-five years after its discovery, the CMB radiation is today a very powerful tool of cosmological investigation. We can say, at present, that about fifty percent of all possible informations are extracted from the CMB.

The CMB is characterized by a black-body spectrum, with temperature anisotropies on the sky at a level of $\Delta T/T \sim 10^{-5}$, on angular scales from 180° to about $5'$. Several cosmological parameters can be extracted from the angular temperature anisotropies: the Hubble constant H_0 , the total energy density of the Universe Ω_0 and the energy associated to the cosmological constant Ω_Λ that describes the expansion of the Universe. For the discovery of the CMB temperature anisotropies, John Mather received in 2006 the Nobel Prize for Physics.

Since there exist degeneracies in parameters, it is not possible to extract all cosmological parameters from temperature anisotropies. Different combinations of cosmological parameters (ie cosmological models) can indeed be extracted by the same temperature anisotropies pattern. These parameters are called degenerated. Degeneracy can be removed by measuring the CMB polarization.

The polarization also allows to know the epoch of re-ionization of the Universe, probably caused by the ignition of the first stars. Moreover the polarization allows to study the *inflationary* (exponential expansion) era of the Universe occurred after the Big Bang. The inflation would have stretched the primordial quantum perturbations that gave rise, by means of the anisotropies, to the actual large scale structures. CMB polarization enables the measurements of the intensity and of the characteristics of these primordial perturbations. In particular can be measured the ratio of tensor-to-scalar T/S perturbations, where the tensor perturbations would be the smoking gun of a cosmological background of *gravitational waves*. Moreover the ratio T/S , is related to the energy scale of the inflation, occurred just $\sim 10^{-34}$ seconds after the Big Bang [14]. The energy scale of the inflation is predicted at a level of 10^{16} GeV, far beyond the level that any particle accelerator on Earth will ever reach.

The CMB is just partially polarized, in an amount $\leq 10\%$, corresponding to a signal of a fraction of μK . The measurements of the CMB polarization is then very difficult and actually at the beginning [4, 5], requiring great technological efforts for the next generation experiments. The measurements of a so faint signal calls for extremely high instrumental sensitivities, achievable with a precise control of systematics and a great number of receivers.

Part of each receiver is the horn antenna that match the detector with the sky or an external optics. The need for a great number of receivers implies also a great number of antennas. In this work I have optimized the “platelet” technique to realize, in a cost and time effective manner, big arrays of *corrugated feed-horn* antennas for future CMB polarization experiments.

The platelet technique consists in the overlap of properly machined metal sheets so that the feed-horn is realized in layers. This method is relatively cheap, with a cost saving of about 90% with respect to the more classical electroforming technique. Moreover the platelet technique allows quick manufacturing of feed-horn arrays by drilling several holes in each plate. A complete corrugation, with a tooth and a groove, can be obtained in each plate, minimizing the number of plates. A curve focal surface can be obtained with a series of modules properly tilted to reproduce the required surface.

In this work I have realized a prototype of module, composed by seven corrugated -dual profiled- feed-horns in W band (75-110 GHz). The mod-

ule is designed for compactness, light-weight, reliability in space conditions and for high electromagnetic performance. The prototype was tested for electromagnetic performances (return loss and beam pattern) in standard conditions, resulting with good performance and in a satisfactory agreement with the relative numerical simulation. Moreover simulated mechanical, vibrational and thermal performance show good results, indicating a possible space readiness for the prototype and the technology.

The design of the realized prototype will be applied for the realization of the focal plane of the STRIP instrument on board of the ASI-LSPE experiment. The LSPE experiments is planned to measure the CMB polarization during a long-duration night flight over the Arctic Polar Circle in winter 2014-2015, with a sensitivity better then Planck in the range $\sim 20 < \ell < \sim 100$.

Contents

Introduction	i
1 Origin e Characteristics of the CMB	3
1.1 Spectrum	3
1.2 Temperature Anisotropies	4
1.3 Polarization	7
2 CMB Polarization Anisotropy	11
2.1 Why the CMB is Polarized	11
2.2 Scalar, Vector and Tensor perturbations	12
2.3 Electric and Magnetic Modes	16
2.3.1 Parity	17
2.3.2 Modulation	18
2.3.3 Correlation with temperature fluctuation	19
2.4 Polarization Power spectra	21
2.5 What the CMB polarization tell us	22
3 Polarization Experiments	25
3.1 Requirements	25
3.1.1 Environment	26
3.1.2 Angular resolution	26
3.1.3 Foregrounds	26
3.1.4 Systematic effects	27
3.1.5 Sensitivity	27
3.2 Experimental setup and technologies	28
3.2.1 Detectors	28
3.2.2 Optics	31
3.3 Were we are	32
3.4 Future experiments	34

4	High performance corrugated feed-horn arrays	37
4.1	Feed-horn characteristic	37
4.1.1	Beam pattern	37
4.1.2	Insertion Loss and Return Loss	42
4.1.3	Bandwidth	43
4.2	Corrugated feed-horn	44
4.3	Specifications for high performance feed-horns arrays	47
4.3.1	Electromagnetic requirements of high performance feed-horns	48
4.3.2	Mechanical requirements for high-performance feed-horn arrays	49
4.3.3	Fabrication techniques for feed-horn arrays	50
5	A non-bonded platelet feed-horn array	55
5.1	Electromagnetic design	55
5.1.1	Rules of thumb	56
5.1.2	Simulation of performance	58
5.2	Mechanical design	59
5.2.1	Materials	63
5.2.2	Design of the plates	64
5.2.3	Design optimization	66
5.3	Fabrication	71
5.3.1	Assembling	74
5.4	Electromagnetic Tests	76
5.4.1	Beam pattern	78
5.4.2	Return Loss	90
6	Conclusions	97
	Bibliografy	104

Chapter 1

Origin e Characteristics of the CMB

The CMB originates from the decoupling of matter and radiation, occurred when the temperature of the expanding Universe fell below 3000 K. At this temperature the plasma constituting the Universe could combine into neutral hydrogen, thus reducing the Thomson scattering cross section and letting the radiation propagate freely.

The photons of the CMB appear to come from a surface in the sky called **Last Scattering Surface**, placed at a distance of 13.7 billion of light years, equal to the distance traveled by the photons in the time since their release.

1.1 Spectrum

Before decoupling, the completely ionized Universe has gone through a period of thermal equilibrium, during which the CMB has become a black body spectrum. The expansion of the Universe did not change the shape of the spectrum, but the temperature has decreased in proportion to the redshift:

$$T \propto 1 + z$$

with $z_{CMB} \sim 1000$. The (cosmological) redshift consists of an increment of the wavelength of the photons, caused by the expansion of the space-time ie of the Universe and it is defined as:

$$z = \frac{\Delta\lambda}{\lambda_e}$$

with $\Delta\lambda$ being the difference between the observed and emitted wavelength λ_e . For this reason today we observe the CMB photons at the microwave frequencies.

The spectrum of the CMB has been fully measured for the first time by the FIRAS (Far Infrared Absolute Spectrophotometer) instrument on board of the COBE (Cosmic Background Explorer) satellite, launched in 1989. The measured spectrum is highly consistent with a blackbody at a temperature of $2,725 \pm 0.002\text{K}$ [7], as shown in Figure 1.1. This is the most precise measurement ever made of a blackbody, and its temperature is today the cosmological parameters known with the higher precision.

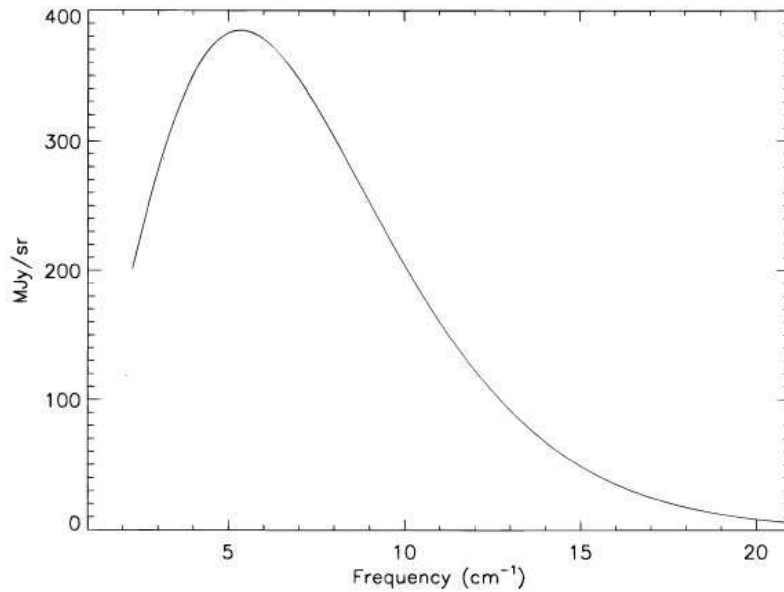


Figure 1.1: Measurement of the CMB spectrum with the blackbody best-fit. The theoretical curve is superimposed on the measurements, with error bars smaller than the curve thickness. [6]

1.2 Temperature Anisotropies

The CMB is highly isotropic. The first anisotropy level is at $\Delta T/T \sim 10^{-3}$. This is an anisotropy between two specific points of the sky displaced at

180 degrees each other and it is called “dipole anisotropy”. This is not an intrinsic anisotropy, but is generated by the peculiar motion of the Solar System with respect to the flux of the CMB photons.

The first intrinsic anisotropies are at a level $\Delta T/T \sim 10^{-5}$, on angular scales from 180 degrees to about $5'$. These anisotropies are the “footprint” left by the primordial quantum fluctuations of the energy density of the Universe. These fluctuations were then brought to the cosmic scales by a period of exponential expansion, the “inflation”, giving rise by gravitational instability to the current structures of the Universe.

The fluctuations of the energy density correspond to fluctuations in the gravitational field that causes compression and rarefaction of the photo-baryon fluid. Compression is opposed by the fluid pressure generated by photons. The opposition between gravity and radiation pressure generates acoustic oscillations in the primordial plasma. The CMB temperature is locally higher where the acoustic oscillations compress the fluid, while the regions where the fluid is rarefied found to have a lower temperature. The k different modes of oscillation propagate independently at the speed of sound c_s in the photo-baryon fluid with frequency $\omega = kc_s$.

At the recombination, matter and radiation are decoupled and the acoustic oscillations end, leaving their traces in the CMB photons temperature. In particular, the modes that at the recombination reaches the extremes of oscillations, originate higher temperature fluctuations. The angular anisotropies result from the projection on the celestial sphere of the spatial inhomogeneities of temperature in the photo-baryon fluid. These angular anisotropies are now detectable because the photons have traveled almost undisturbed up to us.

The anisotropies are described on the celestial sphere as combination of spherical harmonics:

$$\frac{\Delta T}{T}(\theta, \phi) = \sum_{\ell, m} a_{\ell, m} Y_{\ell}^m(\theta, \phi), \quad (1.1)$$

and, for example, the “dipole” is described by the second spherical harmonics ($\ell=1$).

If the fluctuations are a random variable, gaussian distributed, then all the informations on the anisotropies are given by the two-points auto-correlation function of the fluctuations:

$$C(\theta) \equiv \left\langle \frac{\Delta T(x)}{T_{cmb}} \frac{\Delta T(x')}{T_{cmb}} \right\rangle \quad (1.2)$$

where the mean is evaluated over all the couples of points in the sky with directions x, x' such that $x \cdot x' = \cos \theta$. As seen above, the function 1.2 can be expanded in Legendre polynomials:

$$C(\theta) = \frac{1}{4\pi} \sum_{\ell} C_{\ell} P_{\ell}(\cos \theta), \quad (1.3)$$

where the information is “contained” in the coefficients C_{ℓ} given by:

$$C_{\ell} = \langle |a_{\ell,m}|^2 \rangle = \frac{1}{2\ell + 1} \sum_{- \ell}^{\ell} |a_{\ell,m}|^2 \quad (1.4)$$

and forming the *Angular Power Spectrum*. The power spectrum indicates the amplitude of the different spherical harmonics, associated to different angular scales or multipole orders $\ell = \pi/\theta$, where θ is the angular scale of the anisotropy. As an example the dipole anisotropy occurs at $\theta = \pi$, ie $\ell=1$.

The power spectrum exhibits peaks that are directly related to the modes of acoustic oscillations that have reached their extremes at recombination. In fact, there are particular modes in which the wavenumber $k = 2\pi/\lambda$ is an integer multiple of the sound horizon (s^*), given by the ratio between π and the distance traveled by the sound before the recombination. The mode with $k_1 = \pi/s^*$ had time to compress once and corresponds to the first peak of the power spectrum. The second peak is related to the mode for which $k_2 = 2k_1$ that oscillates at twice the frequency; it had the time of compression and rarefaction (Figure 1.2). The third peak with $k_3 = 3k_1$ performed a compression, rarefaction and a new compression. The peaks are then harmonics of the fundamental scale given by the distance traveled by the sound before recombination.

The peaks of the power spectrum are closely related to the initial physical conditions of the primordial photo-baryon fluid. In particular, the peaks depend on the energy density and on the amount of baryons and matter (dark and visible) that drive the acoustic oscillations. From the peaks of the power spectrum can be derived some fundamental cosmological parameters such as the total energy density Ω_0 (first peak), the baryon matter density Ω_B (second peak), the dark matter density Ω_m (third peak) and the density associated with the cosmological constant Ω_{Λ} , also known as dark energy.

The still ongoing mission WMAP [10, 11, 24] is now making a major contribution to the reconstruction of the power spectrum and then to the estimation of cosmological parameters. The third generation satellite Planck,

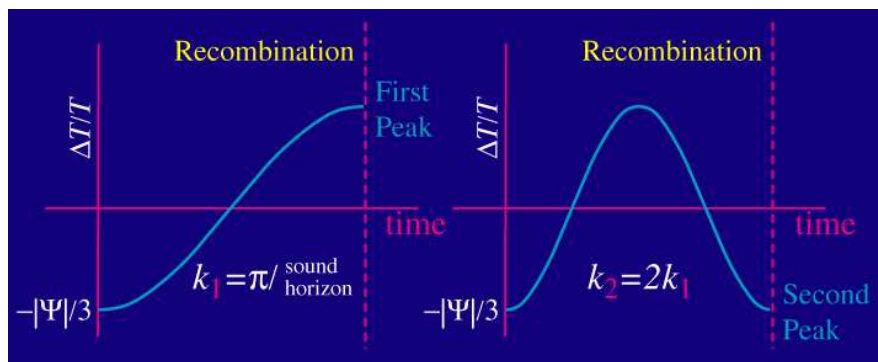


Figure 1.2: Oscillation of the temperature fluctuations. Is there a particular mode (k_1) for which the fluid has had time for a single compression before the recombination. The wavenumber ($2\pi/\lambda$) of such mode k_1 is π/s^* , where s^* is the distance traveled by the sound before the recombination [8].

also ongoing, will measure the power spectrum with even more precision, thanks to a sensitivity of $\sim 1\mu K$, and up to multipoles order $\ell \sim 2500$ thanks to the high angular resolution, that for the cosmological channels reaches $9'$. Planck will give definitive measurements, with an uncertainty of a few percent, limited only by the contributions of “foregrounds” (Galaxy, interstellar dust, synchrotron emission) and by the so-called “cosmic variance”. The cosmic variance is the maximum precision with which the power spectrum can be measured and is given by:

$$\delta C_\ell = \sqrt{\frac{2}{2\ell + 1}} C_\ell. \quad (1.5)$$

Each C_ℓ is evaluated as a mean of a limited number ($2\ell + 1$) of samples $a_{\ell,m}$, because the Universe is observed from a single point. To reduce the cosmic variance would be necessary more observation points separated by cosmological distances.

1.3 Polarization

Another important feature of the CMB is its polarization, which represents the new frontier of the CMB observation. Before we describe the polarization of the CMB is useful to recall the general description of the polarization.

Generally an electromagnetic wave can be described in terms of its electric field:

$$E = E_x + E_y \quad (1.6)$$

with:

$$E_x = E_{x0} e^{i(kz - \omega t + \phi_x)} \quad (1.7)$$

$$E_y = E_{y0} e^{i(kz - \omega t + \phi_y)} \quad (1.8)$$

and x e y that indicate the directions transverse to that of propagation. The polarization of an electromagnetic wave can be described by the *Stokes Parameters*:

$$I = \langle E_{x0}^2 + E_{y0}^2 \rangle \quad (1.9)$$

$$Q = \langle E_{x0}^2 - E_{y0}^2 \rangle \quad (1.10)$$

$$U = 2 \langle E_{x0} E_{y0} \cos(\phi_x - \phi_y) \rangle \quad (1.11)$$

$$V = 2 \langle E_{x0} E_{y0} \sin(\phi_x - \phi_y) \rangle \quad (1.12)$$

were the brackets $\langle \dots \rangle$ indicate the time average over periods far greater than the frequency of the wave ω . The I parameter gives the total intensity, Q indicates the preponderance of polarization along x than along y and U e V give the phase information. The total polarization of a wave is:

$$P = \sqrt{Q^2 + U^2 + V^2} \quad (1.13)$$

and the direction of polarization is identified by

$$\alpha = \frac{1}{2} \tan^{-1} \frac{U}{Q}. \quad (1.14)$$

If the wave is completely polarized $P = I$, then the partial polarization is

$$\Pi \equiv \frac{P}{I}.$$

The Stokes parameters are scalars, then the polarization can be described by a vector without way, with length corresponding to the polarization intensity

and with direction that indicates the axis where the polarization is stronger. On the plane perpendicular to the propagating direction, the intensity of the wave can be decomposed as:

$$I_{ij} = \begin{pmatrix} T + Q & U - iV \\ U + iV & T - Q \end{pmatrix} \quad (1.15)$$

where, in our case, T is the CMB temperature and Q e U indicate the polarization (as discussed in the next chapter V is expected to be null.)

The precise measurements of the CMB polarization (ie its Stokes parameters), as it will be described in the next chapters, requires hundreds of polarimeters coupled with high performance optics. This Thesis addresses the experimental issue, in CMB polarization observation, relative to the realization of high performance corrugated feed horns that constitute one of the main optical subsystem of CMB polarization experiment.

Chapter 2

CMB Polarization Anisotropy

2.1 Why the CMB is Polarized

The CMB photons are polarized because of Thomson scattering with the free electrons of the photo-baryon fluid at the recombination era.

The cross-section of the Thomson scattering depends from the polarization of the incident radiation as:

$$\frac{d\sigma_T}{d\Omega} \propto |\hat{\epsilon} \cdot \hat{\epsilon}'|, \quad (2.1)$$

where $\hat{\epsilon}'$ is the incident polarization and $\hat{\epsilon}$ is the scattered polarization. The scattered radiation intensity peaks in the direction orthogonal to, and with polarization parallel to, the incident polarization, as in Figure 2.1.

If the incident radiation is isotropic, the scattered radiation results not polarized because orthogonal polarization from incident direction separated by 90° would balance. To give rise to linear polarization is necessary that the incident polarization is non isotropic, in particular it is necessary a quadrupolar anisotropy, as shown in Figure 2.1.

However a rapid Thomson scattering, because of randomization of photon direction, would destroy any quadrupole anisotropy and polarization. The CMB polarized photons are then the *last* scattered, and they reflect the *quadrupolar* temperature fluctuations at the Last Scattering Surface. Decomposing the incident radiation in spherical harmonics $Y_l^m(\theta, \phi)$, the quadrupole moments are represented by $l = 2$, $m = 0, \pm 1, \pm 2$ and no other moments exists that can generate polarization via Thomson scattering (Figure 2.2).

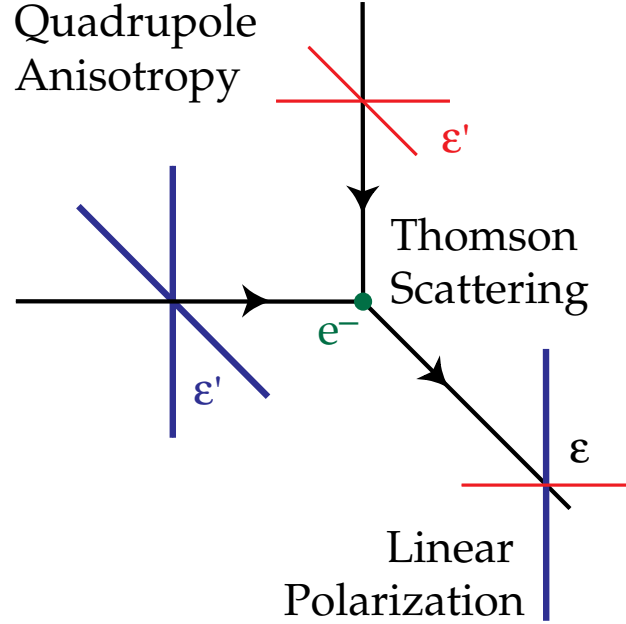


Figure 2.1: The Thomson scattering of a quadrupolar anisotropy radiation give rise to a linear polarized radiation. The polarization components that pass the Thomson scattering are only those orthogonal to the scattering direction. The superimposition of an hot (blue) radiation with a cold (red) radiation, scattering at 90 degrees (quadrupole), give rise a radiation with different intensities on the two directions orthogonal to the scattering direction. The scattered radiation is then linearly polarized.

2.2 Scalar, Vector and Tensor perturbations

From the CMB polarization can be extracted informations on the different sources of quadrupolar temperature perturbations. The three quadrupolar moments match with the three different sources of temperature fluctuations: scalar ($m = 0$), vector ($m = \pm 1$) and tensor ($m = \pm 2$). (Figure 2.2).

The scalar perturbations are energy density fluctuations, due to acoustic oscillations of the photo-baryon fluid. A single Fourier component of the density perturbations, corresponds to a single plane wave of acoustic oscillation and then in the temperature perturbations. The combination of temperature and gravitational potential Ψ results in an *effective* temperature:

$$(\Delta T/T)_{eff} = \Delta T/T + \Psi.$$

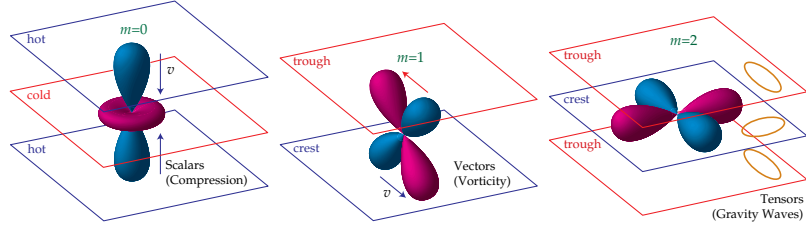


Figure 2.2: The quadrupolar temperature perturbations have three distinct sources: scalar ($m = 0$) due to fluid compression, vector ($m = \pm 1$) due to vortex motions and tensor ($m = \pm 2$) originated from gravitational waves. The orthogonality of the spherical harmonics guarantees that no other source of quadrupole anisotropy exists that can generate polarization via Thomson scattering. [8]

Gradients of *effective* temperature create flows from hot to cold *effective* temperature regions.

The photon flux from effective hot regions towards effective cold regions produces a dipole moment in the direction \hat{k} of the acoustic plane wave. An observer in the trough of a plane wave sees hot photons flowing from the crest towards the trough with $\mathbf{v} \parallel \mathbf{k}$, and cold photons that surrounding. The temperature pattern has then a quadrupole distribution with $m = 0$ [8](Figure 2.3):

$$Y_2^0 \propto 3 \cos^2 \theta - 1 \quad (2.2)$$

where $\cos \theta = \hat{n} \cdot \hat{k}$ and \hat{n} is the line of sight in the spherical harmonics coordinate system.

In the crests the effect is opposite, with the hot photons flowing towards the troughs and the cold photons surrounding the observer. In this case the quadrupole is reversed but with the same nature $m = 0$. The total effect is a quadrupole modulated by a plane wave:

$$-Y_2^0(\hat{n})e^{i(\mathbf{k} \cdot \mathbf{x})}, \quad (2.3)$$

where the sign indicates the flow from hot regions towards cold ones [8].

Recalling that in the Thomson scattering the outgoing polarization depends from the scattering direction as in [2.1], with the maximum in the direction orthogonal to the temperature variation, the orientation of the quadrupole (ie \hat{k}) determines the polarization pattern. Considering the plane passing at the center of the quadrupole anisotropy and orthogonal to the line of light direction \hat{n} , and recalling that the outgoing polarization is always oriented with the cold lobe of the quadrupole, the polarization is maximum when

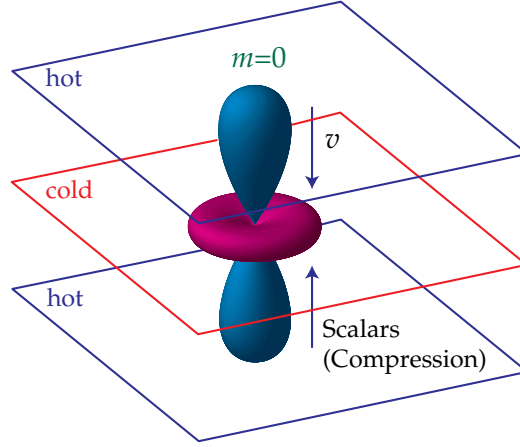


Figure 2.3: Scalar quadrupole moment ($l = 2, m = 0$). An observer in the trough of a plane wave sees hot photons flowing from the crest towards the trough with $\mathbf{v} \parallel \mathbf{k}$ and cold photons that surrounding [8].

the lobes of the quadrupole lie on this plane defined by $\hat{e}_\theta \otimes \hat{e}_\phi$. The scalar polarization pattern then varies with θ with no polarization at $\theta = 0, \theta = \pi$ and a maximum polarization at $\theta = \pi/2$ (Figure 2.4).

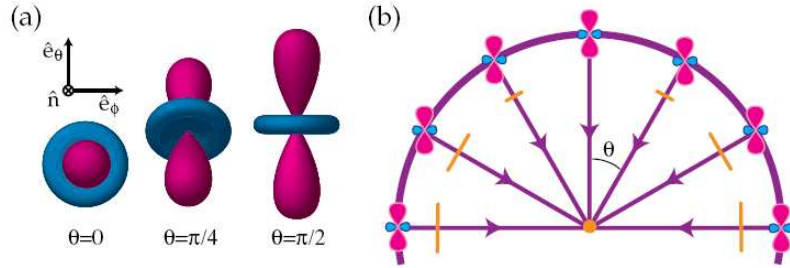


Figure 2.4: Projection of the polarization generated by the scalar quadrupole anisotropy. (a) The direction of the quadrupole moment with respect to the line of sight \hat{n} determines the direction and intensity of the polarization. The polarization lies on the tangential plane $\hat{e}_\theta \otimes \hat{e}_\phi$ projected by the cold (red) lobe of the quadrupole anisotropy. (b) In spherical coordinates with $\hat{n} \cdot \hat{k} = \cos \theta$, the polarization is oriented in the N-S direction (Q) with amplitude modulated as $\sin^2 \theta$. [8]

In spherical coordinates relative to \hat{k} , with the North pole at $\theta = 0$, the polarization oriented in the North-South (E-W) direction is described by

$Q > 0$ ($Q < 0$) and a polarization in direction NE-SW (NW-SE) is described by $U > 0$ ($U < 0$). The pattern in Figure 2.4b is then a pure Q pattern, modulated in amplitude by θ :

$$Q = \sin^2 \theta \quad U = 0$$

The polarization pattern originated by scalar perturbation modes is shown in Figure 2.5. The scalar perturbations are the unique that give rise to the

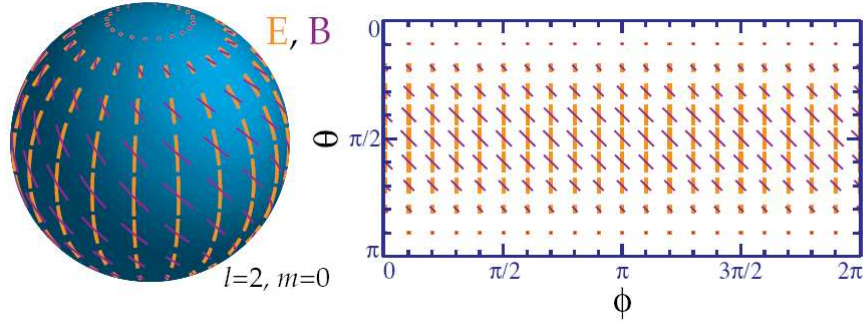


Figure 2.5: Polarization pattern originated by scalar perturbation ($l = 2, m = 0$) with azimuthal symmetry. The scalar perturbations generate a pure Q pattern (yellow), its rotation of 45° represents a pure U pattern (purple). [8]

formation of large scale structure in the Universe by gravitational instability.

The vector perturbations arise from the Doppler effect of the fluid that moves in vortices with velocity $v \perp \mathbf{k}$. There is no associated density perturbation and are expected to be absent in CMB polarization.

A quadrupolar anisotropy can also be generated by a plane gravitational wave that distorts the space-time anisotropically in the plane of the perturbation, causing a wavelength shift of the photons. The photons wavelength distortion produces a quadrupolar $m = \pm 2$ temperature anisotropy:

$$Y_2^{\pm 2} \propto \sin^2 \theta e^{\pm 2i\phi} \quad (2.4)$$

in the spherical coordinate system with $\hat{z} \parallel \hat{k}$.

The polarization pattern is given by the Thomson scattering of the quadrupole anisotropy. At $\theta = \pi/2$ the quadrupole intersects the tangential plane $\hat{e}_\theta \otimes \hat{e}_\phi$ with the lobes that cross the plane in the \hat{e}_ϕ direction as ϕ varies.

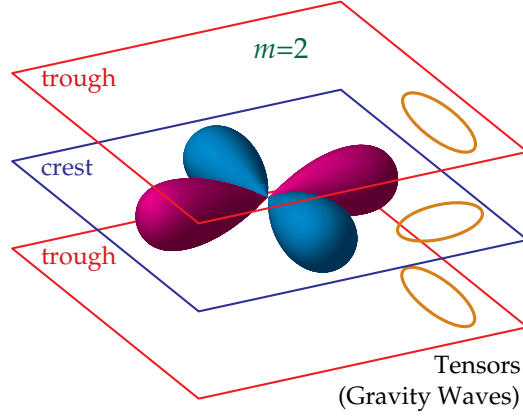


Figure 2.6: Tensor quadrupole moment ($m = 2$). A circle in the plane of perturbation of a gravitational wave is distorted in an ellipse with the semi-major and semi-minor axes that alternate each other. The photons wavelength distortion produces quadrupolar temperature variation $m = 2$. [8]

At $\theta = \pi/2$ then the polarization pattern is a pure Q field. At $\theta = 0, \pi$, the quadrupole lies in the tangential plane giving the maximum polarization. The whole pattern is [8]:

$$Q = (1 + \cos^2\theta)e^{2i\phi}, \quad U = -2i \cos\theta e^{2i\phi} \quad (2.5)$$

as showed, for the real part, in Figure 2.7, where can be noted that both the Q and U component are present. From these considerations the V parameter is expected to be null for the CMB polarization.

2.3 Electric and Magnetic Modes

As described above, for a single plane wave \hat{k} , the different perturbations types $m = 0, \pm 1, \pm 2$ generate different polarization pattern. But on the sky the polarization pattern does not results separated in the described components. In fact there exist an entire spectrum of perturbation with different \hat{k} , with an assumed isotropic distribution of direction, then the averaged power for each l is independent from m . Nevertheless two characteristics of the polarization pattern survive the superposition of a spectrum of different \hat{k} modes: the parity and the correlation with the temperature fluctuations.

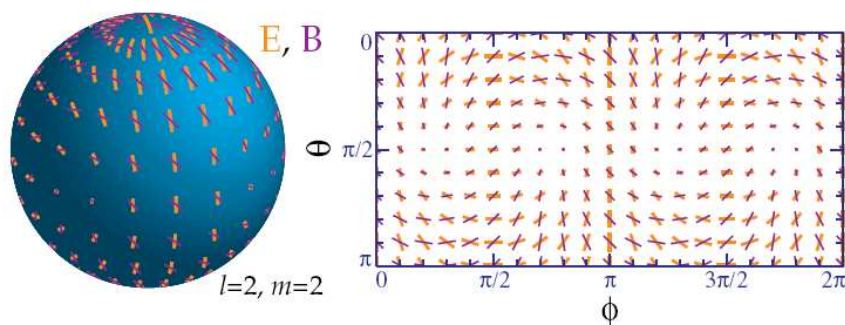


Figure 2.7: Polarization pattern for the tensor perturbations with $l = 2, m = 2$ (yellow). Both Q and U fields are present, in similar quantity. At $\theta = \pi/2$ the field is purely Q with a $\cos(2\phi)$ dependence. The purple pattern is obtained with a 45° rotation. The polarization is maximum at $\theta = 0$ and $\theta = \pi$, contrary to scalar modes. [8]

2.3.1 Parity

The polarization pattern on the sky can be decomposed in two so-called modes: “electric” (E) modes and “magnetic” (B) modes. This distinction reflects local and global properties of the polarization pattern.

The global property is described by the parity of the modes: $(-1)^l$ for the E modes and $(-1)^{l+1}$ for the B modes. This means that for even l , an inversion of $\hat{n} \rightarrow -\hat{n}$ leave the E mode unchanged but the B mode results changed in sign, as shown in Figure 2.8. As can be seen in Figures 2.5 and 2.7, E and B modes are rotated by 45° each other, because for a 45° rotation $Q \rightarrow U, U \rightarrow -Q$. As for the multipole radiation the parity is rotationally invariant and then survive to the superposition over \hat{k} .

Locally the two modes are distinguished by the second derivative of the polarization amplitude, in analogy with the electric and magnetic fields first derivatives (gradient and curl respectively) that are null. For CMB polarization the second derivative condition are applied to the Q and U fields. In particular, for the E modes the difference between the second derivatives of Q in the directions $\hat{e}_\theta + \hat{e}_\phi$ and $\hat{e}_\theta - \hat{e}_\phi$ vanish as for U in the directions \hat{e}_θ and \hat{e}_ϕ . For the B modes the Q and U fields are reversed. Since the Q field is parallel to \hat{e}_θ or \hat{e}_ϕ and the U field is 45° rotated, the direction of maximum variation of polarization is parallel/orthogonal to the polarization itself for the E modes and $\pm 45^\circ$ rotated for the B modes. The E and B modes are shown in Figure 2.8 for the scalar modes, $l = 2, m = 0$.

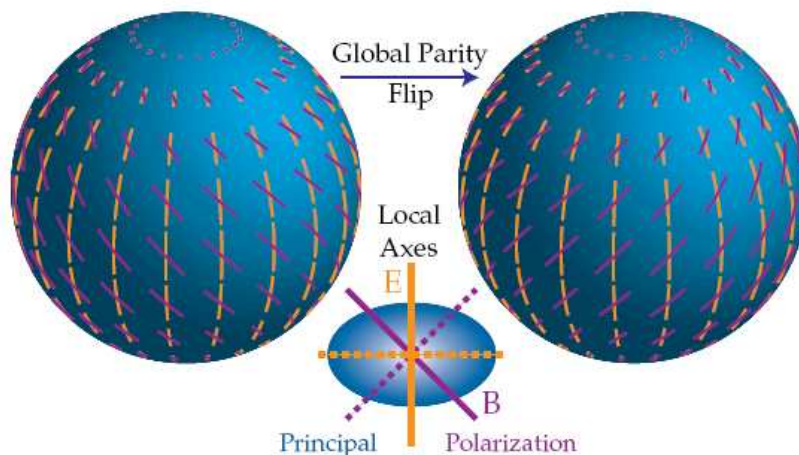


Figure 2.8: E and B modes are globally distinguished by the effect of a transformation of $\hat{n} \rightarrow -\hat{n}$. The parity $(-1)^l$ of the E mode leaves it unchanged, but the parity $(-1)^{l+1}$ of the B mode change its sign. In this case $l = 2, m = 0$. Locally the E and B modes are distinguished by the orientation between the polarization and its gradient: parallel for the E mode and 45° rotated for the B modes. A rotation of 90° (dashed lines) changes the sign of polarization. [8]

2.3.2 Modulation

Because of the parity -1^l of the quadrupolar spherical harmonics, the Thomson scattering can generate only E modes, as represented in yellow in Figures 2.5 and 2.7 respectively for $l = 2, m = 0$, and $l = 2, m = \pm 2$. The same patterns rotated by 45° would represent the B modes (in purple in the same figures) that can't be generated by the Thomson scattering.

As mentioned before, the whole pattern of polarization in the sky results from the modulation of the quadrupoles by the plane waves of the perturbations, as in Figure 2.9.

The plane wave modulation changes the amplitude and the sign (eg $Q \rightarrow -Q$) of the polarization but not the "type", ie a Q field remains Q. However the modulation can generate B modes from E modes, because of the local properties of the modes seen above. The plane wave modulation changes the polarization amplitude always in the \hat{k} direction. For an E mode the maximum variation of the polarization amplitude is in direction parallel or orthogonal to the polarization itself. For a B mode the variation direction is ± 45 degrees rotated with respect to the polarization direction. Then the modulated resulting pattern will depend on the presence of the Q and U

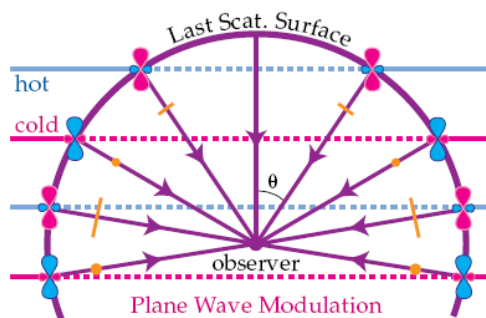


Figure 2.9: Modulation of the scalar quadrupole anisotropy ($l = 2, m = 0$) by the plane wave at the last scattering surface. The modulation changes the sign and the amplitude of the polarization, without mixing Q and U. Conversely the plane wave modulation can generate B modes if U field is present. [8].

fields.

A scalar $m = 0$ perturbation produces a pure $\pm Q$ field that is oriented in direction parallel or orthogonal to \hat{k} , so the modulation in the \hat{k} direction produces E modes. The tensor $m = \pm 2$ perturbations produce comparable amount of Q and U fields. The U field is 45 degrees rotated with respect \hat{k} , so the plane wave modulation produces comparable amount of E and B modes. Then scalar perturbations produce only E modes and tensor perturbations produce both E and B modes.

2.3.3 Correlation with temperature fluctuation

Being the CMB polarization originated by quadrupole temperature anisotropies, there is a correlation between the polarization and temperature anisotropies patterns. The correlation is only partial because the quadrupole temperature anisotropies are not the dominant temperature anisotropies at the last scattering surface. Nevertheless this correlation allows to distinguish between the different source of quadrupolar anisotropies: scalar, tensor, vector, and then between E and B modes.

The E modes correlate with the temperature anisotropies. As seen before the E modes originate from Q fields that are parallel or orthogonal to the plane wave modulation (\hat{k}). E modes are then always parallel or orthogonal to fluctuation gradients.

In particular for the E modes originated by scalar perturbations, the polarization is parallel to the crests of the plane wave and orthogonal to the troughs (Figure 2.3). The superimposition of \hat{k} from all directions leads to

tangential polarization pattern around hot (crests) spots in the sky. Conversely around cold (trough) spots the polarization pattern is radial as shown in Figure 2.10. The polarization-temperature correlation increases at angular scales corresponding to the sound horizon at the last scattering surface. In fact the quadrupole anisotropy that generates the polarization is only the quadrupole generated by the photon flux.

For E modes originated by tensor perturbation the correlation is reversed, because the quadrupole lies in the plane of perturbation. Then the pattern is mainly radial around hot spots and tangential around cold spots. Also in this case the correlation increases towards the scale of the sound horizon, because the gravitational waves signature is frozen at the last scattering surface.

The hot and cold spots refer only to the temperature anisotropies that correlates with the polarization, then the hot and cold spot correlation is not necessary recognizable on the sky.

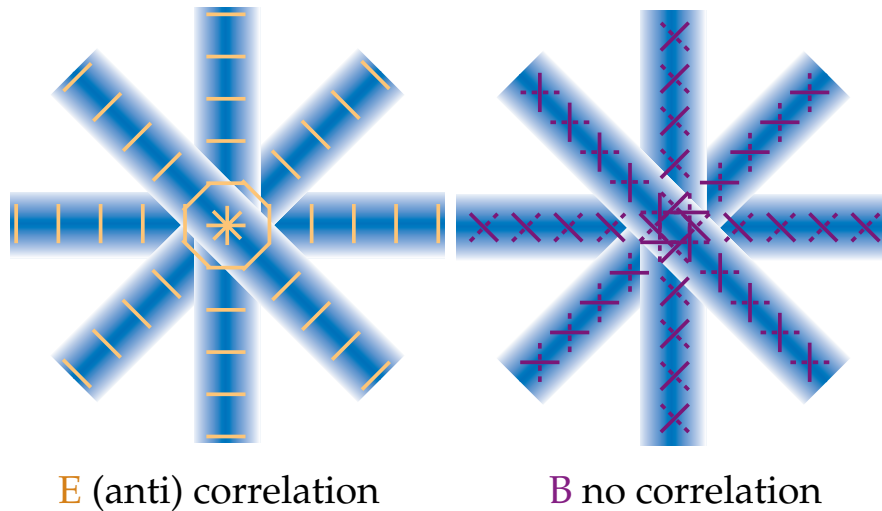


Figure 2.10: Temperature-polarization pattern correlation. The E-mode polarization, being orthogonal or parallel to plane wave crests, generates respectively tangential or radial pattern around hot spots. B-modes do not correlate with temperature, as being ± 45 degrees rotated, contributions from opposite direction are canceled [8]

The B modes arise from plane wave modulation of U fields that are $\pm 45^\circ$ rotated with respect to \hat{k} . The polarization in the B modes is then rotated $\pm 45^\circ$ with respect to the crest and trough of the plane wave. The B modes do not correlate with temperature, because the superimposition of plane waves from opposite directions cancel each other, as in Figure 2.10.

2.4 Polarization Power spectra

As seen the CMB polarization originates from quadrupolar anisotropies of the photon flux at the last scattering surface. The quadrupolar anisotropies are generated by the acoustic oscillations of the photo-baryon fluid that originate the temperature anisotropies, then also the polarization shows angular anisotropies.

As for the temperature anisotropies, also for the polarization anisotropies can be defined angular power spectra. In the polarization case there are different power spectra for E modes (EE), B modes (BB) and for the temperature-polarization correlation (TE).

The polarization power spectra are defined as below:

$$C_\ell^{TT} = \langle \Theta_{\ell,m}^* \Theta_{\ell,m} \rangle, \quad (2.6)$$

$$C_\ell^{TE} = \langle \Theta_{\ell,m}^* E_{\ell,m} \rangle, \quad (2.7)$$

$$C_\ell^{EE} = \langle E_{\ell,m}^* E_{\ell,m} \rangle, \quad (2.8)$$

$$C_\ell^{BB} = \langle B_{\ell,m}^* B_{\ell,m} \rangle \quad (2.9)$$

$$(2.10)$$

where Θ, E, B indicate respectively: temperature, E-modes and B-modes fluctuations. The power spectra of C_ℓ^{TE} describes the temperature-polarization (E modes) correlations. The theoretical spectra are shown in Figure 2.11.

The distribution of multipoles of the polarization anisotropies is defined by the projection on the sky (Figure 2.4). A single plane wave contribute to multipoles till $\ell \leq kr$, where r is the comoving distance to the last scattering surface. The entire power spectra results from the contributions from all the plane waves \hat{k} , with weights dependent on the source of the perturbations (scalar, vector, tensor).

The polarization anisotropies peaks at small angular scales corresponding to the distance the photons can travel before recombination. At angular scales corresponding to distance greater than the photons diffusion distance, the cold and hot photons can not meet and scatter to produce polarization. At large angular scales (small ℓ) the polarization anisotropies are expected to be at minimum.

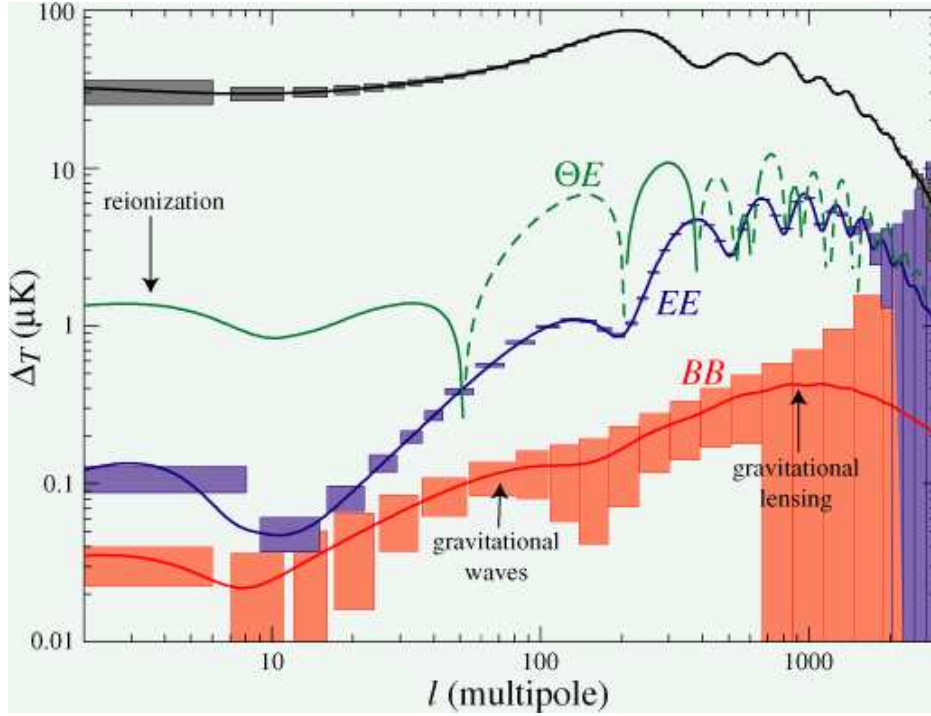


Figure 2.11: Power spectra of temperature, polarization, and TE correlation, calculated for a cosmological model with $\Omega_{tot} = 1, \Omega_{\Lambda} = 2/3, \Omega_b h^2 = 0.02, \Omega_m h^2 = 0.16, n = 1, z_{ri} = 7$. The dashed lines in the TE spectrum represent the anti-correlations. The colored error bars represent the expected statistical errors for the Planck satellite. (Source: <http://background.uchicago.edu/~whu/araa/node4.html>)

2.5 What the CMB polarization tell us

The CMB polarization gives direct information on the last scattering surface, where it is generated. In particular the polarization allows to know when the last scattering occurred, in terms of the fraction of last scattered photons. In the same way can be know the epoch of reionization, caused by the ignition of the first stars, when the photons were re-scattered. The reionization, occurred later, imprints its polarization signature on large angular scales (low ℓ) where the intrinsic fluctuations are smaller.

That the CMB is polarized can be predicted by the acoustic oscillation scenario of the Hot Big Bang model, where the large scale structures are originated from primordial fluctuations by gravitational instability. The verification of the partial CMB polarization on small scales then allows an impor-

tant check on the acoustic oscillations of the Hot Big Bang model. Moreover knowing the temperature power spectrum and the temperature-polarization correlation, it is possible to precisely predict the E-mode power spectrum and verify the cosmological model.

The polarization brings information on the different source of quadrupolar anisotropies that generate it. In particular can be derived the relative content of tensor and scalar perturbation T/S , that is related to the energy scale of the inflation epoch occurred $\sim 10^{-34}$ seconds after the Big Bang [14]. The energy scale of the inflation is at a level of 10^{16} GeV, beyond any particle accelerator that will ever be built on Earth.

From polarization anisotropies can be obtained complementary informations with respect to the temperature anisotropies, breaking the cosmological parameters degeneracies and improving their estimation. Not least, the detection of B modes would be a “smoking gun” for the cosmological background of gravitational waves.

An important issue for the CMB polarization is its faint signal. Only the photons that scatter in an optical thin region, ie at the end of decoupling, can be polarized, because a rapid random Thomson scattering eliminates the polarization. Nevertheless the Thomson scattering can occur when the electrons are still free. At the same time the coupling between photon and electrons reduces the temperature anisotropies. Then the fraction of polarized photons depends from the duration of the decoupling, that determines the number of scattering undergone by the photons. For the Hot Big Bang model the period of decoupling implies a level of CMB polarization anisotropies of about $\leq 10\%$ [8] with respect to the temperature anisotropies.

Being the temperature anisotropies at the level of 10^{-5} , the polarization anisotropies have a level of about $\leq 10^{-6}$, corresponding to a signal of few μK . A so faint signal represents an important issue for the detection and measurement of CMB polarization, that requires high instrumental sensitivities of the order of fraction of μK .

Many experiments are currently planned to accurately measure the CMB polarization. First detection of E-modes and its correlation with the temperature anisotropy was published in 2003 by the DASI collaboration [13], while the most up-to-date measurements come from WMAP [10, 24].

Chapter 3

Polarization Experiments

Measuring the CMB polarization means to map the Stokes parameters on the sky:

$$I = \langle E_{x0}^2 + E_{y0}^2 \rangle \quad (3.1)$$

$$Q = \langle E_{x0}^2 - E_{y0}^2 \rangle \quad (3.2)$$

$$U = 2\langle E_{x0}^2 E_{y0}^2 \cos(\phi_x - \phi_y) \rangle \quad (3.3)$$

$$V = 2\langle E_{x0}^2 E_{y0}^2 \sin(\phi_x - \phi_y) \rangle \quad (3.4)$$

Several types of polarimeters can be designed, with different technologies and that can measure different combination of the Stokes parameters. For the CMB the V parameter, as seen before, is expected to be null, so in principle can be not measured, though can be used as a check.

Moreover different options are available for CMB polarization measurements: imaging or interferometric observation, ground based, balloon-borne, or space-borne experiment, which and how many frequency channels, what type of detector technology. Every option gives constraints on the combination with each other and on other experimental requirements: fraction of sky observed, angular resolution, sensitivity.

3.1 Requirements

Experimental requirements come from the specific scientific goals, and realistically from the time and costs budgets. Nevertheless some considerations can be done on the basis of the CMB polarization features seen before.

3.1.1 Environment

For ground experiments the atmosphere allows observation in just a few atmospheric windows and it is also a source of microwave emission, then it imposes limits on the frequency channels. From ground the sky coverage is never complete, but can be used large telescope or interferometers to reach small angular resolutions.

Balloon-borne experiment avoid the issue of the atmosphere, but they have more constraints on the integration time (ie the time of flight). Moreover, suborbital experiments need to reject the $250^\circ \text{ K} \times 2\pi \text{ sr}$ signal from the ground to remain below the desired noise on large angular scales.

From a distant point in space such as L2, the Earth subtend an angle of about 0.5° , reducing its emission by a factor 10^5 . Moreover, at L2 the Earth and the Sun, can be more easily shielded, and a full-sky coverage is possible. Full-sky coverage is necessary to measure the reionization signal in polarization at large angular scales.

3.1.2 Angular resolution

The angular resolution θ , limits the higher multipole order $\ell = 180/\theta$ one can achieve in the power spectra reconstruction.

The reionization signature peaks at low ℓ (~ 10), so no high angular resolution is required, but an high sky coverage. The B-mode spectrum nominally peaks at $\ell \sim 100$, corresponding to an angular resolution of $\theta \sim 2$ degrees. E-modes peaks at smaller angular scales $100 < \ell < 1000$, ie fraction of degree. At even smaller angular scales is concentrated the signal of the CMB lensing.

An high (the best possible) angular resolution is however necessary for the removal of contamination by the point sources. Each point source has its own emission spectrum, and its contamination cannot be efficiently removed using multi-frequency observations unless the sources can be isolated in the maps.

3.1.3 Foregrounds

In terms of temperature anisotropies, the main foreground contributions in the CMB frequency window come from the synchrotron and free-free emissions below ~ 100 GHz and from the dust at higher frequencies. For the temperature anisotropies mapping, the near-independence of most emission laws on sky coordinates allows for subtraction of foreground contaminants

using a proper linear combination of measurements at a few nearby wavelengths [15].

The sources of polarized foreground is actually not well know. But for polarization measurements the situation could be worse than for temperature, because the CMB is only a few per cent polarized. The main polarized contaminants are the synchrotron and dust emission, that can reach about the 97% of the polarized emission. Synchrotron emission can be up to 70% polarized and dominates at frequencies below 50 GHz, reaching the dust contribution at 65 GHz. The dust emission can be up to 10-15 % polarized in some regions [16]. Then also for polarization, multi frequency observations are required to subtract the polarized foregrounds.

Nowadays the information needed to decide the best observational strategy to optimally subtract polarized foreground contamination are not available. In the next future, the precise measurements of foreground polarization properties will be necessary for the CMB polarization foregrounds removal.

3.1.4 Systematic effects

Systematic effects can be essentially divided in two typologies: multiplicative effects and additive effects. To the first type belong errors involving the instrument, as inaccurate beam shapes, unknown spurious-polarization, sidelobes in the optical response and gain drifts. To the second type belong errors such as glitches due to cosmic ray impacts with the instrument, temperature drifts of the payload, and low frequency noise.

Then to minimize the systematic errors is essential to carefully design the instrument and to measure with precision its operational performance and imperfections.

3.1.5 Sensitivity

Sensitivity is one of the main issues in CMB polarization mapping. As seen, the level of the polarization anisotropies is very small $\sim 10^{-6}$ for the E-modes, and even smaller but not well constrained for the B modes.

The B modes, that are generated by the primordial gravitational waves, represent the final goal of polarization measurements. The main driver for the sensitivity of an experiments can be the level of the B modes from gravitational lensing that is less critical. It set a sensitivity better than few $\mu\text{K}/\text{arcmin}$. In any case until the B mode are measured, the upper limits fixed by previous experiments fix the sensitivity to overcome. Moreover, the sensitivity should be maximum in the frequency channels where the level of CMB emission is maximum, relative to foregrounds.

Polarization experiment then require very high sensitivities that today are limited by the current detector technologies. To increase the instrumental sensitivity two complementary strategies can be done: to substantially increment the integration time and the detectors number. Both strategies are obviously limited: the integration time must be compatible with the time-lives of the instrument and the environmental conditions; the number of detector must be compatible with the dimensions, weight, and power supply of the instrument, especially for flying experiments.

If not all the power spectrum can or want to be reconstructed, the sensitivity requirement is to be evaluated according to the feature one can or want to measure.

3.2 Experimental setup and technologies

As mentioned the scientific requirements define the experimental requirements that are the driver for the experimental setup, the required technologies and the location and environments of the experiment.

A receiver for the measurement of the CMB anisotropies is essentially constituted by an optic that “observes” the sky and a detector that measures the received radiation. Various possible optics and detectors are possible to chose, depending on the experimental setup.

3.2.1 Detectors

The measurement of the Stokes parameter implies the measurement of the power of the received radiation. The power can be measured with radiometers or bolometers. Radiometers use a diode to convert the power of the received radiation into a DC tension at its connectors. Bolometers are thermometers that measure the temperature of a target that absorbs the power of the incident radiation. Both radiometers and bolometers need cryogenic conditions to work properly with minimum noise.

Each technology has advantages and drawbacks that prefers the use of radiometers at frequencies below ~ 100 GHz and the bolometers above. Either for radiometer and bolometers, the current technological limits on the minimum detectable signal, impose to realize instruments with many detectors for each frequency, in order to be able to reach the high sensitivity required for the precise measurements of the CMB polarization.

Radiometric receivers

The simplest way to measure Stokes parameters with radiometers (ie to realize a polarimeter) is to correlate directly signals proportional to the electric field. There are many possible polarimetric schemes to measure microwave polarization. In order to achieve the low noise levels necessary to see CMB polarization, however, the system must be extremely sensitive, and at the same time extremely stable. It should have 1/f noise that is as low as possible and be insensitive to gain drifts in the front-end amplifiers, constituted by High Electron Mobility Transistors (HEMT). The noise performance of the HEMTs constitute the main technological limit on the sensitivity of a radiometric receiver.

The power W of the radiation received by a radiometer is given by the product:

$$W = k\Delta\nu T_A \quad (3.5)$$

where k is Boltzmann constant, $\Delta\nu$ is the bandwidth of the radiometer and T_A is the antenna temperature. The antenna temperature is defined as the convolution of the brilliance temperature of the source T_B with the antenna pattern P_n with which the source is observed:

$$T_A = \frac{\iint_{4\pi} T_B(\theta, \phi) P_n(\theta, \phi) d\Omega}{\int_{4\pi} P_n(\theta, \phi) d\Omega}, \quad (3.6)$$

where T_B for a source of surface brilliance B_ν is:

$$T_B = \frac{c^2}{sh\nu^2} B_\nu. \quad (3.7)$$

Under the hypothesis of a white noise, the minimum signal detectable by a radiometer is given by the ‘‘Radiometer Equation’’:

$$\Delta T_{rms} = K \frac{(T_{Noise} + T_{Sky})}{\sqrt{\Delta\nu\tau}} \quad (3.8)$$

where K is a constant ~ 1 which depends on the radiometric scheme, T_{Noise} and T_{Sky} are the noise and sky temperatures, and $\Delta\nu$ and τ are the bandwidth and the integration time per single detector respectively. The increment of

the numbers of detectors has the same effect of increasing the integration time:

$$\Delta T_{rms} = K \frac{(T_{Noise} + T_{Sky})}{\sqrt{\Delta\nu\tau N}}. \quad (3.9)$$

As an example, to reach the sensitivity of $\sim 1\mu\text{K}$, required by the polarization signal, from the equation of the radiometer 3.9 can be calculated that, with $T_{Noise} \sim 10\text{ K}$, $T_{Sky} \sim 2.7\text{ K}$ e $\Delta\nu \sim 10\text{ GHz}$, it is necessary to observe, with 1 radiometer, in the same direction (or the same pixel of sky) for $\tau \sim 1.6 \times 10^4$ seconds. Moreover if one wants to measure the power spectra at all the angular scales ($2 < \ell < 1000$), all the sky must be observed (4π) with an angular resolution of $\sim 10'$. In this case the sky results divided in 1.5×10^6 pixels, requiring an integration time of about 750 years. Using 750 receivers would reduce the integration time to only one year. For future CMB polarization experiments will be necessary instruments with array of hundreds of receivers, concentrated in reduced space, as the focal plane of an optical system.

A polarimeter can in principle be designed to measure all four Stokes parameters. As seen in the previous chapter, the CMB is expected to exhibit only linear polarization, then for CMB polarization measurements it is desirable to be sensitive to both Stokes Q and U simultaneously. This certainly isn't a strong argument against measuring V, that can be a useful check for the instrument performance. Thus, the polarimeter must be designed with the issue in mind of which Stokes parameters are to be measured.

Bolometers

Bolometers are simply total power detectors composed by a sensitive thermometer that measure the temperature of an high cross-section absorber of heat capacity C, Figure 3.1. Incoming energy E is converted to heat in the absorber. The temperature rise is proportional to the incoming energy as:

$$\Delta T = T - T_0 = E/C. \quad (3.10)$$

Thermometer and absorber are connected to an heat sink at temperature T_0 by means of a weak thermal links G to dissipate the heat. Then temperature in absorber decays with an exponential law, flowing out to the heat sink with a time constant:

$$\tau = C/G. \quad (3.11)$$

Thermometers are made of materials, as doped Germanium crystals, which change strongly in resistivity with temperature. Temperature is hence mea-

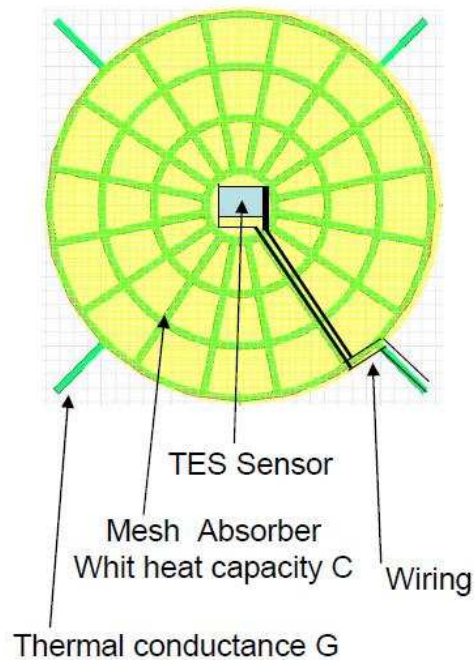


Figure 3.1: Scheme of a “spider web” bolometer. The thermometer is constituted by a TES sensor, placed at the center of the absorber, realized as a spider web to have an high cross-section but “transparent” to the cosmic rays.

sured by mean of resistance. The resistance is measured biasing the thermometer with a constant current or voltage and measuring the voltage or the current respectively.

Bolometers can be made sensitive to polarization by selecting the polarization of the incident radiation. This can be obtained with waveguide component as Orthomode Transducers or other components as Half-wave plates. A special kind of bolometers sensitive to polarization are the Polarization Sensitive Bolometers. They are made sensitive to polarization by realizing the absorber as a kind of wire grid that absorbs only one polarization of the incident radiation. In this case at least two bolometers are necessary to realize polarimeter to measure the Stokes parameters.

3.2.2 Optics

Both coherent radiometers and bolometers have to be coupled with the incident radiation for minimizing the undesired radiation that does not come from the measured source. At the microwave frequencies this coupling is

efficiently obtained by horn antennas, that guide the radio frequency signal to the detector, matching the impedance of the free propagation.

Typical horn antennas are corrugated horns, with pyramidal or conical shape, that can reach high performance in terms of polarization purity, impedance matching and directivity of the field of view, with efficient rejection of unwanted radiation.

Horn antennas are limited in the angular resolution that can achieve. To improve the angular resolution and minimize the spurious radiation, feed-horns are coupled to telescopes. By designing the geometry of the feed-horns in the proper manner, various feeds can be placed on the focal surface of a telescope, increasing the number of detectors and hence the instrumental sensitivity.

The optic of an instrument designed to measure the CMB radiation, constitute the very first interface of the instrument itself with the measured radiation. For these reason particular care must be taken in the design and realization of the optics. Every error or imperfection in design or realization in the optical performance, influences the measurements with systematical errors. Moreover the optical performance must be known at the best to reconstruct as the instrument looks at the sky.

3.3 Were we are

The first complete map of the temperature anisotropies of the CMB were produced by the COBE¹ satellite in the first '90, together with an high precise measurements of the black-body spectrum of the CMB [6]. The COBE results were rewarded with the Physics Nobel Prize in 2006 to George Smoot and John Mather. After the first detection of the CMB anisotropies by COBE [17], many experiments were made for the precise measurements of the CMB temperature anisotropies, from ground as DASI [20], and balloon-borne as BOOMERanG [18], and MAXIMA [19]. These experiments have strongly confirmed the acoustic oscillation scenario foreseen by the Hot Big Bang model. The second generation space mission WMAP², had improved significantly [11] the measurements obtained by COBE, still giving data with improved precision. WMAP, together with other experiments as DASI, CBI, B2K and ACBAR represents the state of art for the temperature anisotropies measurements.

As seen in the previous chapter, the signal of the polarization anisotropies is about one order of magnitude fainter, resulting more difficult to measure

¹<http://aether.lbl.gov/www/projects/cobe/>

²<http://map.gsfc.nasa.gov/>

with precision. Today many experiments as WMAP [21], CBI [22], DASI [4, 5, 13], and BOOMERanG [23] have detected the E-mode polarization and/or its correlation with the temperature anisotropies. The amplitude of the polarization anisotropies is of few μK on angular scales smaller than $\sim 1^\circ$ and of just some tenth of μK on angular scales $> 10^\circ$, as measured from the most recent WMAP 7-years results [24], again confirming the standard cosmological model of the Hot Big Bang.

These low levels represent a great experimental challenge, that requires more technological efforts to open the path to the precision cosmology with the CMB polarization, as already done by Planck for the temperature anisotropies.

Planck

The ESA satellite Planck³ was launched in May 2009 in the Lagrangian L2 point, where it is still measuring the temperature anisotropies with unprecedented angular resolution, frequency coverage (30-857 GHz) and with a foreground-limited sensitivity on the entire sky.

Planck is constituted by two instruments coupled to the same 1.5 dual reflector telescope: the Low Frequency Instrument, with radiometric technology at 30, 44 and 70 GHz, and the High Frequency Instrument, with bolometric technology -with active cooling- at 100, 143, 217, 353, 545 and 857 GHz, with some channels sensitive to polarization.

Planck will be able to measure the TE correlation and to detect the E-mode, but it is not specifically designed to measure the CMB polarization and will be a “reconnaissance” mission, with respect to the high precision measurements of the temperature anisotropies. Planck is opening the path to accurate measurements of CMB polarization anisotropies, the goal of the post-Planck missions, now under feasibility studies.

QUIET

The Q/U Imaging Experiment (QUIET)⁴ employs arrays of correlation polarimeters, cooled to 20 K and coupled to a dual reflector telescope, at 43 GHz and 95 GHz, operating from the Atacama Desert in Chile. QUIET primarily targets the B modes from primordial gravitational waves. Between October 2008 and December 2010, over 10,000 hours of data were collected,

³<http://planck.esa.int>

⁴<http://quiet.uchicago.edu/>

first with the 19-element 43-GHz array and then with the 90-element 95-GHz array.

QUIET detected the polarization in the EE power spectrum at 43 GHz, finding it consistent with the Λ CDM model, confirming the only previous detection of the first acoustic peak [26]. The B-mode spectrum is still consistent with zero, leading to a measurement of the tensor-to-scalar ratio of $r = 0.35_{0.87}^{+1.06}$ [25].

3.4 Future experiments

Future experiments aim to precise measurements of the CMB polarization. To reach this goal are necessary very high sensitivity, with unprecedented control of systematics and wide frequency coverage on the entire sky. These requirements call for the space environment, and in particular for the Lagrangian point L2, as already chosen for WMAP and Planck.

Before going to space an intermediate (necessary) step is the stratosphere. The stratosphere is a near-to-space environment that requires almost the same technological requirements for the components. Moreover the stratosphere permits to reach a good sensitivity, reducing the Earth emission, covering a significant ($\sim 25\%$) sky fraction without the atmosphere frequency limitations. Reaching the stratosphere is relatively simple and cheap (w.r.t. the space) with stratospheric balloons. The stratosphere is then an environment that permits both to test the technologies and obtain relevant scientific results. For these reasons, before the scientific community can head a CMB-polarization dedicated -third-generation- space mission, the intermediate step are the balloon-borne experiments.

Some balloon-borne experiments are already in planning, and/or in the design phase, for the next years, as SPIDER⁵, EBEX⁶, and LSPE, on the wake of BOOMERanG and MAXIMA.

LSPE

The Large Scale Polarization Explorer is an Italian balloon-borne experiments, already funded by the Agenzia Spaziale Italiana (ASI), designed for a precision measurements of the CMB polarization on large ($\sim 1^\circ$) angular scales [27]. LSPE is planned for a long-duration night-flight over the Arctic Polar Circle, that allow a sky coverage of about 25%.

⁵http://www.astro.caltech.edu/~lgg/spider/spider_instr.htm

⁶<http://groups.physics.umn.edu/cosmology/ebex/index.html>

LSPE will be composed by two instruments: a correlation polarimeter, based on the QUIET technology experiment, with a 49-element array at 43 GHz and 7 single elements at 95 GHz; and a bolometric detector, interfaced with a rotating half wave plate, with 40 detectors at 95 GHz, 43 detectors at 145 GHz and 55 detectors at 245 GHz. The sensitivity of LPSE will be better than Planck, for the fraction of sky observed, at the angular resolution of about 1 degree, permitting a better reconstruction of the TE and EE power spectra on a multipole range $10 \leq \ell \leq 200$.

Beyond the aimed scientific results, LSPE will be a great demonstrator of the technology readiness for a third-generation space mission, dedicated to the precise measurements of the CMB polarization. For a third-generation space mission some proposals have already been submitted in response to the European Space Agency Cosmic Vision 2015-2025 call, as the B-Pol⁷ and CoRE⁸ mission.

⁷<http://www.b-pol.org/index.php>

⁸<http://www.core-mission.org/index.php>

Chapter 4

High performance corrugated feed-horn arrays

As mentioned in the previous chapter, in order to be able to reach the high sensitivity (fraction of μK) required for precise measurements of the CMB polarization, future experiment will need hundreds of cryogenic receivers, with high optical performance and control of systematics. This imply to have hundred of detectors, each coupled with an high performance horn antennas. Before to describe the corrugated feed-horns, its useful to recall the general characteristics of an horn antenna.

4.1 Feed-horn characteristic

As each other antenna, feed-horns are mainly characterized by their angular response or “beam pattern”, cross-polarization (ie spurious polarization), impedance-matching and resistive losses (respectively Return Loss and Insertion Loss) and the bandwidth.

4.1.1 Beam pattern

The main characteristic of an antenna and hence of an horn antenna is its beam pattern. The normalized beam pattern is obtained as the ratio between the power received from a direction (θ, ϕ) and the power received from the sight-of-view direction, ie the longitudinal axis of the horn: $\theta = 0, \phi = 0$:

$$P_n(\theta, \phi) = \frac{P(\theta, \phi)}{P(0, 0)}, \quad (4.1)$$

usually expressed in deciBell (dB):

$$P_n(\theta, \phi) = 10 \log_{10} \frac{P(\theta, \phi)}{P(0, 0)}. \quad (4.2)$$

Being the antenna a passive element, it is “reciprocal” with respect to the electromagnetic propagation. This means that the same definition of beam pattern, as each other characteristic definition, applies also in transmission. For feed-horn antennas the beam pattern recalls the ”Airy” pattern from the Fraunhofer diffraction from a circular hole. The pattern has then a main lobe surrounded by side lobes, typically with reduced intensity.

The first characteristic of a beam pattern is the width of the main lobe at half power level with respect to the maximum power level, named **F**ull **W**idth **H**alf **M**aximum. The FWHM corresponds to 2 times the angle θ at which the measured power is one half with respect to the power at $\theta = 0$, that in dB means -3dB. The square of the FWHM represents the solid angle the antenna can see with approximately a flat power response, ie the angular resolution of the antenna. The FWHM of an antenna can be calculated at the first order as the ratio:

$$FWHM \sim \frac{\lambda}{D} \quad (4.3)$$

where λ and D are respectively the wavelength of the observed radiation and the aperture diameter of the antenna. The FWHM then decreases with increasing diameters and decreasing wavelength.

The beam pattern defines the “directivity” D of the antenna as,

$$D = \frac{P(\theta, \phi)_{max}}{\int P(\theta, \phi) d\Omega} = \frac{4\pi}{\int P(\theta, \phi) d\Omega} = \frac{4\pi}{\Omega_A}, \quad (4.4)$$

where Ω_A is the solid angle at which all power would flow through, if the antenna radiation intensity were constant and at the maximum value. The directivity estimates how much of the antenna radiation is concentrated in the main beam and not coming from others directions, the so-called “straylight”. The high sensitivities required by the measurements of CMB polarization ($\sim \mu\text{K}$) imposes a strong suppression of the straylight, then the angular response of an antenna must be very directive.

To improve the angular resolution of an antenna at a given frequency band, the aperture must be increased. To increase the aperture of a conical horn antenna two approaches can be used: to increase the length of the horn or to increase the aperture angle, named flare, keeping the same length. As shown in Figure 4.1, for flare angles > 10 degrees, the FWHM depends from the flare angle with an oscillating response, while increasing the horn length can give rise to dimensional and mechanical issues. In any case, as shown in Figure 4.1, the FWHM is limited in increasing the flare angle or the aperture. To reach better angular resolution, horn antennas need to be coupled to optical systems as dielectric lenses or telescopes.

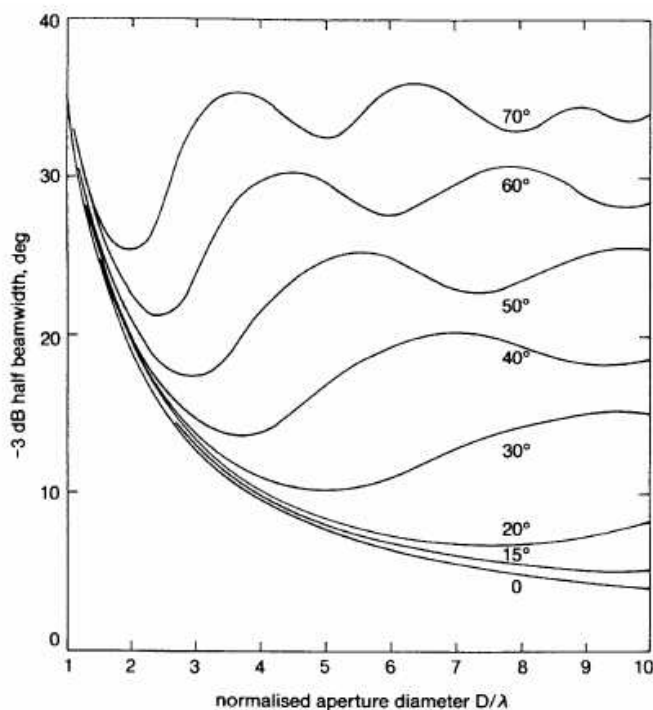


Figure 4.1: Dependence of the FWHM when D/λ varies, for different values of the flare angle. For flare angle > 10 degrees the approximation 4.3 is even less true [29].

The beam pattern being a two dimensional function can be described a surface. Typically not all the surface is reported but just four principal cuts, or planes, at constant ϕ . The fundamental planes are named E, H, $+45$ and -45 , corresponding respectively to cuts at $\phi = 0$, $\phi = 90$, $\phi = +45$ and $\phi = -45$ degrees, with respect to the direction of the E field propagating

inside the horn.

Cross polarization

Eventual asymmetries between the beam pattern planes indicate a non uniform response of the horn to the polarization of the field. This means that if excited with a given polarization, the horn transfers part of the field to the orthogonal polarization. This “leakage” of polarization is called “Cross-Polarization”. The most widespread definition of cross-polarization is the third Ludwig’s definition [28]:

$$\hat{e}_{xp} = \sin(\phi)\hat{e}_\theta + \cos(\phi)\hat{e}_\phi \quad (4.5)$$

$$\hat{e}_{co} = \cos(\phi)\hat{e}_\theta - \sin(\phi)\hat{e}_\phi \quad (4.6)$$

in the coordinate system with the origin on the antenna aperture and with the \hat{z} axis orientated along the axis of the horn, as in Figure 4.2. The maximum cross-polarization is always obtained with respect to the ± 45 degrees planes [29].

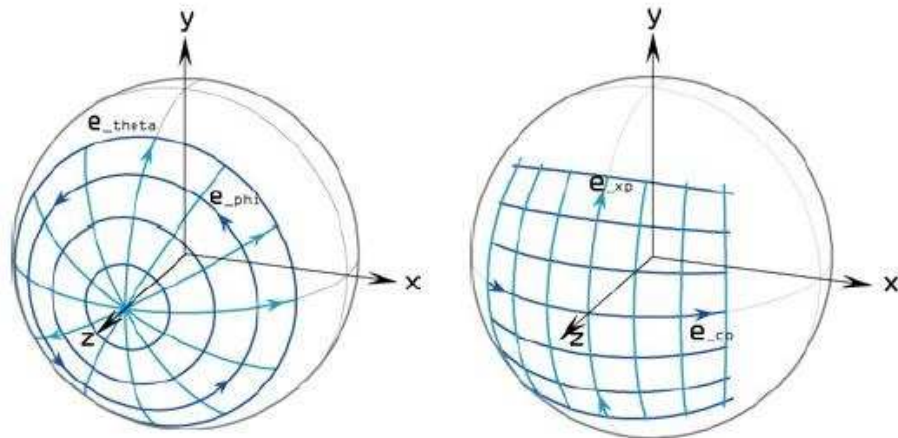


Figure 4.2:

Side Lobes

To reach the required high sensitivity for CMB polarization measurements, a very low level of side-lobes is required in the antenna pattern. For example

taking an experiments from the ground and with a typical angular resolution of $10'$, the ground emission comes from a solid angle of 2π , then the ground antenna temperature is approximated as:

$$T_{A,Ground} \simeq \frac{T_{Ground} \times 2\pi \times P_{Side}}{\int_{4\pi} P_n(\theta, \phi) d\Omega} \quad (4.7)$$

where P_{Side} is the side-lobes level and T_{Ground} is the brilliance temperature of the ground (~ 300 K). Considering that the main lobe of the antenna pattern is typically three order of magnitude higher than the side-lobes, the ground antenna temperature can be rewritten as:

$$T_{A,Ground} \simeq \frac{T_{Ground} \times 2\pi \times P_{Side}}{\Omega_{MainBeam}}, \quad (4.8)$$

and $\Omega_{MainBeam}$ is given by the approximation:

$$\Omega_{MainBeam} \simeq \iint_{\Omega_{MB}} P_n(\theta, \phi) d\Omega \simeq (\theta_{FWHM} \times \theta_{FWHM}). \quad (4.9)$$

To obtain the sensitivity of $\sim \mu\text{K}$, is required that:

$$T_{A,Ground} < 10^{-6},$$

then for an angular resolution of $10'$:

$$T_{A,Ground} \simeq 10^{-6} \simeq \left(\frac{1}{10/60} \frac{180}{\pi} \right)^2 (300K \times 2\pi \times P_{side}). \quad (4.10)$$

The required level of side lobes is $P_{side} \sim 4 \times 10^{-15}$ corresponding to -143 dB, not achievable with the feed horn alone. To observe the CMB polarization from the ground, shields are needed surrounding the experiments to reject the 300 K ground signal.

Reducing the solid angle subtended by the ground the side lobes requirement can be relaxed. Reducing the ground solid angle means to fly the experiments in the stratosphere or in space. For example from the Lagrangian

point L2 (see WMAP and Planck), at a distance of 1.5×10^6 Km, the Earth subtends an angle of about 7.6×10^{-5} sr. The side lobe level in this case is reduced to:

$$P_{side} \simeq 4 \times 10^{-15} \frac{2\pi}{7.6 \times 10^{-5}} \simeq 5 \times 10^{-10} \quad (4.11)$$

ie about -90 dB, hard to obtain but less critical.

4.1.2 Insertion Loss and Return Loss

The signal losses caused by a passive component, as the feed horn, contribute to its noise temperature T_n as the equation below:

$$T_n = [1 - 10^{\frac{RL}{10}}] \cdot [1 - 10^{\frac{IL}{10}}] \cdot T_{phys} \quad (4.12)$$

where T_{phys} is the physical temperature of the component, and RL and IL stands for Return Loss an Insertion Loss respectively, expressed in dB. The return loss describes the losses due to the impedance matching, the insertion losses describes the losses due to non-perfect conductivity of the material constituting the component.

In a system of n components in cascade, each characterized by its noise temperature T_{ni} , and its gain G_i (that in the case of a passive component is < 1 , ie an attenuation), the total noise temperature T_n^{tot} is given by the Friis formula:

$$T_n^{tot} = T_{n1} + \frac{T_{n2}}{G_1} + \frac{T_{n3}}{G_1 G_2} + \frac{T_{n4}}{G_1 G_2 G_3} + \dots \quad (4.13)$$

Then if the system is composed by a passive component as a feed horn, followed by an amplifier, the T_{n1} of the passive component contributes entirely to the total noise temperature of the system T_n^{tot} . Moreover, being the gain of passive component $G_1 < 1$, the contribute T_{n2} of the active component results incremented by a factor $1/G_1$ in the calculus of the total noise temperature T_n^{tot} .

As an example, assuming cryogenic conditions ($T_{phys} = 20K$), with typical IL and RL as for the Planck LFI (IL = -0.15 dB, RL = -30 dB), the horn noise temperature would be $T_n^{horn} = 0.68$ K, while the noise temperature of the subsequent components would be incremented by a factor $1/G_{horn} \cong 1/0.965 = 1.036$. To minimize the noise temperature is then necessary to limit as much as possible the losses of the feed horn, before they would amplified by the subsequent amplifiers.

The figures below show the trend of the noise temperature T_n as a function of the insertion loss for fixed values of return loss (Figure 4.3), and as a

function of the return loss with fixed values of insertion loss (Figure 4.4). As seen in the graphs, the insertion loss effect on the noise temperature is more critical with respect to the return loss.

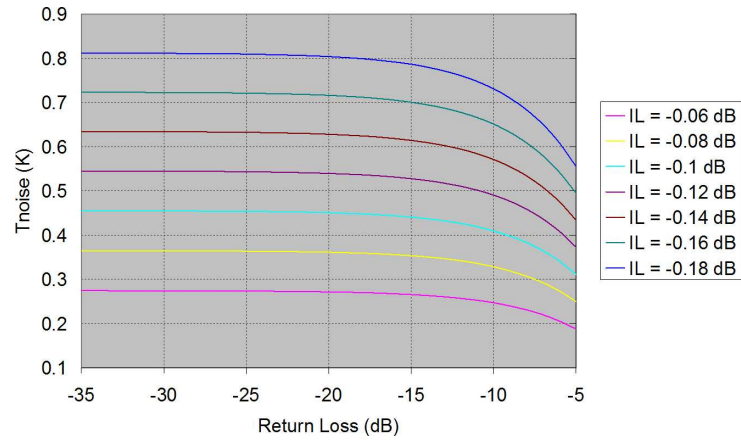


Figure 4.3: Noise temperature against Return Loss for various values of Insertion Loss.

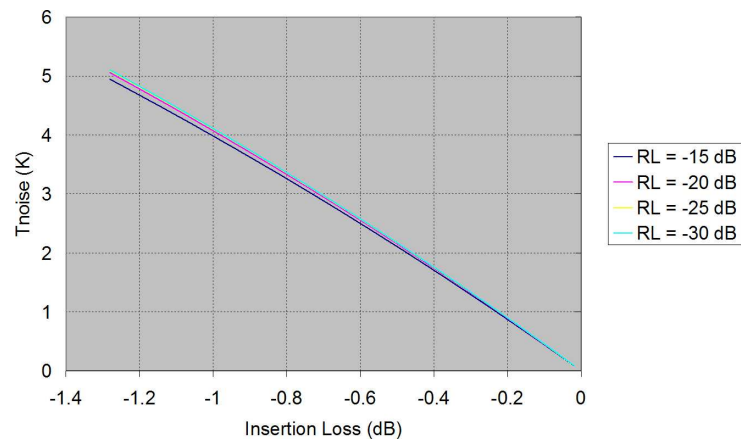


Figure 4.4: Noise temperature against Insertion Loss for various values of Return Loss.

4.1.3 Bandwidth

The equation of the sensitivity of a radiometer,

$$\Delta T = K \frac{T_{sys}}{\sqrt{\beta\tau}} \quad (4.14)$$

shows that the minimum detectable signal for the instrument is proportional to its system temperature: $T_{sys} = T_{sky} + T_{noise}$, and inversely proportional to the square root of the product between the bandwidth β and the integration time τ . The K factor depends from the particular radiometric scheme and is of the order of 1, for example for the Planck-LFI radiometer its value is $\sqrt{2}$. Similarly for a correlation polarimeter, as that of the QUIET experiment, the sensitivity for the Stokes parameters Q and U is given by:

$$\Delta T_{Q/2} = \sqrt{\frac{2}{\beta\tau}} \cdot \frac{Q}{2} = \frac{Q}{\sqrt{2\beta\tau}} \quad (4.15)$$

$$\Delta T_{U/2} = \sqrt{\frac{2}{\beta\tau}} \cdot \frac{U}{2} = \frac{U}{\sqrt{2\beta\tau}} \quad (4.16)$$

where Q and U are defined in terms of Q/2 and U/2, and include the polarization signal T_Q and T_U and the instrumental noise T_{noise} :

$$Q = T_Q + T_{noise} \quad (4.17)$$

$$U = T_U + T_{noise}. \quad (4.18)$$

It is evident as the instrumental sensitivity depends from the bandwidth of the receiver and firstly from the antenna bandwidth that is the first element. The antenna bandwidth is then a fundamental requirements for CMB experiments with a typical value of 20% w.r.t. the central frequency $f_{central}$. This means that the requirements on the antenna beam pattern, RL and IL are metted in the frequency band $0.9 \times f_{central} - 1.1 \times f_{central}$.

4.2 Corrugated feed-horn

The desired performance of a feed-horn designed to measure the CMB polarization call for an highly symmetrical beam pattern, with as low as possible side lobes and cross-polarization (spurious polarization generated by the horn). Moreover also the losses (IL and RL) are required as low as possible. These performance must be satisfied over the largest possible bandwidth. Corrugated horn antennas can reach these high performance in terms of polarization purity, impedance matching and directivity of the field of view, with efficient rejection of unwanted radiation over a wide bandwidth.

The horn beam pattern, as mentioned before, recalls the ‘‘Airy’’ pattern of the Fraunhofer diffraction from a circular hole. More precisely the beam

pattern is given by the Fourier Transform of the electromagnetic field at the aperture of the feed-horn. Then shaping the beam pattern means to shape the field at the horn aperture.

To obtain symmetrical beam pattern with low side-lobes it is necessary to have an electric (and hence magnetic) field uniformly distributed over the aperture of the feed. In that way for every ϕ cut over the aperture of the horn the electric field intensity has the same trend, and the same is true for the Fourier-transformed far-field, ie the beam pattern.

Nevertheless, inside a circular waveguides of radius r the fields can distribute only in certain “modes”, given by the solution of the Maxwell equations with the circular boundary condition. The solutions that describe the modes are the Bessel functions of the first kind $J_n(Kr)$, where K is the transverse wavenumber [29].

The *single* mode that give the most symmetric field distribution, and hence far-field beam pattern, is the TE₁₁ mode, that is the fundamental mode for circular waveguides.

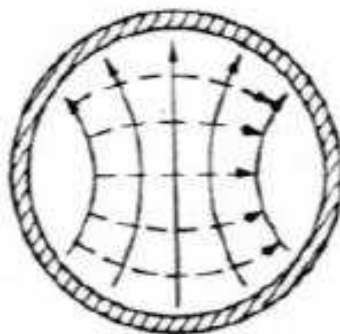


Figure 4.5: Field distribution of the TE₁₁ mode inside a circular waveguide

The highly symmetrical patterns desired for the CMB polarization experiments require a more uniform field distribution that the only TE₁₁ mode can't give. The desired field distribution can be achieved with the sum of the two modes TE₁₁ and TM₁₁ giving the *hybrid* mode HE₁₁, as shown in Figure 4.6. The hybrid EH₁₁ mode is then obtained propagating simultaneously, ie in phase, the TE₁₁ and the TM₁₁ modes. To do this an hybrid boundary condition is needed, that satisfies both the modes.

The hybrid boundary condition is achieved *corrugating* the horn internal surface, ie realizing transverse circular hollows on its internal surface, as in Figure 4.7.

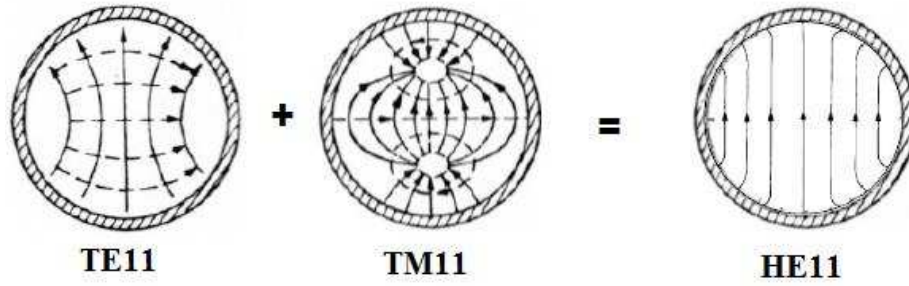


Figure 4.6: The hybrid mode HE11 is obtained summing the TE11 and TM11 modes.

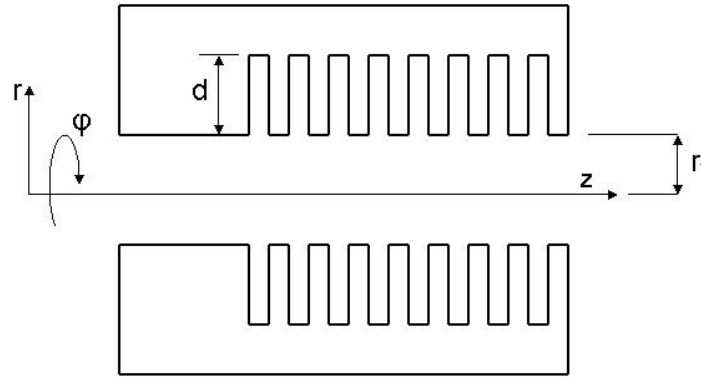


Figure 4.7: Corrugated waveguide.

The \mathbf{E} field for the hybrid mode HE11 is given by [29]:

$$\mathbf{E} = A J_0(Kr) \hat{i}_x - \left(\frac{(X - Y)}{4} \right) \frac{U_0}{kr_1} J_2(Kr) \left[\cos(2\phi) \hat{i}_x + \sin(2\phi) \hat{i}_y \right] \quad (4.19)$$

where $J_n(Kr)$ is a Bessel function of the first kind, $\hat{i}_{x,y}$ are the unit vectors in the x and y directions, K and k are respectively the transverse and the free space wave numbers, X and Y are the reactance and admittance of the

boundary at $r = r_1$. Being the boundary a circular waveguide:

$$X = -j \frac{Z_\phi}{Z_0} = -j \frac{E_\phi}{H_z} \left[\frac{\epsilon_0}{\mu_0} \right]^{1/2} \quad (4.20)$$

$$Y = -j \frac{Z_0}{Z_z} = -j \frac{H_\phi}{E_z} \left[\frac{\epsilon_0}{\mu_0} \right]^{1/2} \quad (4.21)$$

with the fields in eqns. 4.20 and 4.21 evaluated at the boundary $r = r_1$ [29].

If the $(X - Y)$ term vanish then the \mathbf{E} field is independent form ϕ and free of cross polarization. For a corrugated waveguide (or horn) $E_\phi = 0$, because the corrugation are seen as waveguides in a cut-off condition, then $X = 0$. Y is the admittance at the boundary $r = r_1$, the corrugations at the boundary are terminated transmission lines with admittance:

$$Z \approx \frac{1}{j \cdot \tan(kl)}$$

where l is the depth of the corrugation. If the corrugation depth is equal to $\lambda/4$, corresponding to an open line, then also $Y = 0$ ie $H_\phi = 0$ and the *balanced hybrid condition* is achieved. The corrugation depth is varied from $\lambda/4$ to $\lambda/2$ going from the horn aperture toward the throat, to match the short circuit condition of the waveguide at the end of the horn. Noting that at the frequency of 100 GHz, the hybrid condition gives a corrugation depth of 0.75 mm, it is clear as the fabrication of horn at high frequencies is a technological challenge.

4.3 Specifications for high performance feed-horns arrays

As said the goal of this work is to develop an efficient and reliable design to realize big array (hundreds of elements) of high-performance corrugated feed-horns, suitable for the next generation of CMB polarization experiments. This goal implies the joint analysis of: i) the electromagnetic performance required (and then the e.m. design), ii) the mechanical requirements and iii) the fabrication techniques, from which one can not ignore.

4.3.1 Electromagnetic requirements of high performance feed-horns

The electromagnetic performance and mechanical requirements are defined from time to time from the scientific goals of the single experiment, nevertheless some guidelines can be established for any high-precision CMB polarization experiment.

Scientific requirements of an experiment dedicated to the precise measurements of the CMB polarization anisotropies, impose strong electromagnetic requirements for the feed-horns. To minimize the spurious polarization signal generated by the feed-horn, its beam pattern must have a high level of symmetry. As shown in the previous chapter, the rejection of the stray-light radiation must be very efficient to reach the required sensitivity, then a high directivity with a low level of near and far side-lobes is required for the beam pattern. Moreover, because the feed-horn precedes the first stage of amplification, it is very important that the feed-horn losses, either resistive and of impedance matching, are as low as possible, in order to keep a low system noise temperature.

A good feed-horn beam pattern, as for example those of the Planck-LFI experiment, has near and far side lobes under the level of -30 dB and -50 dB respectively, and a low level of ellipticity of the beam, of the order of 0.95, as measured on a plane orthogonal to the boresight and at the -3 dB level. The beam pattern requirements can not be given without knowing the performance of the entire instrument of which it is part, and in particular of the eventual telescope/optic coupled. In fact the symmetry requirements of the beam pattern and its Full Width Half Maximum is related to the feed-horns position in the focal plane of the optic.

Regarding the FWHM of the beam pattern, it depends on the smallest angular scale aimed to measure. As seen a feed-horn "alone" can achieve a minimal FWHM of about 6 degrees, corresponding to an angular scale of $l \sim 25-30$. In order to be able to obtain a smaller FWHM an optical system is required to be coupled to the feed-horn. To properly couple the feed-horn with an optic, as a lens or a telescope, the feed-horn FWHM must be chosen in order to illuminate in the proper manner the right surface of the coupled optic and obtain the wanted final FWHM.

The cross-polarization indicates the spurious polarization generated by the feed-horn. Its level must be as low as possible, especially in a polarization experiment. Keeping the cross-polarization level very low is not simple, as typically improving strongly a characteristic can worsen the others, as for example the bandwidth. In any case a high performance feed-horn should have a polarization contamination less than -30 dB.

The return loss is typically linked to beam pattern characteristics, then a point of equilibrium must be found. The return loss, as shown above, determines the noise temperature of the system, that limits the sensitivity of the instrument. The insertion loss has a weight even greater on the system noise temperature, then the requirements of an high performance feed-horn in terms of losses would be a return loss < 30 dB and an insertion loss < 0.1 dB.

The bandwidth defines in a directly manner the instrumental sensitivity (Eq. 3.9), requiring to be as large as possible. Typical bandwidth, achievable for all the previous characteristics, are of 20-25 % of the central frequency.

The level of electromagnetic performance of an high performance feed-horn, suitable for precise measurements of the CMB polarization anisotropies, can be then summarized as follow:

- Side lobes < -30 dB
- Far side lobes < -50 dB
- Cross-polarization < -30 dB
- Bandwidth $\sim 20\%$
- Insertion loss > -0.1 dB
- Return loss < -30 dB.

Keep in mind that, if the feed-horn is coupled to an optic, the final beam pattern is given by the coupling of the entire optical system. Then the feed-horn performance have to be chosen in relation to the final beam pattern of the entire optical system.

4.3.2 Mechanical requirements for high-performance feed-horn arrays

The fabrication of hundreds of such high-performance corrugated feed-horns is a great experimental issue for CMB polarization experiments. In particular, without change the performance, and hence the electromagnetic design, the dimensions of the feed-horn scale with the frequency: more higher the frequency, smaller the dimensions. Moreover mechanical tolerances are more critical increasing the frequency band. Then, as seen for the corrugation depth, at high frequencies (> 100 GHz) the fabrication of such feed-horn represent a true technological challenge.

Realizing feed-horns *arrays* involves other mechanical issues and constraints besides those of the electromagnetic design. First of all the feeds displacement and the composition of the array. The feeds displacement comes from the focal plane of the optical system. Typically the feed-horn would be displaced with no distance between them, keeping the apertures tangential, but clearly some material have to exists between them. The feed-horns also should fit the focal plane surface that is typically curve. Finally the focal plane can be composed of multi frequency channels, involving feed-horns with different dimensions, both in aperture and in length.

Besides the optical instrumental constrains, also fabrication and testing issues have to be taken into account. The realization of a unique single (big) array can be very problematic or impossible to do, depending on the working volume of the machine used for the fabrication. A single array can also be very critical for its electromagnetic tests, either for the mass/volume to be managed and for the beam pattern tests accuracy, that can be affected by the form and dimension of the array. Moreover a single array is very critical regarding possible failure of single elements and for the integration with the whole instrument. For the cited reasons an array composed of modules or sub-arrays permits to overtake most of these issues with the drawback of the integration of the modules in the final array that require other structures to be realized with precision.

Typically array of receivers require an high density of elements, with dimension and weight as small as possible to minimize testing and managing issues. For flying experiments weight and dimension are strictly constrained by the mission requirements, becoming an experimental issue. Moreover the array must survive cryogenic conditions (thermal contractions) and, in case of flight, vibrational stress. Then not only the single elements have to be designed correctly from the mechanical point o view (and obviously from the electromagnetic one) , but also the assembly of the elements and of the eventual holding structure. This means that the electromagnetic design and the mechanical design are then strictly connected and they can not ignore from the fabrication technique and materials choice.

4.3.3 Fabrication techniques for feed-horn arrays

Typical fabrication techniques for feed-horns, and in particular for corrugated feed-horns, as the direct machining and the electroforming, allow to realize single elements with high precision but are time and cost expensive, and then not suitable for many element production. In recent years new fabrication techniques have arisen, as the 3D printing and the platelet technique, giving the opportunity to reduce times and costs, realizing more elements at the

same time and keeping adequate precisions. A brief summary of the principal technique used for the realization of corrugated feed-horns is in Table 4.1

Technique	Pro	Cons
Electroforming	High precision, allow complex geometries (e.g. OMT)	High costs, time consuming, complex process, sacrificial mandrel-tools
Electroerosion	High precision, geometries with sharp edges	High costs, time consuming, complex process, sacrificial mandrel-tools, no undercuts
Direct Machining	High precision, better times and costs w.r.t. electroforming and electroerosion	Expansive machine-tool for complex geometries (no OMTs), no small geometries (high frequencies), time expensive.
Platelet	Time and costs effective (w.r.t. electroerosion and electroforming), modular approach, limited risks	Requires precise alignment system and mass control,

Table 4.1: Comparison of fabrication techniques for corrugated feed-horn.

Electroforming

Electroforming consists in an electrochemical deposition of material on a mandrel. The mandrel is realized by direct machining as a negative of the desired object. In this way the geometry of the mandrel object is copied with high precision. High accuracy is required in controlling currents and pH of the electrochemical bath. Moreover the material chosen for the mandrel and the object have to be adequate to work as anode and cathode. At the end of the process the mandrel and the object are separated. For complex geometries, as corrugated feed-horns, the mechanical separation is not possible and then is necessary to dissolve the mandrel in an acid solution that do not dissolve the desired object. The electroforming allow to realize complex geometries with high accuracy, at the same time it is an expansive, complex and time consuming technique, resulting not suitable for mass-production.

Electroerosion

Electroerosion provides the realization of an object removing the material by erosion. The erosion is obtained with mandrel-tool with the negative shape of the desired object or with a cutting current-carrying wire. The mandrel or wire acts as electrode that erode the material. This technique is very similar to the electroforming in terms of precision, costs and times, and obviously can be applied just on metallic objects.

Direct machining

Direct machining (typically turning) is generally less time consuming w.r.t. the electroforming and electroerosion, but it is limited in the minimum dimension of the objects. In particular for what concern the corrugated feed-horns the minimum size workable corresponds to a maximum frequency of about 100 GHz. Moreover, as the feed-horn are realized one at a time, the direct machining is not suitable for mass-production.

The major limit in realizing corrugated feed-horn are the corrugations, in particular in the throat region, that require custom, small-size and expensive tools. The realization of corrugation for high frequencies feed-horn is also a critical machining that can compromise the realization of entire object.

3D Printing

The 3D printing is a recent technique, based on the idea of the lithography. In this case a polymer or a metallic powder is deposited in layers and fixed with glue.

The technique is very cheap and rapid and is actually used for the prototyping of design objects. Unfortunately the low precision achieved and the few availability of materials make this technique not suitable, until now, for the realization of corrugated feed-horns. In particular the use of glues (dielectric materials) is unsuitable for the electromagnetic and cryogenic requirements of the feed-horns.

Platelet

The technique chosen in this work, which from other works seems to be promising [31, 32], is the “platelet” technique, that provides the realization of the feed-horns by layers or plates. The platelet technique consists in the overlap of properly machined metal sheets so that the feed-horn is then realized in layers. This method is relatively cheap, with a cost saving of about 90% with respect to the electroforming and allows quick manufacturing of

feed-horn arrays by drilling several holes in each plate. A complete corrugation, with a tooth and a groove, can be obtained in each plate. A complex focal surface can be obtained with a series of modules properly tilted to reproduce the required geometry. Particular care is required in the plate assembly alignment system and for mass/volume control in order to minimize the weight.

Bonded and non-bonded platelet

Plates assembling can be obtained substantially in two manners. By bonding the plates, or by fix them with bolted connections.

The bonding can be realized as a soldering (light brazing) or a diffusion bonding. The soldering provides the addition of a filler metal between the plates as bonding alloy. The alloy have to be a melting point lower than that of the plates and the shape and quantity of the bonding alloy have to be chosen precisely in order to avoid leakage inside the feed-horn. The diffusion bonding does not requires a bonding alloy but is based on the diffusion of a material in each other at relatively high temperature (0.5 of fusion temperature) and under pressure. Both these bonding methods requires particular tools (like ovens and presses) and are time consuming, but allow a minimum separation between the horns with an high compactness of the arrays. Obviously are irreversible junction with the related risks.

Non-bonded junctions make use of bolted joints. This method is very simple, rapid, cheap ad reversible, but requires the spaces to accommodate the head and the bolts. Then a reduced compactness can be achieved w.r.t. the bonded junction. A non-bonded platelet, shown in Figure 4.8 was already realized by me with very good results [30].

The advantages of the platelet technique go beyond its application to CMB measurements and can be exploited in a wide range of mm-wave and sub-mm astronomical instruments. In particular, platelet techniques may prove appropriate for the new generation of very large interferometric arrays, such as ALMA¹, which require high performance antennas (including polarization properties) over a large number of channels.

¹<http://www.eso.org/sci/facilities/alma.html>

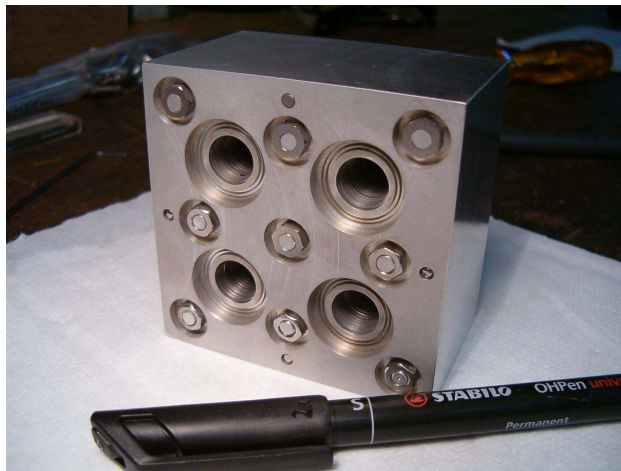


Figure 4.8: The previously realized non-bonded platelet array prototype. The feed-horns have a central frequency of 100 GHz

Chapter 5

A non-bonded platelet feed-horn array

In this work I have developed a prototype of feed-horn array, realized with the non-bonded platelet technique, as an evolution of the previously realized prototype [30], shown in the previous Chapter.

The prototype of this work is an array of seven corrugated-profiled feed-horns in W band (75-110 GHz). The array is designed for compactness, light-weight, reliability in cryogenic conditions and with electromagnetic performance polarization-suitable. Moreover the array can be replicated for the composition of larger arrays composed of many such 7-elements modules.

5.1 Electromagnetic design

The electromagnetic design of the feed-horns was derived on the basis of the guidelines given in the previous chapter and here summarized:

- Side lobes < -30 dB
- Far side lobes < -45 dB
- Cross-polarization < -30 dB
- Bandwidth $\sim 20\%$
- Insertion loss > -0.1 dB
- Return loss < -30 dB.

As shown in Chapter 4, these performance are suitable for an experiment dedicated to the measurements of the CMB polarization.

Being the scope of this work the technological development of the fabrication technique, no particular care and/or optimization was taken for the electromagnetic performance and design. Moreover the feed-horns of the prototype are not part of an experiment with an eventual optic, from which the electromagnetic design can not ignore.

5.1.1 Rules of thumb

To obtain the electromagnetic design the so called “rules of thumbs” have been used. The starting parameters are the following:

- Central frequency: 100 GHz ($\lambda_{central} = 3mm$)
- Bandwidth: 20% ($\pm 10\%$)
- Semi-flare angle: 6 degrees
- Full Width Half Maximum: 22 degrees

The circular waveguide radius r was calculated from the cut-off frequency formula:

$$\lambda_{cut,mn} = \frac{2\pi r}{p_{mn}} \quad (5.1)$$

where p_{mn} is the coefficient that depends from the considered propagation mode. In this case, to obtain the typical hybrid EH11 mode at the aperture, is necessary to excite the fundamental mode TE11 inside the circular waveguide, corresponding to $p_{mn} = 3.832$. The resulting starting waveguide diameter is 2.033 mm at the lower frequency of the band, ie 90 GHz.

The aperture D was initially calculated from the approximated rules as form Eq. 4.3:

$$FWHM = 1.22 \frac{\lambda}{D} \quad (5.2)$$

taking the resolution (FWHM) of 22 degrees and obtaining an aperture diameter of 9.532 mm for the central frequency of 100 GHz.

For what concerning the corrugation design, the starting parameters are the following [29]:

- corrugations per $\lambda_{central}$: 3
- corrugation for the hybridization section at the throat: 4
- width of the throats: 0.6 mm.

A linear transition, from $\lambda/2$ to $\lambda/4$, was applied for the depth of the first 4 corrugation of transition, that change the propagation mode from the fundamental TE11 to the hybrid HE11.

With these initial parameters the length L of the feed-horn would be of 44.05 mm, realized with 44 corrugations of 1 mm thickness each (three for λ). In order to reduce the criticalities concerning the assembling of the plates and to reduce the fabrication time, the number of corrugations (and plates) was reduced by profiling the starting conical shape. As for the Planck LFI feed-horns [33] the shape is dual-profile with a sine-square section plus an exponential one:

$$R(z) = R_i + (R_s - R_i) \left[(1 - A) \frac{z}{L_s} + A \sin^2 \left(\frac{\pi z}{s L_s} \right) \right], 0 \leq z \leq L_s \quad (5.3)$$

$$R(z) = R_s + e^{\alpha(z-L_s)} - 1, \quad L_s \leq z \leq L_e + L_s, \quad (5.4)$$

with

$$\alpha = \frac{1}{L_e} \ln(1 + R_a - R_s)$$

and where:

- R_i is the waveguide radius,
- R_s is the sine-squared region end radius
- R_a is the aperture radius,
- L_s is the sine squared region length,
- L_e is the exponential region length,
- A modulates the sine square profile.

Besides the already cited data, the parameters chosen for the feed-horn profile are:

- R_s : 7.923 mm
- $L_s/(L_s + L_e)$: 0.75
- A : 0.5

After profiling, a refinement of the waveguide diameter and corrugations depth was done to adjust the bandwidth center. Also a refinement of the first corrugation width was done to optimize the return loss. The final design obtained is shown in Figure 5.1.

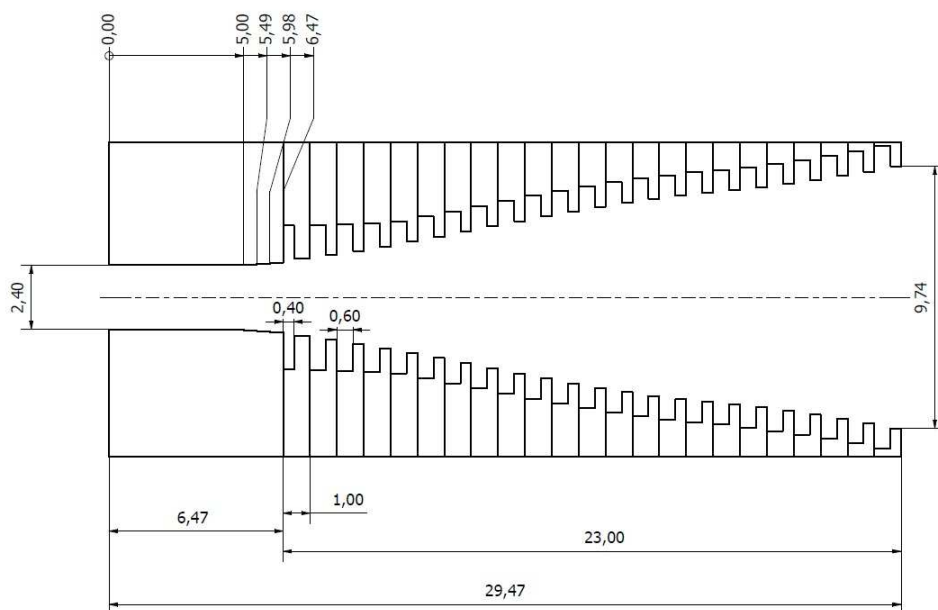


Figure 5.1: The electromagnetic design of the dual-profiled feed-horns realized.

5.1.2 Simulation of performance

The performance simulations and the refinement of the electromagnetic design was performed with the ©SRSR-D software of France Telecom. SRSR is a software for the analysis of radiating structures with symmetry of revolution. The calculation method consist in determining the currents on the radiating structure by solving scalar integral equations. The unknown current is expressed analytically along the azimuth angle, hence the problem reduces to one-dimensional equations. Once the currents are determined, the radiated field can be computed in the near-field or far-field regions. The computed data are:

- the reflection coefficient at the waveguide input (RL),
- the gain and the directivity,
- the near-field or far-field radiation pattern on the principal planes: E, H, $\pm 45^\circ$ copolar and $\pm 45^\circ$ crosspolar.

The great reliability of the SRSR software was already tested, among others, in [30]. Being the software designed for structures with symmetry of revolution, the simulation were performed on an single feed-horn, without taking

into account for the hexagonal shape of the entire module neither for the presence of the others feed-horns.

The calculated beam pattern of the design in Figure 5.1 for the E, H, 45 and 45-crosspolar planes are shown in Figures 5.2, 5.3, 5.4, 5.5, 5.6, respectively at 90, 95, 100, 105, 110 GHz. Assuming the revolution symmetry the ± 45 co-polar beam pattern are identical, and the same for the ± 45 cross-polar, hence only one plane for each is shown.

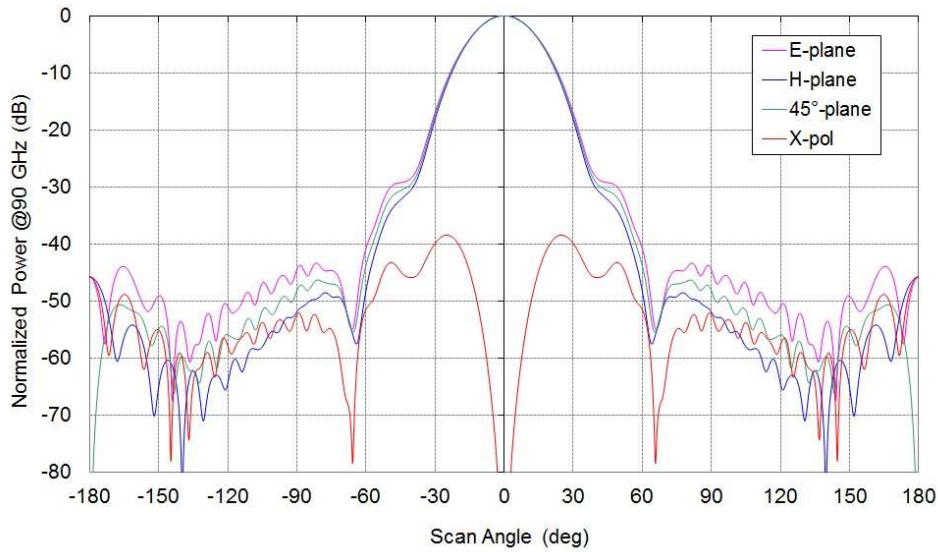


Figure 5.2: The calculated beam pattern of the design in Figure 5.1 for the E, H, 45 and 45-crosspolar planes at 90 GHz.

In Figure 5.7 is shown the simulated return loss in the entire W band. In Figures 5.8 and 5.9 are shown respectively the trend in W band of directivity and cross polarization.

5.2 Mechanical design

In order to be compliant to the compactness requirement, the module was designed as composed of 7 elements, displaced on an honeycomb lattice, then on the vertexes of equilateral triangles. The shape of the module is hexagonal with a central feed-horn surrounded by the other six elements. This displacement and shape enable the compactness of the single module and also of an array composed of such modules, again displaced as an honeycomb lattice.

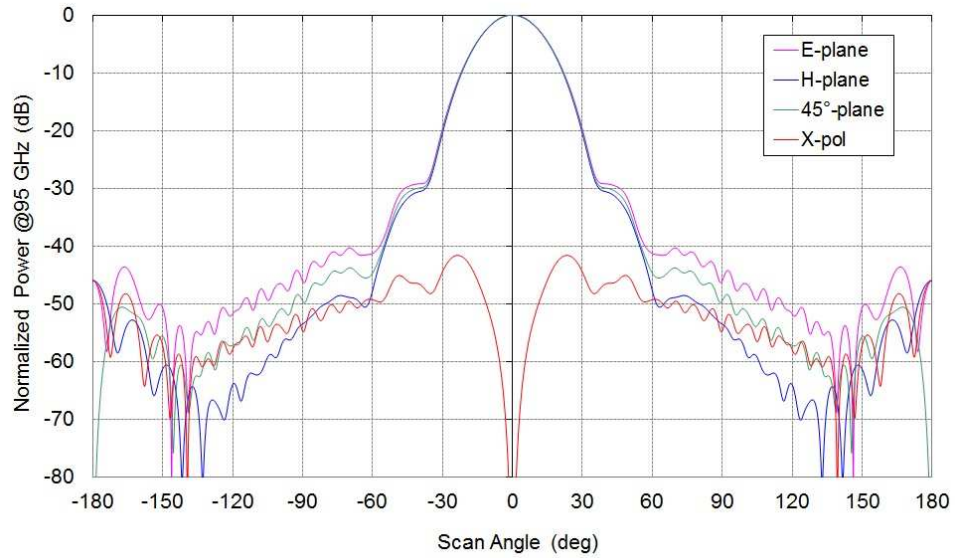


Figure 5.3: The calculated beam pattern of the design in Figure 5.1 for the E, H, 45 and 45-crosspolar planes at 95 GHz.

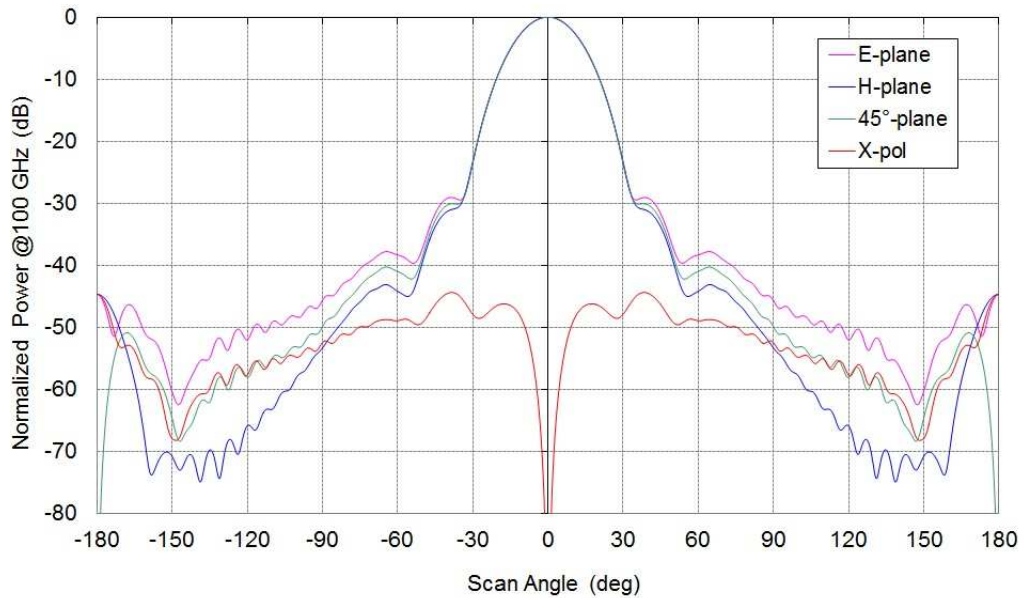


Figure 5.4: The calculated beam pattern of the design in Figure 5.1 for the E, H, 45 and 45-crosspolar planes at 100 GHz.

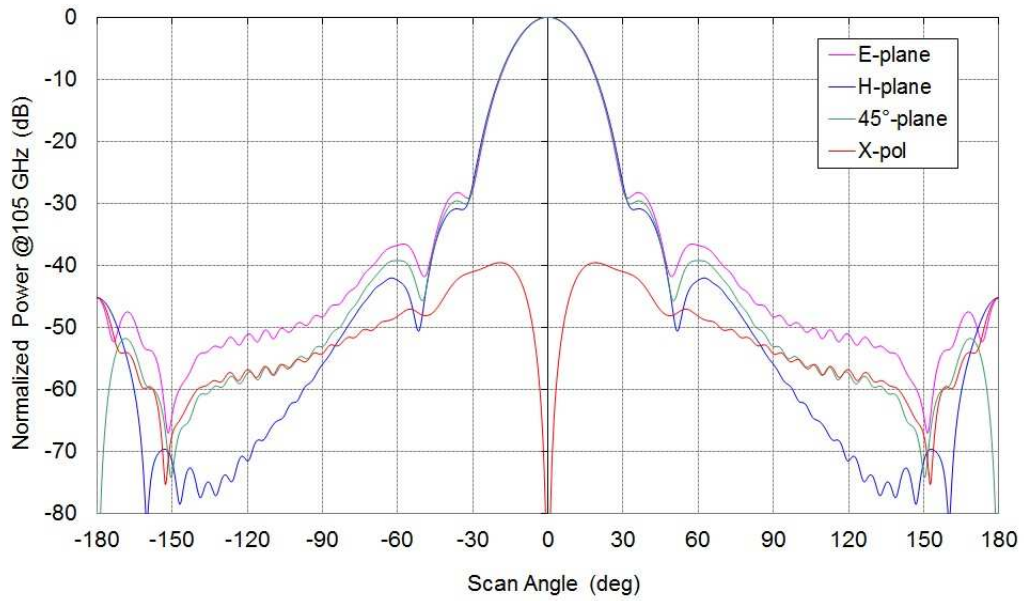


Figure 5.5: The calculated beam pattern of the design in Figure 5.1 for the E, H, 45 and 45-crosspolar planes at 105 GHz.

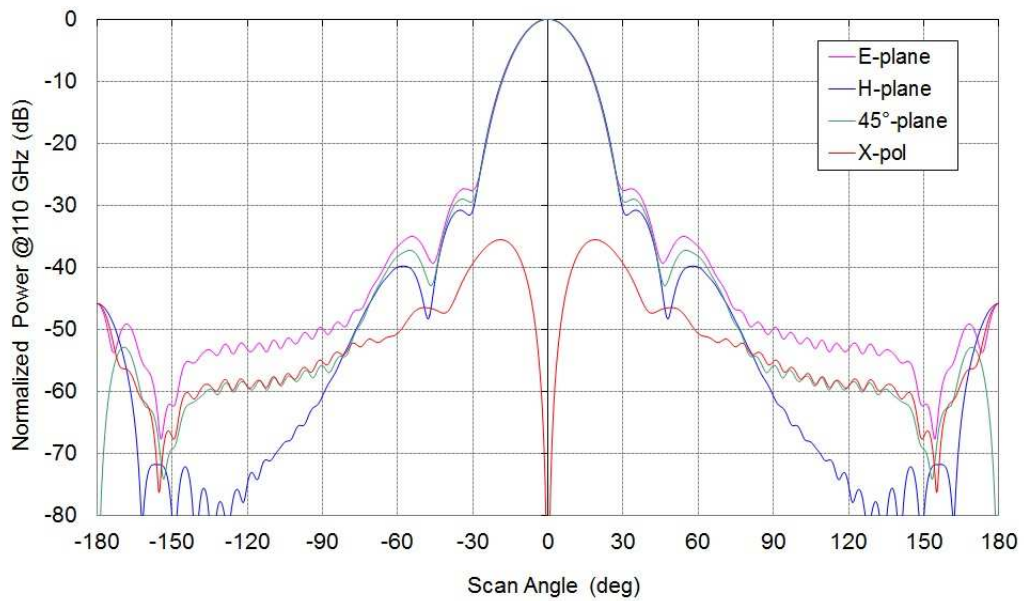


Figure 5.6: The calculated beam pattern of the design in Figure 5.1 for the E, H, 45 and 45-crosspolar planes at 110 GHz.

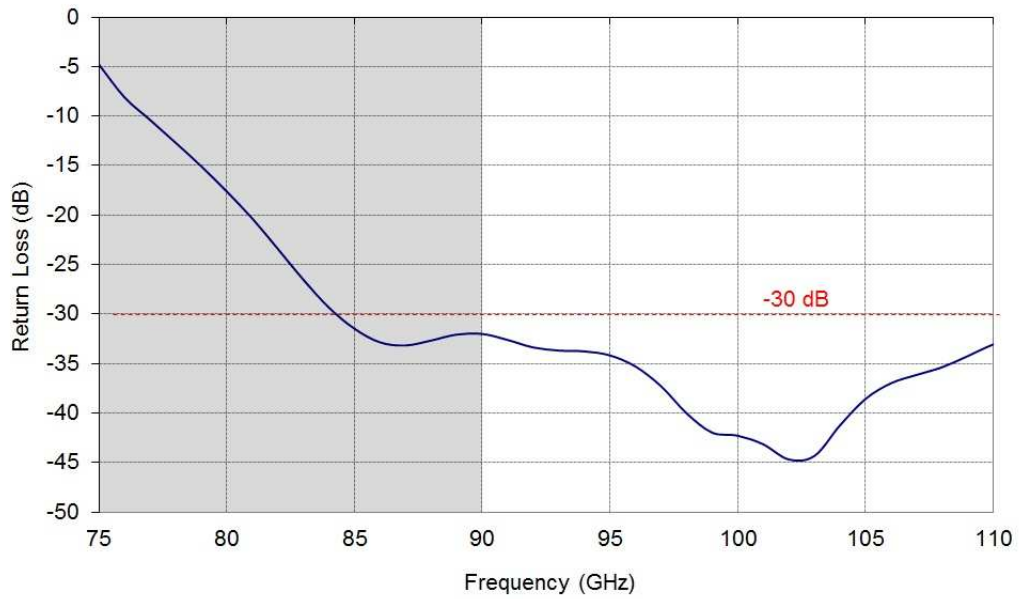


Figure 5.7: The calculated return loss of the design in Figure 5.1 on the entire W band. In white background the band of interest.

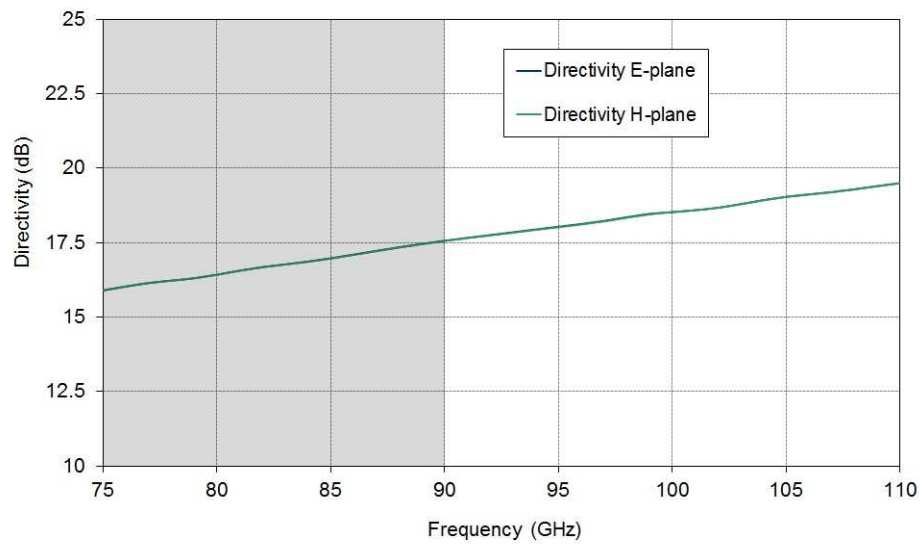


Figure 5.8: The calculated directivity of the design in Figure 5.1 for the E and H planes. In white background the band of interest.

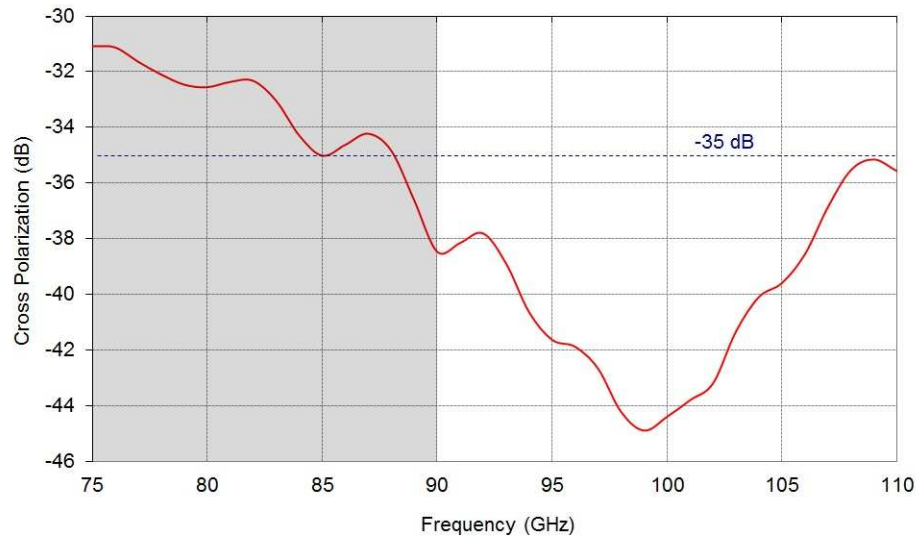


Figure 5.9: The calculated cross polarization relative to the maximum of the ± 45 degrees planes, on the entire W band. In white background the band of interest.

As mentioned, the technique chosen for the realization of the prototype is the non-bonded platelet technique. The feed-horns are then realized in transversal layers with metallic plates fixed together with screws. The screws are displaced at the centers of the equilateral triangle on which lies the feed-horns, in order to ensure compactness and at the same time a uniform distribution of tightening force and pressure on the plates.

To align the plates three holes, one every 120 degrees, are provided on three vertexes of the hexagonal rim of the module. In that way an external system of three alignment pins can be used to align the plates. Being the alignment pins external to the module they do not contribute to its weight and do not require extra space inside it.

5.2.1 Materials

The chosen materials are two aluminum alloys: Al6082 Al-Mg-Si-Mn (Anticorodal) for the plates, and Al70750 Al-Zn-Mg-Cu (Ergal) for the screws, compliant with the lightweight and high conductivity requirements. The main characteristics of these aluminum alloys are their low specific weight: 2.69 g/cm^3 for the Al 6082 and 2.81 g/cm^3 for the Al 7075, their excellent workability and corrosion resistance, their ability to be anodized and their good strength. The main difference between Al6082 and Al7075 is the tensile

strength that is respectively 310 N/mm^2 and 560 N/mm^2 . Moreover their thermal expansion coefficients are quite similar: $23.4 \cdot 10^{-6} \text{ K}^{-1}$ for the Al6082 and $23.5 \cdot 10^{-6} \text{ K}^{-1}$ for the Al7075, thus allowing to apply a great screw load to properly fix the plates, and to stabilize the prototype with respect to thermal contractions. In addition at cryogenic temperature the force should be just a bit more tighten, due to the differential thermal contraction.

5.2.2 Design of the plates

To partition the module in plates, it was chosen to realize an entire corrugation, with a tooth and a groove, for each plate (Figure 5.10), this allow to:

- halve the number of plates required w.r.t. realizing a tooth or a groove in each plate,
- minimize the alignment errors reducing the number of parts to align,
- allow to realize the corrugation with unique single-side machining.

Moreover, as seen before each corrugation has a length of 1 mm, this means that plates of 1 mm thickness are required. This choice simplifies the retrieval of the metal sheet for the realization of the plates, as the 1 mm thickness is a commercial standard..

The first plate, where is realized the feeding smooth waveguide, plus 3 matching steps (see Figure 5.1), has a greater thickness to allow the realization of: the matching waveguide steps, the holes for the flange interface, and the counterbores to accommodate the heads of the screws that assemble the plates. In that way the back surface of the module is flat and easy to interface, as in Figure 5.11.

The last plate, that hosts the feed-horn aperture with its (last) corrugation, required a particular design. The last plate, for the same flatness reason of the first plate and for compactness, have to accommodate the thread for the screws tighten, and requires a certain thickness. The thread length required for a reliable tighten, corresponds to 1.5 times the diameter of the thread itself. The screws chosen for assemble and fasten the plates are twelve DIN 912-M3 Ergal screws. The choice of the screws number and dimension was taken from the experience of a previous prototype [30] and in relation to the the choice of materials. Then the last plate must be at least 4.5 mm thick. In order to obtain a flat surface at the aperture plane of the feed-horns the holes are blinds. To ensure a safety fastening margin and avoiding the contact of the end of the screws with the bottom of the blind hole, a factor

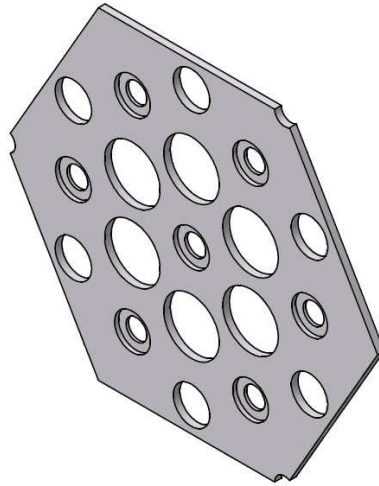


Figure 5.10: Design of a plate with an entire corrugation with a tooth and a groove for the seven feed-horns holes. At the centers of the equilateral triangle on which lies the feed-horns are displaced the screws through holes. On three vertexes of the hexagonal rim there are the centering (partial) holes.

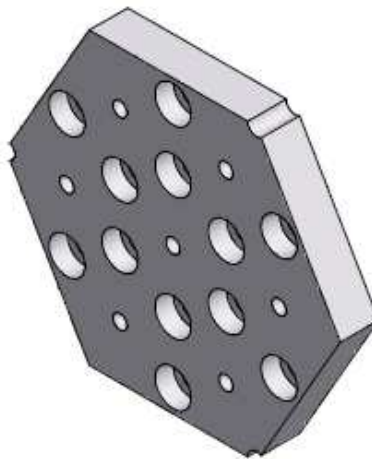


Figure 5.11: Design of the first (base) plates with the counterbores for the screws heads.

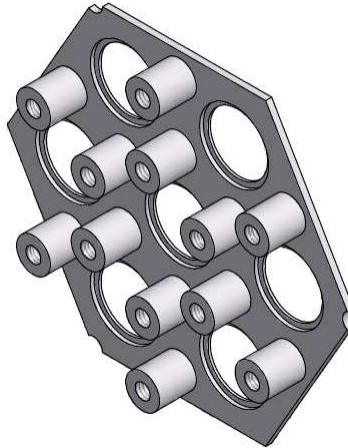


Figure 5.12: Design of the last (head) plate with the 12 threaded rods for screw fastening. The plate is designed as grinded from a unique piece, realizing the rods and leaving the 1 mm thickness for the realization of the seven corrugation.

2 was chosen for the thread length. Adding a 1 mm thickness for the hole bottom, the total thickness of the last plate results of 7 mm.

Nevertheless the last plate hosts only one corrugation of 1 mm thickness, otherwise undercuts machining would be necessary, requiring more times and expansive customized complex tools. To realize a single corrugation the last plate was designed as a plate of 1 mm thickness with 12 rods in the position of the screws, each with the blind threaded hole at the center and with the necessary diameter. The rods diameter was chosen as tabulated for the metric standard bolts, that for M3 screws is 5.5 mm. The resulting design of the last plate is shown in Figure 5.12.

5.2.3 Design optimization

Once fixed the electromagnetic design and some mechanical constraints, as the screws number, diameter and position, an optimization is required in the mechanical design for the maximum compactness and lightweight.

The leading component that drives the compactness is the last head-plate, in which have to be realized the largest machining: the horns first corrugations and the rods for the screws fastening. The maximum compactness would be reached if the horns first corrugation would be close each other, considering a certain material between them. At the center of each three feed-horns it is placed a rod for the screw fastening. Then the diameter of the rod have to be taken into account for the minimum feed-horn dis-

tance. Also in this case the rod should be tangential to the feed-horns first corrugation, considering a certain necessary material between them.

The optimization is performed by a designing tool, written specifically in Visual Basic language. The tool needs the following input data:

- diameter of the groove of the first corrugation
- minimum desired material between the horn first corrugations,
- screws diameter,
- minimum desired material between screw rods and horn first grooves,
- minimum desired material between rim of the head plate and outer machining (the horn corrugation or the rod),
- # and angular position of the feed-horns
- # and angular position of the centering holes
- diameter of the centering holes

and calculates the following dimensions:

- *effective* distance between the horns apertures,
- *effective* material between the horn first corrugations,
- *effective* material between rim of the head plate and outer machining,
- position of the screws
- radii of the inscribed and circumscribed circle to the hexagonal rim.

Moreover the designing tool calculates, for each plate, the maximum diameter for the through holes for the screws, taking into account for a minimum material between them and the feed-horn holes. This minimum material was chosen equal to the minimum material needed between the horns first corrugations. This calculus allow to eliminate the excess of material, lightening the module. A screen shot of the designing tool is shown in Figure 5.13. The mechanical input and output data for the design optimization of the module are listed respectively in Table 5.1 and 5.2.

The final mechanical design is shown in Figures 5.14 and 5.15. In Table 5.3 are listed the final construction dimensions, with the holes diameters for the horns corrugations and for the through screws holes. In addition the width of the corrugations grooves are listed as “Z”, as all the holes are realized along the Z axis of the machine tool.

The screenshot shows a software interface with three tabs: "Parametri E.M. (Freq. 1)", "Parametri E.M. (Freq. 2)", and "Parametri Meccanici". The "Parametri Meccanici" tab is active. It is divided into "Input" and "Output" sections. The "Input" section contains 14 fields for defining geometry and assembly. The "Output" section shows calculated values for the same parameters. Below the "Output" section are two sub-sections: "Flangia" with a checkbox and a dropdown menu, and "Frame7" with two radio button options.

Input	Output
Inframetallo Minimo (mm)	Inframetallo Effettivo (mm)
M (mm)	Interasse (mm)
Sovrametallo (mm)	Sovrametallo Effettivo (mm)
Nr. Feed Horn	Posizione Tiranti Interni (mm)
Angolo Offset Horn (deg)	Posizione Tiranti Esterni (mm)
Nr. Tiranti Interni	R Circoscritto all'Esagono (mm)
Angolo Offset Tiranti Interni (deg)	R Inscritto all'Esagono (mm)
Nr. Tiranti Esterni	
Angolo Offset Tiranti Esterni (deg)	
D Fori Allineamento	
Nr. Fori Allineamento	
Angolo Offset Fori Allineamento (deg)	
Spessore superficie d'appoggio (mm)	

Flangia

Disegna flange standard sulla lamina di base

EIA designation (Standard US) WR4

Frame7

Modulo singolo

Moduli multipli

Figure 5.13: Screen shot of the designing tool. On the left the input data, on the right the calculated data.

Input data	value [mm]
first grove diameter	11.258
min. mat. between the first grooves	1
screws diameter	3
min. mat. between rim and outer machining	1
min. mat. between screw rods and first grooves	2

Table 5.1: Input data for the compactness and wight optimization with the designing tool.

Output data	value [mm]
<i>effective</i> mat. between horn first corrugations	6.739
<i>effective</i> distance between horns axes	17.846
<i>effective</i> mat. between hexagon rim and outer machining	1
position of inner screws	10.303
position of outer screws	20.606
radii of circumscribed circle to the hexagonal rim	28.124
radii of inscribed circle to the hexagonal rim	24.356

Table 5.2: Output data obtained from the designing tool, relative to the input data listed in Table 5.1

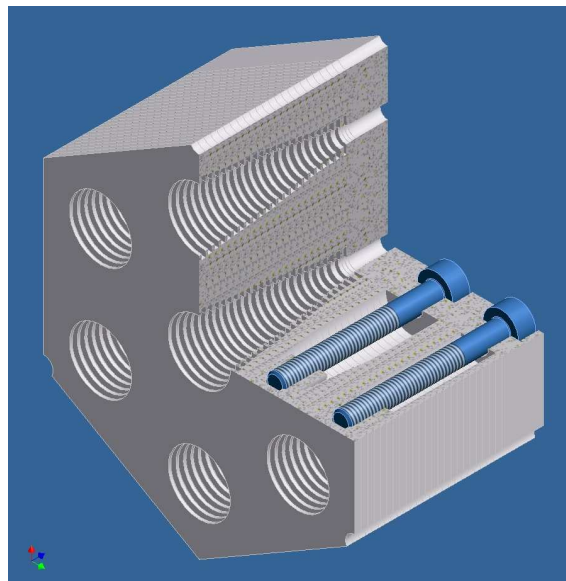


Figure 5.14: Sectional CAD view of the final design of the 7-element module array. As obtained with the optimization designing tool with the input data listed in Table 5.1.

Plate	Tooth \varnothing	Groove \varnothing	Z	In screw hole \varnothing	Out screw hole \varnothing
23	9.744	11.258	0.4	2.500	2.500
22	9.360	10.874	0.4	5.500	5.600
21	9.015	10.529	0.4	5.884	5.600
20	8.705	10.219	0.4	6.229	5.600
19	8.425	9.939	0.4	6.539	5.600
18	8.174	9.688	0.4	6.818	5.600
17	7.948	9.462	0.4	7.070	5.600
16	7.774	9.288	0.4	7.296	5.600
15	7.568	9.082	0.4	7.469	5.600
14	7.324	8.838	0.4	7.675	5.600
13	7.044	8.558	0.4	7.920	5.600
12	6.732	8.247	0.4	8.200	5.600
11	6.394	7.908	0.4	8.379	5.600
10	6.033	7.547	0.4	8.379	5.600
9	5.658	7.172	0.4	8.379	5.600
8	5.273	6.787	0.4	8.379	5.600
7	4.886	6.400	0.4	8.379	5.600
6	4.504	6.018	0.4	8.379	5.600
5	4.134	5.648	0.4	8.379	5.600
4	3.782	5.537	0.4	8.379	5.600
3	3.454	5.450	0.4	8.379	5.600
2	3.155	5.391	0.4	8.379	5.600
1	2.889	5.367	0.6	8.379	5.600

Table 5.3: The final construction dimensions (in mm) of the prototype. In the first two columns are listed the holes diameters for horns corrugation, as tooth and groove. In the third column is listed, as Z, the width of the groove. In the two last columns are listed the diameters of the through screws holes.

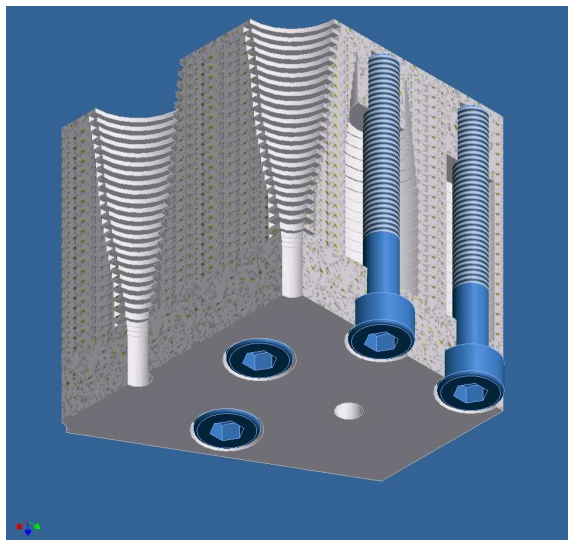


Figure 5.15: Sectional CAD view complementary to the section shown in Figure 5.14. Here are clearly visible the through holes for the screws, enlarged where possible to reduce the weight of the module.

5.3 Fabrication

The prototype has been realized at the workshop of the Physics Department-University of Milan, with the 3-axes CNC machine tool “Guldoni GV-94”.

The 1 mm thick plates were realized from an Anticorodal sheet, already of the right thickness directly from the producer, with a measured tolerance of ± 0.01 mm. The first base-plate and the last head-plate were realized from Anticorodal slabs of 10 mm thickness with the same tolerance. All the 22 1-mm-thick plates were realized from a unique sheet of 300x400 mm, taking into account for the space between them, needed for the cutting of the hexagonal shape. The base and head plates were realized from single presized slabs.

The CNC machine tool were programmed with ISO code. For the base and head plates single custom codes were written, while for the 22 intermediate plates a single *parametric* code was written. The parametric code for the intermediate plates allow to “cut and paste” all the required dimensions, both the machining dimensions as listed in Table 5.3 and the positioning dimensions as listed in Table 5.2. In that way the transcription errors are avoided and the code is able to realize, in series, only the required plates, for example in case of manufacturing errors.

All the machining were programmed in apposite sequence that allow the

minimization of the working time and errors. In particular the general realization sequence was: all centering holes, antenna trough holes, antenna corrugations (or steps in the base-plate), screws holes, aligning holes, cutting of the hexagonal edges.

The workpieces were fixed inside the machine tool by means of a vacuum clumping system. This system consists of a metallic plane, connected to a vacuum pump, and aspirated by means of little slots dug into it. A special rubber sheet is interposed between the slotted plane and the workpiece, to increase the coefficient of friction and for masking the zone where the vacuum is desired by piercing it (Figure 5.16). This system allows for secure and reliable fastening, without the need for custom holders and avoiding the risk of deforming the thin sheets. Moreover this clumping system allows a working plane free from obstacles, making it more quickly and safely to work.

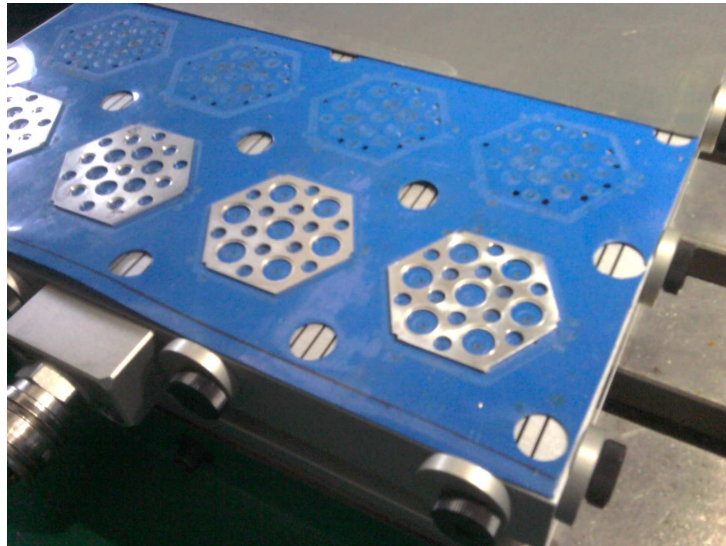


Figure 5.16: The vacuum clumping system for the machining of the plates. Under the properly pierced blue rubber are visible the suction slots. At the bottom is visible the connection through the vacuum pump system. The waste material, after the machining, is already removed in the picture to show the rubber vacuum mask and the slotted plane.

After carefully prepared the rubber mask, piercing it properly, the Anticorrosive sheet was positioned over the mask and the plates were realized executing the ISO codes. The same procedure was applied for the base and head plates separately. All the plates realized are shown in Figure 5.17, in Figure 5.18 details of the base-plate and head-plate.

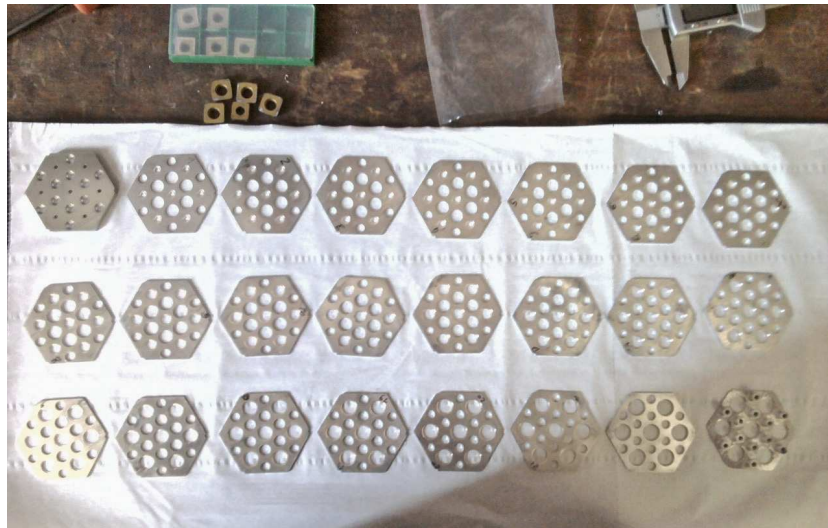


Figure 5.17: All the plates realized and ordered in the mounting order, from upper left (base-plate) to bottom right (head-plate). It can be seen as increasing the horns holes diameter, decreasing the screws holes diameter.

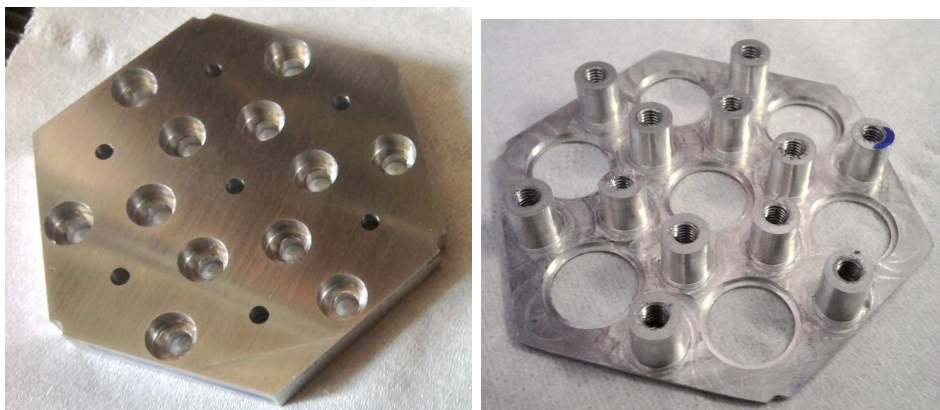


Figure 5.18: Details of the base-plate (left) and head-plate(right).

As already mentioned, all the plates were worked from only one side, in order to avoid repositioning and then minimizing manufacturing errors and times. The only exception was the realization of the counterbores in the base plates, but manufacturing errors in this machining do not compromise the performance of the module, provided that the screws heads come into. The maximum manufacturing error for all the plates was measured to be ± 0.03 mm.

5.3.1 Assembling

After the realization and a ultrasonic cleaning process the plates were assembled together. The alignment of the plates were obtained by means of the three 3 mm diameter centering holes, realized in each plate, aligning them with three rectified stainless steel pins. The plates were aligned tightening them all together in a late spindle with three jaw chucks on which were mounted the rectified pins. In Figure 5.19 is shown the tightening of the base plate alone in the spindle.

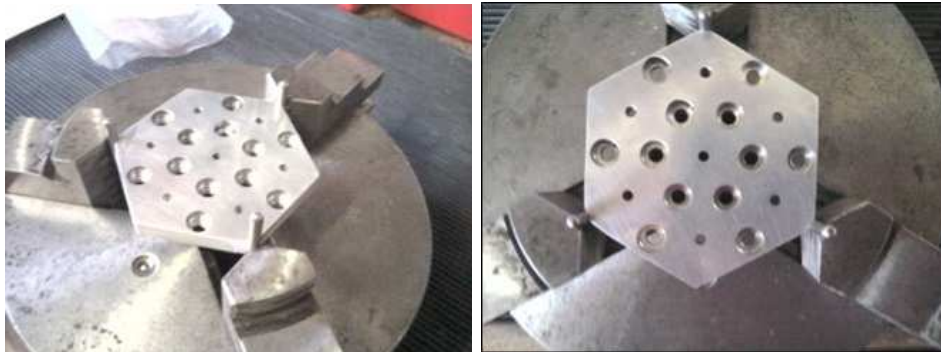


Figure 5.19: The alignment of the plates were obtained by means of the three 3-mm centering holes realized in each plate, aligning them with three rectified stainless steel pins. The plates were tightened all together in a late spindle with three jaw chucks on which were mounted the pins.

While the plates were aligned in the spindle, the twelve Ergal screws were tighten with a torque wrench, applying the same torque. The module assembled, shown in Figures 5.20 and 5.21, has a weight of 111 grams.

In order to loading the screws with the maximum permissible load, the Equation 5.5 was applied, that gives the relation between the applied momentum M_{app} with the torque wrench and the force F_V loading the screw

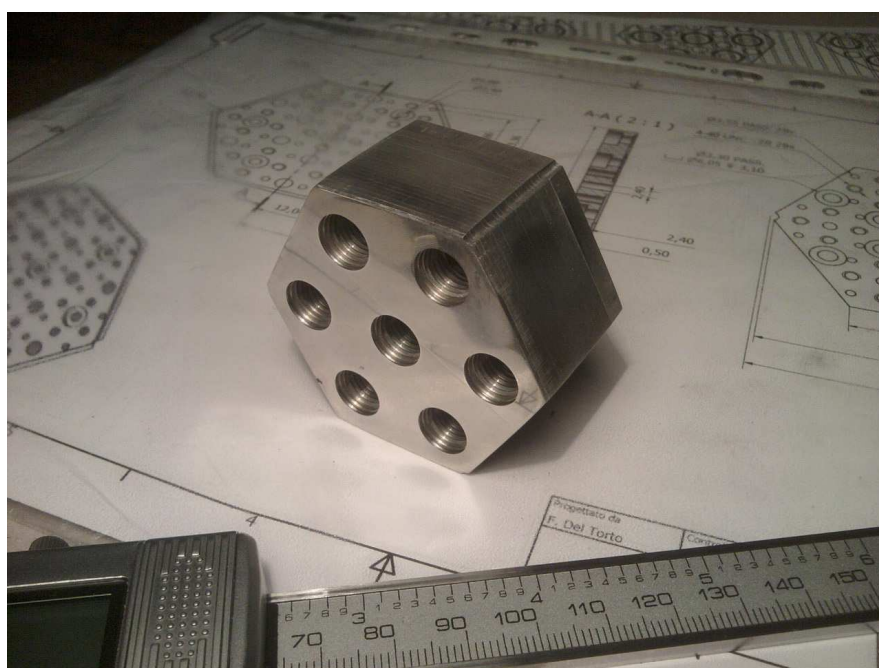


Figure 5.20: The feed-horns module assembled, seen from the feed-horns apertures.

[35]:

$$M_{app} \approx F_V \left[0.16p + 0.58\mu_{th} + \mu_{uh} \frac{d_{uh}}{2} \right]. \quad (5.5)$$

In the above relation p and d_{uh} are the pitch and the under-head diameter of the screw respectively; μ_{uh} and μ_{th} are the friction coefficients at the head and at the thread of the screw respectively. The issue of the friction coefficient, and in general of the threaded fasteners are complex problems, beyond the scope of this work. Nevertheless, considering the aluminum alloys used, a realistic value of 0.35 can be taken either for μ_{uh} and μ_{th} [35].

Before tighten the M3 screws, some tests were performed on a testing head-plate to find the torque limit corresponding to the tensile strength limit. This torque limit was experimentally founded at 1 Nm, corresponding from Equation 5.5, to a loading force of about 1227 N and a load of about 250 N/mm², considering the 2.5 mm core diameter of the DIN 912-M3 screws. The 250 N/mm² load value is still below the nominal yielding limit of 490 N/mm² and in fact the tested screws did not break at the shank, but its head was stripped. To avoid breakage of the screws heads, a torque of 0.6 Nm were applied to the twelve screws, corresponds from the Equation 5.5 to a loading force of about 687 N per screw, for a total tightening force of about 8246 N. The corresponding load for each M3 screw is about 140 N/mm², well below the yielding limit of 490 N/mm².

Vibrational and thermal analysis were performed by Thales Alenia Space Italia considering a 0.9 Nm of torque for each screw. The analysis confirmed the reliability of the design in space launch and cryogenic conditions with good margin of safety [34].

5.4 Electromagnetic Tests

Typical electromagnetic performance measured for antennas are the co-polar and cross-polar beam pattern, the return loss and the insertion loss. All these performance are measured in the band of interest. For the realized prototype beam pattern and return loss were measured, while the insertion loss was not measured. A reliable insertion loss measurement would require a not still available customized setup, that allow the matching of the horn aperture with the instrument. Moreover the measurements were performed with the aim of verify the goodness of design and realization. An eventual insertion loss problem could be resolved by a surface deposit of an high conductive material as silver or gold, as the insertion losses depends principally from the conductivity of the materials.

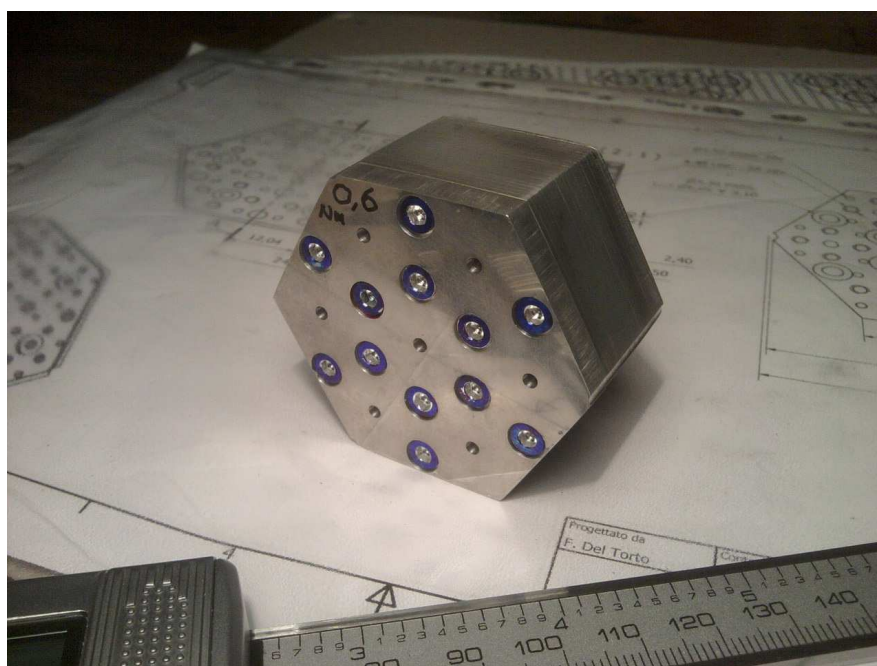


Figure 5.21: The feed-horns module assembled, seen from the circular waveguide apertures. Coloured in blue are visible the twelve Ergal screws.

The electromagnetic tests were performed at room temperature at the “Istituto di Fisica del Plasma-CNR Milano”. The experimental setup was composed principally by a 7X4X4 m anechoic chamber (for the beam pattern measurements) and a vector network analyzer ABmillimetre MVNA 8-350-4.

5.4.1 Beam pattern

As mentioned antennas are passive components, then are reciprocal components and their beam pattern can be measured either transmitting or receiving the signal with them. To measure the beam pattern of an antenna a second antenna is necessary to measure the signal transmitted by the antenna under test or to transmit the signal to be measured with the antenna under test.

Antenna beam pattern can be obtained by measuring the near-field at the antenna aperture and transforming it by the Fourier Transform into the far-field, or by measuring directly the radiating far-field, as in this case. The antenna beam pattern can be measured in co-polarization and in cross-polarization by orienting the receiver and the transmitter with polarizations parallel (co-polar) or orthogonal (cross-polar) to each other. Moreover, in the far-field configuration the antenna under test, or the second transmitting/receiving antenna, must be rotated around the antenna under test phase center. The phase center is a point where the irradiated waves may be thought to be emitted in terms of their phase. Centering the feed-horn in the phase center allow to obtain the same electrical path of the irradiated waves as the feed-horn is rotated during the measurement.

Experimental setup

In our configuration the beam pattern was measured in transmission, rotating the antenna under test in the horizontal/azimuth plane and receiving the signal from a fixed corrugated horn.

Being an array of seven feed-horns each horn phase center had to be centered on the rotation axis before measuring its beam pattern. The alignment of the antennas under test was obtained by an x-y positioner, on which the array were mounted by means of a clumping system that allows the positioning along the antenna axis. The array fixed on the x-y positioner was then mounted on a motorized rotating positioner. All the positioners and the clumping system were shielded with absorber material $\text{\textcircled{R}}\text{ECCOSORB}$, in order to avoid spurious signal reflections.

Both the array under test and the receiver antenna were positioned inside the anechoic chamber that, being entirely shielded with absorbing material,

minimize signal reflections and external disturbance. In that way the signal measured by the receiver comes only (or almost) from the plane wave irradiated from the antenna under test. In order to obtain a good approximation of a plane wave and then measuring the antenna under test far-field, the receiver must be positioned in its radiating far-field region. The far-field region starts at a distance $2D^2/\lambda$, where D is the antenna aperture and λ is the considered frequency. The distance between the array and the receiving antenna was about 3 meters, many times greater than the ~ 60 mm of the far-field position of the antenna under test.

To measure the various ϕ -cut planes the antenna under test (ie the whole array) and the receiver were rotated, of the same angle, around their axes once they were aligned with a laser. In order to minimize the tests duration, once chosen a ϕ -cut plane and aligned the polarization plane, the beam pattern was measured, at all the required frequencies, for each feed-horn. The feed-horns were then connected in sequence to the VNA and their phase centers were centered with the known geometrical data of the array. The procedure was then repeated for each plane. The feed-horns were numbered from the central one as the #1 and proceeding clockwise, from the rear view, to the #7. The positions of the feed-horns in the four configuration for the different planes measurements are shown in Figure 5.22

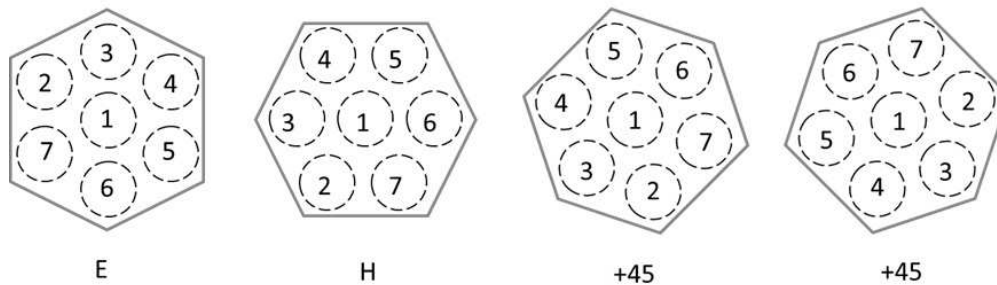


Figure 5.22: Rear view of the positions of the seven feed-horn, in the four configurations for the measurements of the E, H, +45 and -45 planes beam pattern.

Measurements

Typical beam pattern measurements are realized for the co-polar principal planes: E($\phi=0$), H, +45 and -45 degrees and for the cross-polar principal planes at +45 and -45 degrees, where the cross-polarization is maximum. Moreover the θ range spanned is limited at $-90 \leq \theta \leq 90$ degrees, as

most of the power is received from the front directions and where the receiver/transmitter attached to the antenna does not affect the measurement. For the realized prototype the E, H, ± 45 co-polar planes and the ± 45 cross-polar planes were measured at 90, 95, 100, 105 and 110 GHz for all the seven horns, for a total of 210 beam patterns measured.

In Figures 5.23 to 5.29 the beam pattern of the seven feed-horns is shown, measured on the six principal planes at the central frequency of 100 GHz. With regards to the co-polar planes, for all the seven feed-horns the main beam angular regions, between ± 30 degrees, are very symmetric with differences ≤ 1 dB. At higher angle and below the -30 dB level, are visible asymmetries at the level ≤ 5 dB, together with noisy fluctuations ≤ 3 dB. Those asymmetries have similar features for the feed-horns #1, #2, #3, #6, #7, and slightly different for the feed-horn #4 and #5. For what concerns the cross-polarization pattern some considerations will be done briefly.

In Figures 5.30 to 5.33 are shown for each co-polar plane, at the central frequency of 100 GHz, the comparison between the seven feed-horns with the corresponding simulation. The asymmetries below the -30 dB level are more evident in the E-planes (Figure 5.30), moreover the measured main beams are slightly larger than simulated, and slightly (≤ 2 dB) asymmetric in the ± 45 -planes (Figures 5.32 and 5.33). With the exception of the E-planes second side-lobes, the measured beam pattern do not exceed the simulation more than ~ 2 dB at -30 dB level.

As mentioned the six-planes beam pattern of the seven feed-horn was also measured in the band of interest at the frequencies of: 90, 95, 100, 105, and 110 GHz. To show the frequency trend of the co-polar planes, in Figures 5.34 to 5.37, are plotted the beam pattern of the feed-horn #1 for all the five measured frequencies. The frequency trend can be assumed similar for the others feed-horns, with differences between them at the same level of those showed in the previous Figures 5.30, 5.31, 5.32, 5.33. As expected the beam pattern spreads around the central frequency, but with the first side-lobes/shoulder that exceed the -30 dB limit for almost all the plane at 90 and 95 GHz, with a maximum excess of ~ 4 dB for the E-plane. At the same time, always for the first shoulders in all planes, at the frequency of 110 GHz there is a leakage of power with respect to the -30 dB limit.

However the directivity of all the seven feed-horns at the five measured frequencies shown good agreement with the simulation (Figure 5.38). All the feed-horns have very similar directivity, with differences < 0.1 dB. In Figure 5.38 also the simulated directivity is plotted, which lies 0.37 dB below the mean directivity of the seven feed-horns at 90 GHz.

The cross-polarization beam patterns are very different from those simulated and between the +45 and -45 planes (Figures 5.39 and 5.40). Moreover

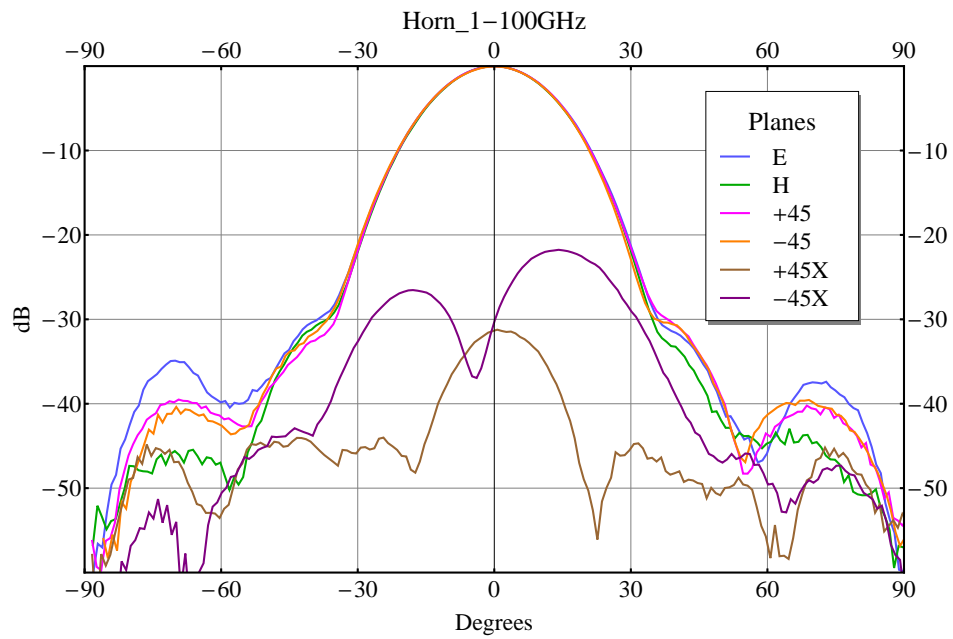


Figure 5.23: Measured beam pattern of the feed-horn #1 at the central frequency of 100 GHz.

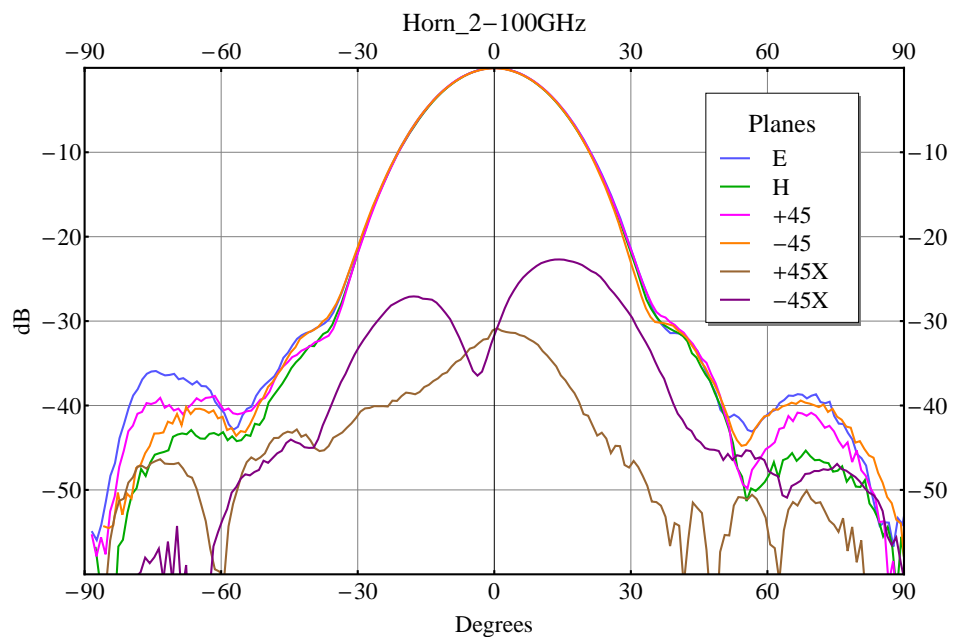


Figure 5.24: Measured beam pattern of the feed-horn #2 at the central frequency of 100 GHz.

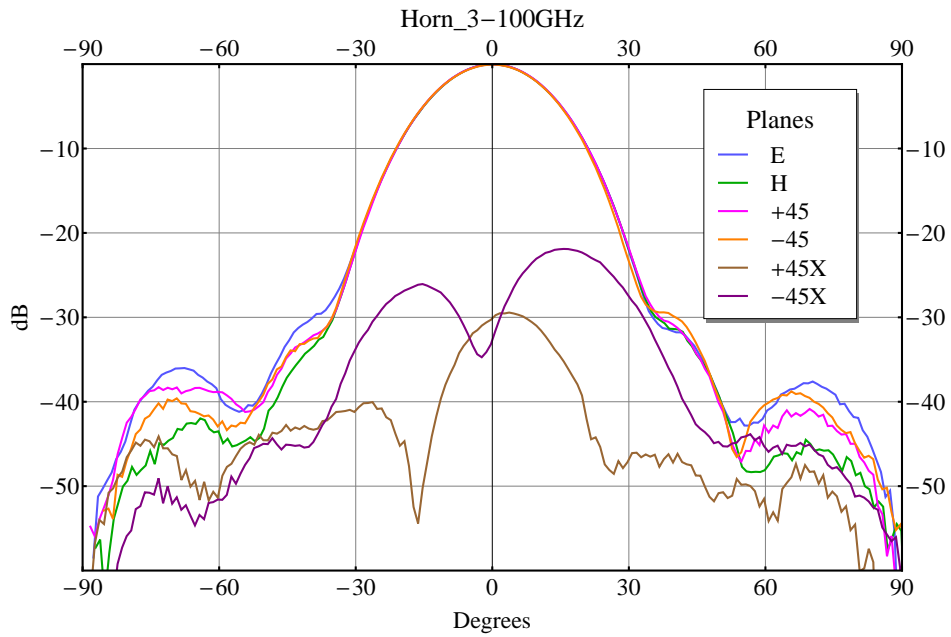


Figure 5.25: Measured beam pattern of the feed-horn #3 at the central frequency of 100 GHz.

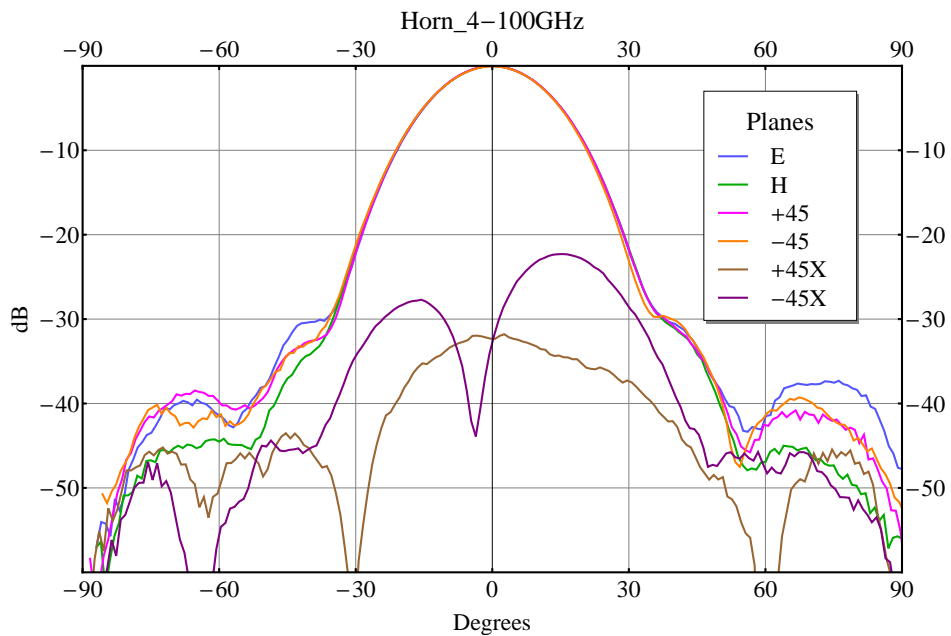


Figure 5.26: Measured beam pattern of the feed-horn #4 at the central frequency of 100 GHz.

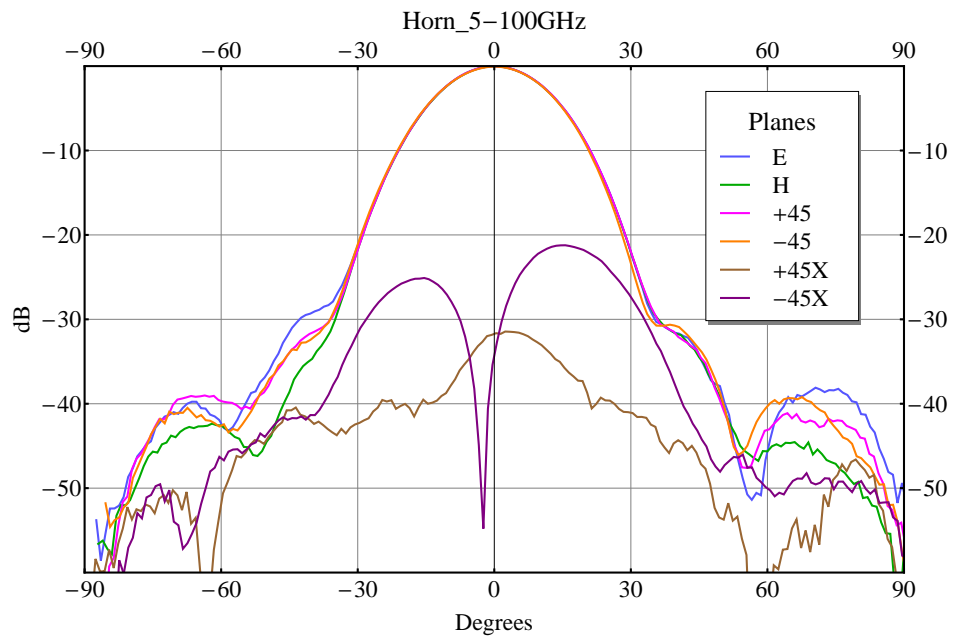


Figure 5.27: Measured beam pattern of the feed-horn #5 at the central frequency of 100 GHz.

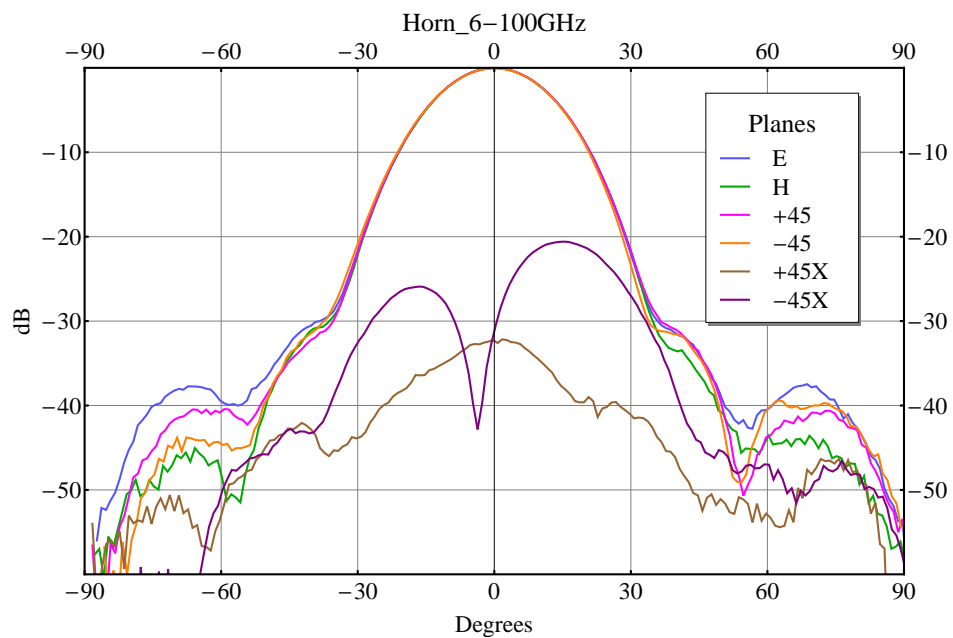


Figure 5.28: Measured beam pattern of the feed-horn #6 at the central frequency of 100 GHz.

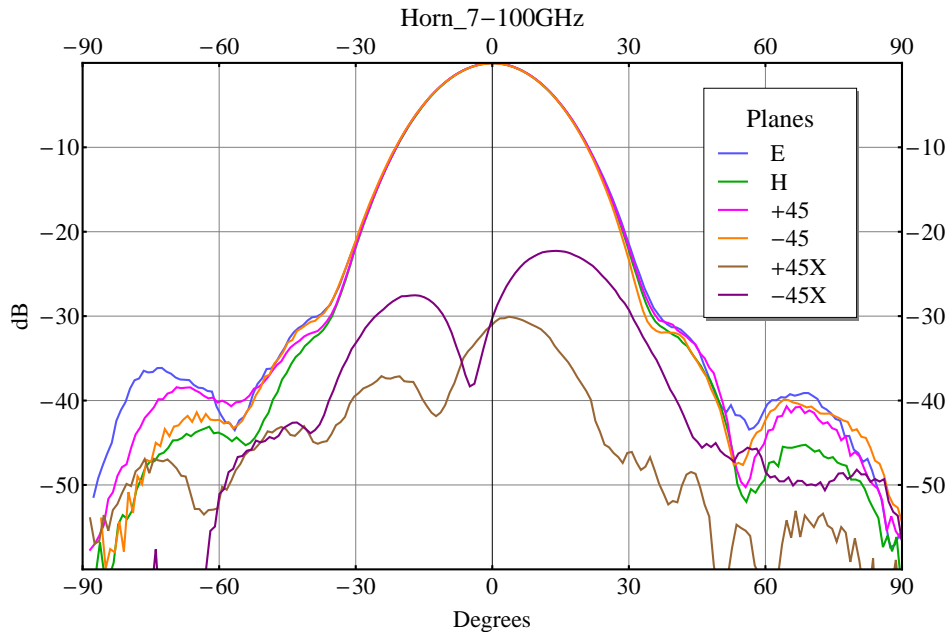


Figure 5.29: Measured beam pattern of the feed-horn #7 at the central frequency of 100 GHz.

for the +45 plane (Figure 5.39) the measured beam pattern differ from each others, in contrast with all the other planes that are similar between the different feed-horns. Finally an excess of power is present at 90 and 95 GHz for both the +45 and -45 planes, as shown in Figures 5.41 and 5.42 for the feed-horn #1. Also in this case the frequency trend can be assumed similar for the others feed-horns, with differences between them at the same level of those showed in the previous Figures 5.30, 5.31, 5.32, 5.33.

Considerations

A first important consideration needs to be done about the difference between the level of simulated and measured cross-polar beam pattern. The central ($\theta=0$) cross-polarization level of the *receiving* antenna was measured to be -35 dB. This imply the impossibility to measure the expected lower cross-polarization signal of the antennas under test. In fact the central level of the measured cross-polarization for the feed-horn array is at the same -35 dB level for all the feed-horns in both +45 and -45 planes.

Another consideration needs to be done about the anechoic chamber of the beam pattern experimental setup. The anechoic chamber was equipped

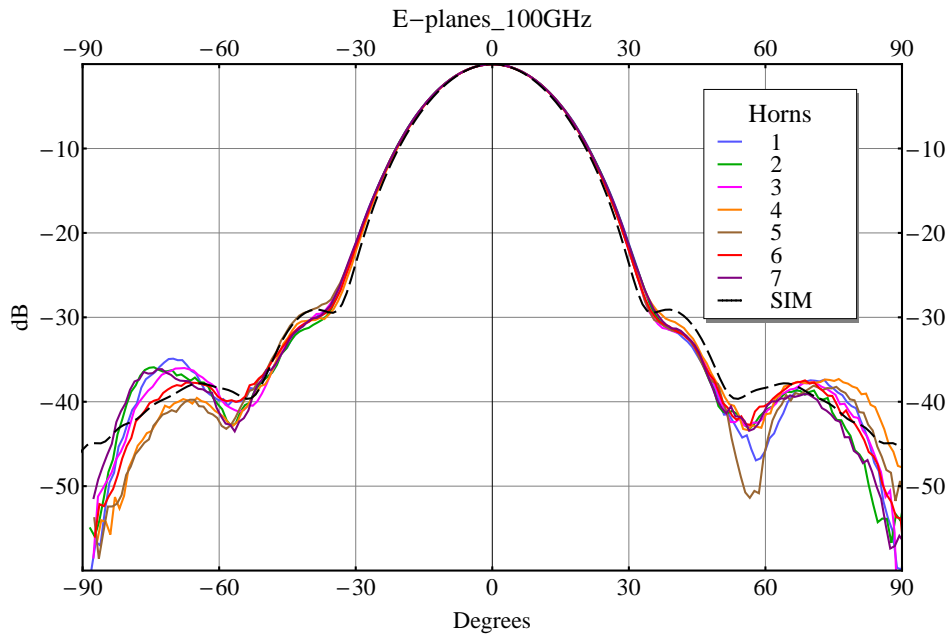


Figure 5.30: Comparison of the E-planes, @100 GHz, for all the seven feed-horns with the relative simulation.

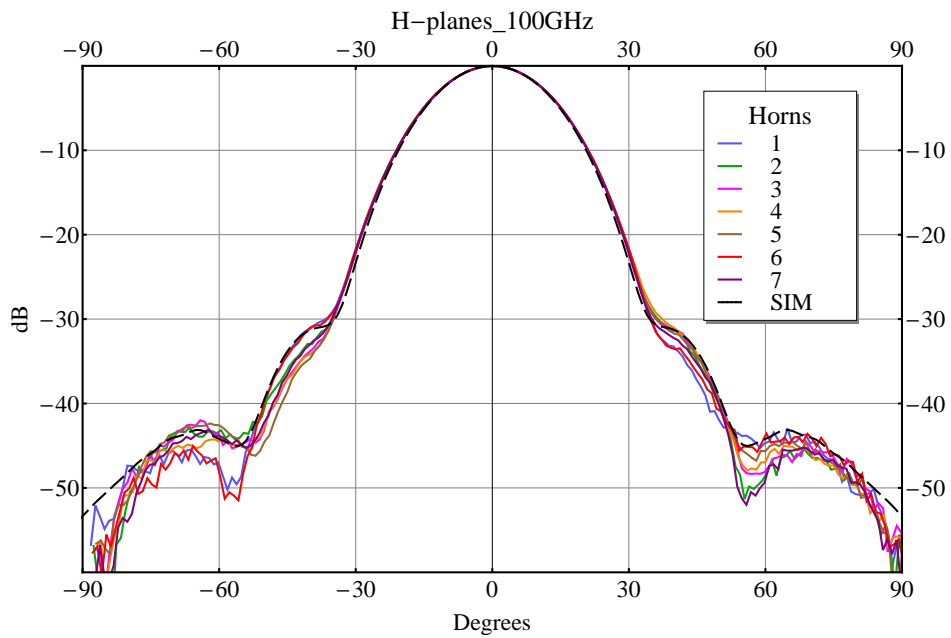


Figure 5.31: Comparison of the H-planes, @100 GHz, for all the seven feed-horns with the relative simulation.

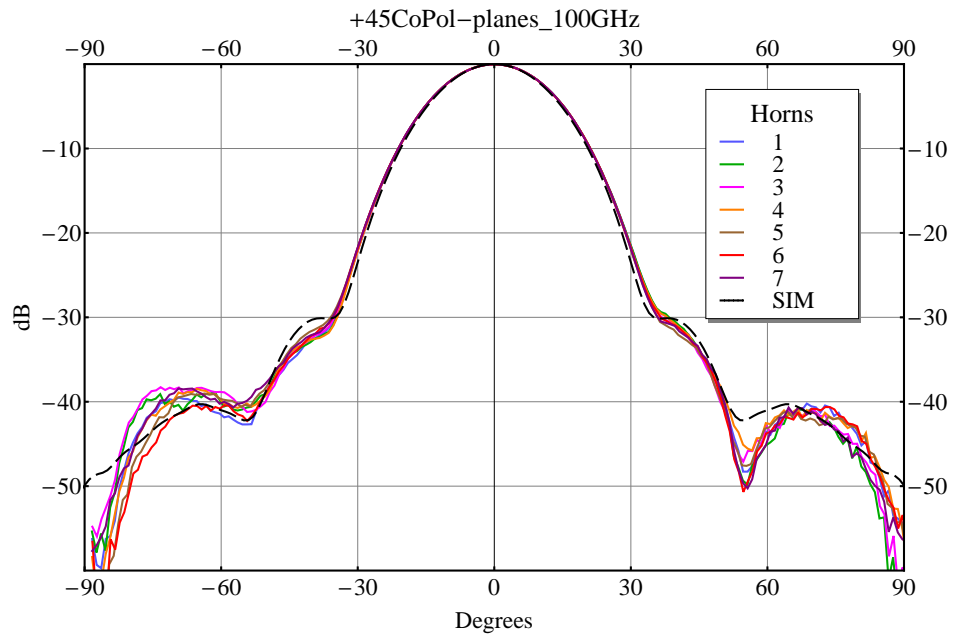


Figure 5.32: Comparison of the +45-planes, @100 GHz, for all the seven feed-horns with the relative simulation.

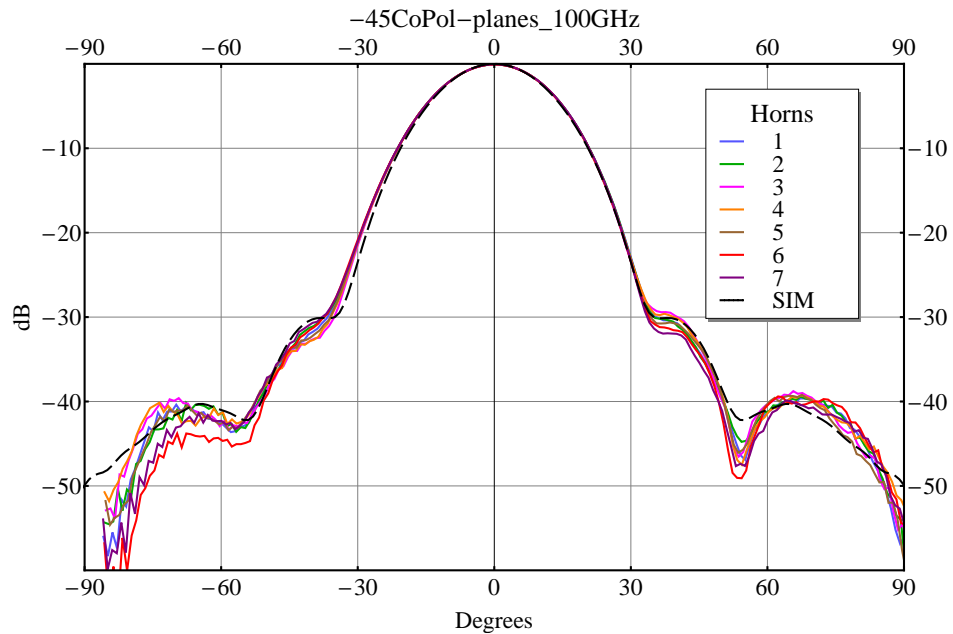


Figure 5.33: Comparison of the -45-planes, @100 GHz, for all the seven feed-horns with the relative simulation.

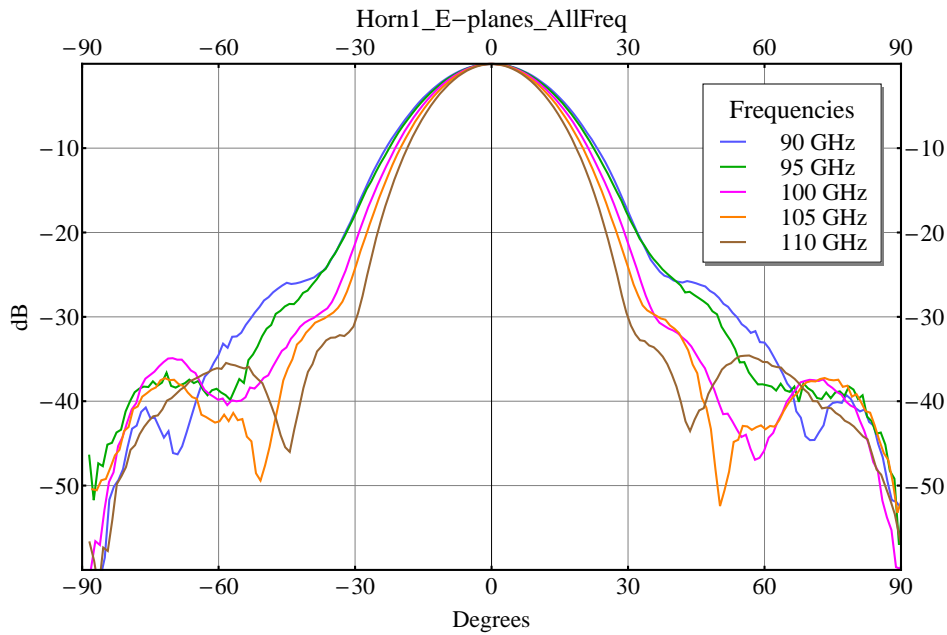


Figure 5.34: Beam pattern of the E-planes for the feed-horn #1 at the five measured frequencies.

with a great (~ 2.5 m tall) motorized positioner inside it, for measuring beam pattern by moving the second receiving/transmitting antenna. Unfortunately when our tests were performed the positioner was out of use and in a blocked side position. Despite the positioner was shielded with apposite material, it constitute an asymmetric element inside the anechoic chamber, whose effects are practically not quantifiable, especially at the high frequencies of the W band. This consideration about the possible asymmetric response of the anechoic chamber are particularly relevant for the cross-polarization measurements, that requires to measure more faint signals with respect to the co-polar measurements. Moreover the co-polar beam pattern suggest a related lower cross-polarization.

Finally it is important to recall that all the simulated beam pattern and performance were obtained for a feed-horn alone, using the ©SRSR software that assumes cylindrical symmetry and hence without considering neither the presence of the surrounding others feed-horns in the different positions nor the hexagonal shape of the array.

The difference between the simulated and measured geometry, do not allow to say that the measured performances are really unexpected. Looking at the Figure 5.30 can be seen that the co-polar E-planes of the horn #4 and

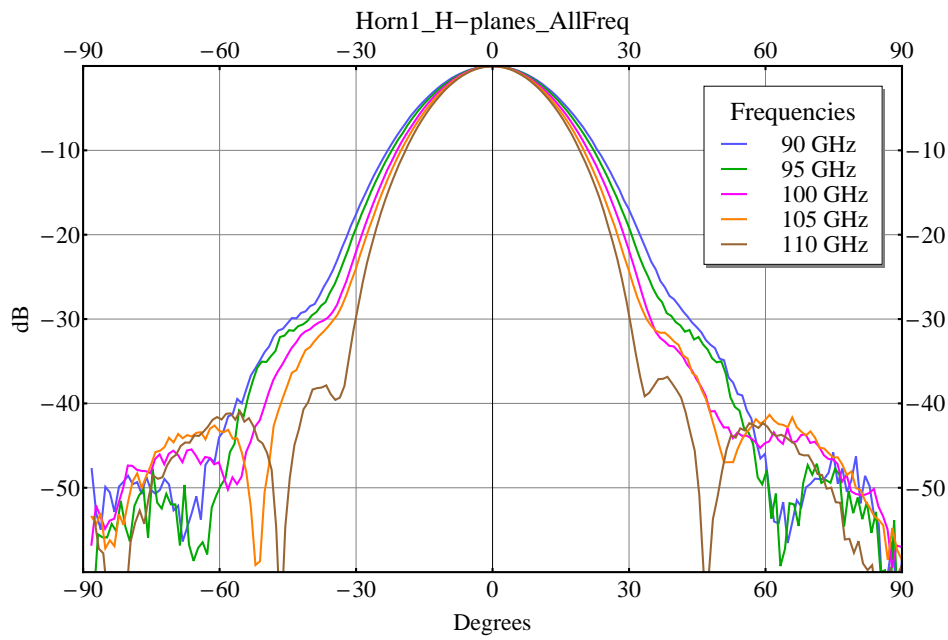


Figure 5.35: Beam pattern of the H-planes for the feed-horn #1 at the five measured frequencies.

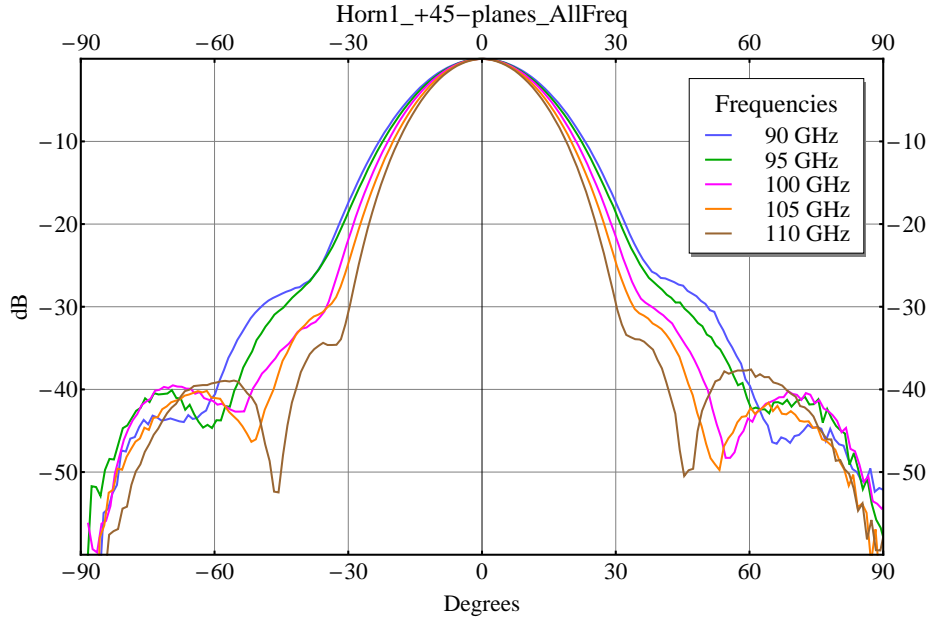


Figure 5.36: Beam pattern of the +45-planes for the feed-horn #1 at the five measured frequencies.

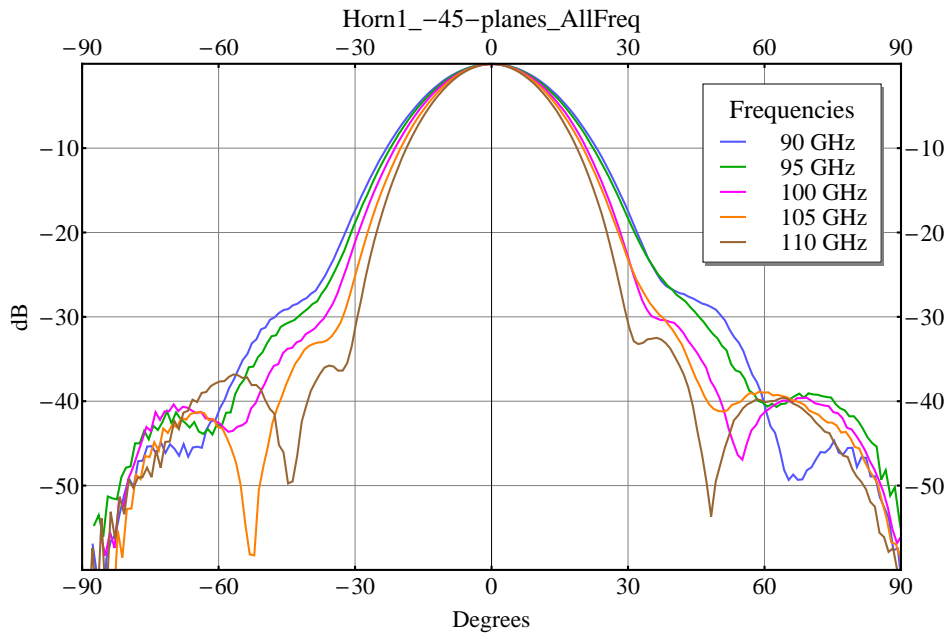


Figure 5.37: Beam pattern of the -45-planes for the feed-horn #1 at the five measured frequencies.

#5 show reflected side-lobes with respect to the #2 and #7. Those pairs of horn, during the E-planes measurements were displaced on the opposite edges of the array (see Figure 5.22). The same apply to the horn #3 and #6 for the H-planes measurements (Figure 5.31). Nevertheless the feed-horn #1, despite being in an unique position at the center of the array, shows (Figure 5.31) the same asymmetries of the feed-horn #6. Moreover always from Figure 5.31 the feed-horn #1 and #6 seem to show a reflected H-plane with respect to the #2 and #7, without relation of symmetry position. To obtain simulated performance more compliant with the real array, a three-dimensional simulating software is necessary, together with an appropriate computing power.

To decouple the eventual manufacturing errors of the array, from the uncertainties on the symmetry response of the anechoic chamber, further analysis are required with a more reliable experimental setup. Then it is currently difficult or impossible to say if and how much the measured beam pattern asymmetries are due to manufacturing errors in the array.

In any case, as explained before in the Fabrication section, for each plate all the feed-horn holes were machined sequentially with the same tool. Furthermore an eventual misalignment of a plate would have the same influence

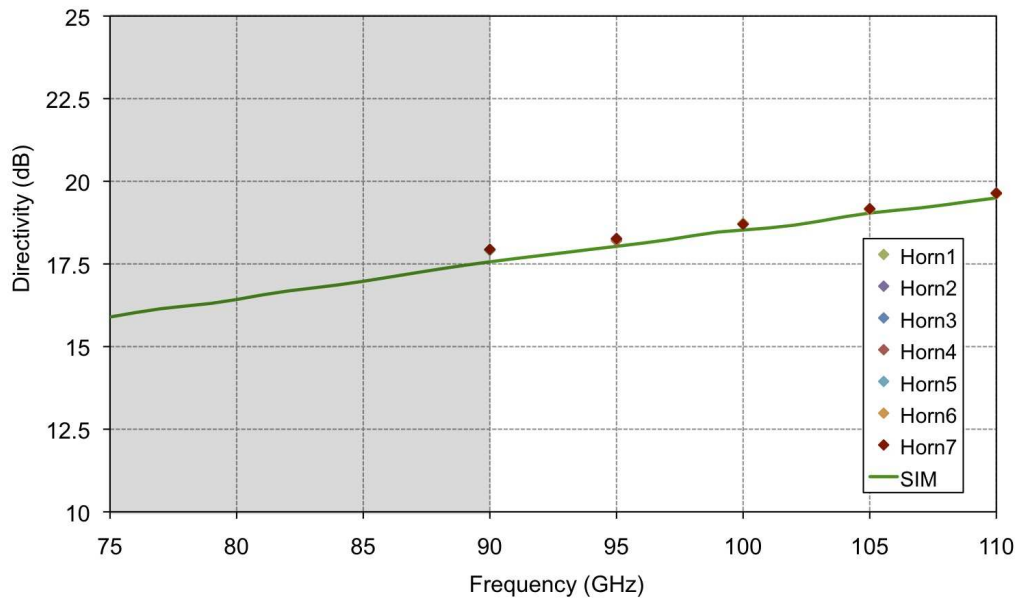


Figure 5.38: Beam pattern of the -45-planes for the feed-horn #1 at the five measured frequencies.

on all the feed-horns. The array of four feed-horns realized with the same technique[30], showed very similar performance on all the feed-horns. In this work the new vacuum clumping system was introduced. This tool can be investigated with regard to its precision, and in particular in the displacement of the vacuum holes of the rubber mask. An insufficient surface of suction on the workpiece can in fact results in insufficient clamping force, allowing the workpiece to slightly move during the working process and introducing fabrication errors. A refinement on the preparation of the vacuum clumping masks could reduce the eventual fabrication errors, obtaining feed-horn with performance even better than those here obtained, that already meet almost all the requirements.

5.4.2 Return Loss

Return Loss measurements are obtained injecting a signal into the feed-horn and measuring the reflected signal. The measurements are performed on the entire band of interest and with the antenna irradiating in the free space.

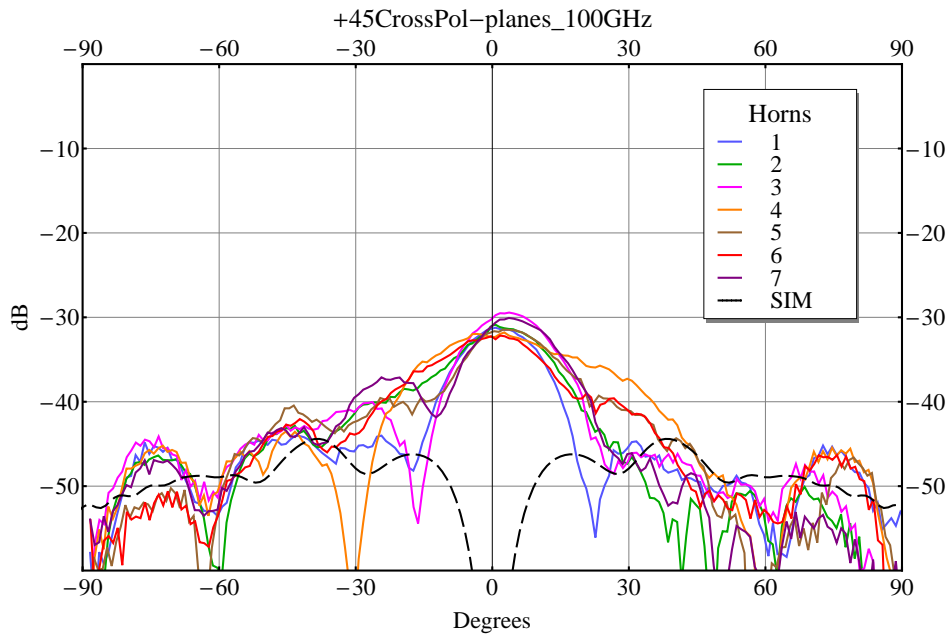


Figure 5.39: Comparison of the +45-Crosspolar-planes, @100 GHz, for all the seven feed-horns with the relative simulation.

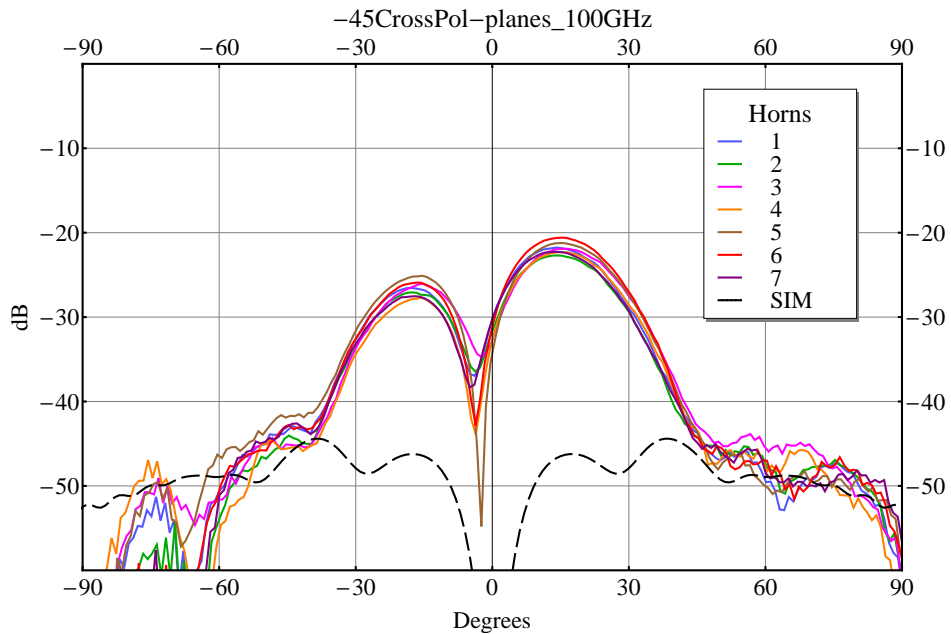


Figure 5.40: Comparison of the -45-Crosspolar-planes, @100 GHz, for all the seven feed-horns with the relative simulation.

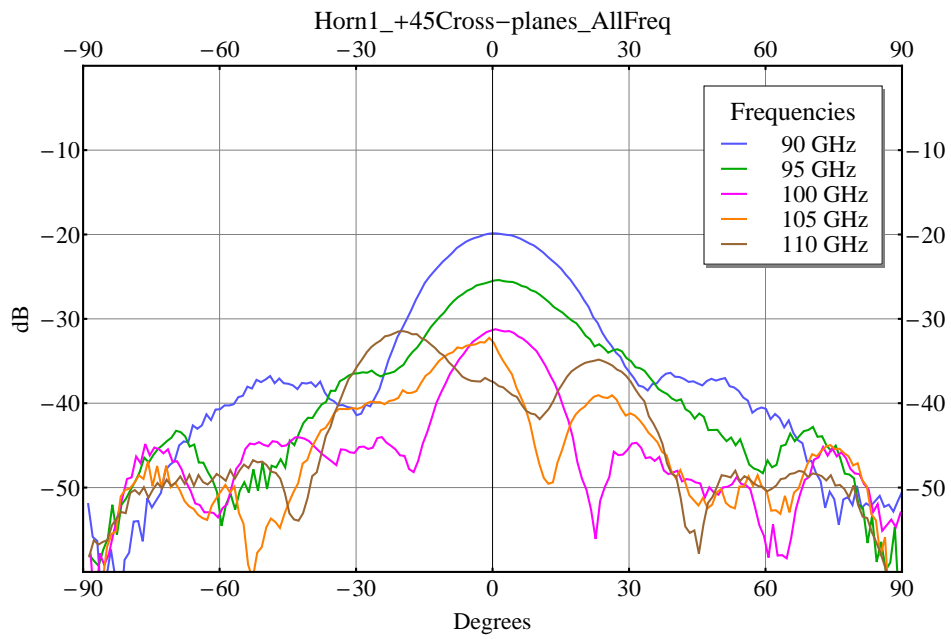


Figure 5.41: Beam pattern of the +45crosspolar-planes for the feed-horn #1 at the five measured frequencies.

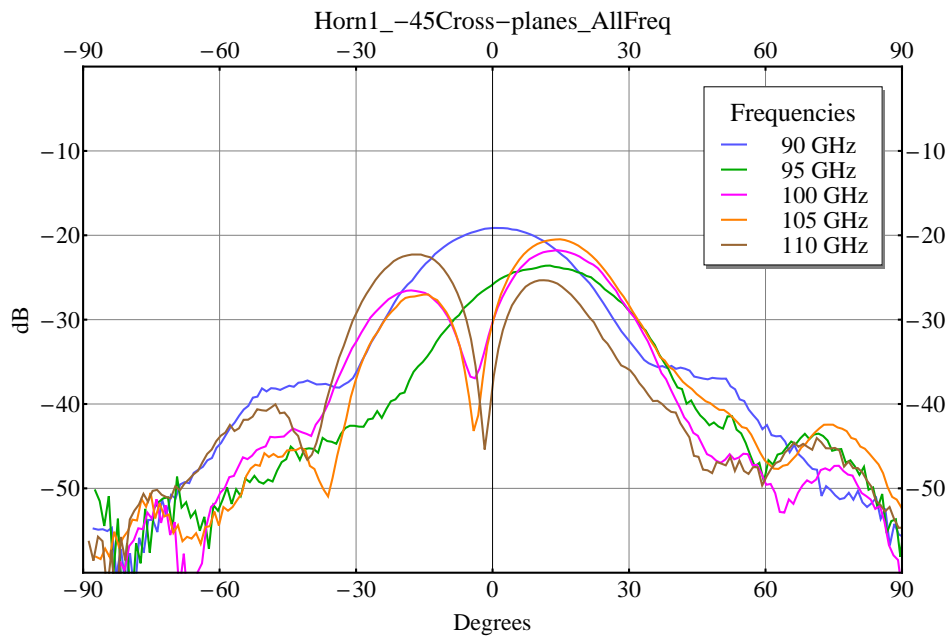


Figure 5.42: Beam pattern of the E-45crosspolar-planes for the feed-horn #1 at the five measured frequencies.

Experimental setup

The experimental setup for the Return Loss measurements of the feed-horn array was a reflectometer composed as below. The signal generator was connected to an isolator, a 10 dB attenuator and a directional coupler. On the principal arm of the directional coupler was connected a straight section of waveguide at which was connected the feed-horn under test. On the side-arm of the directional coupler was connected the receiver with an isolator.

The reflectometer needs to be calibrated, in order to measure the signal reflected by the device under test (DUT) and remove the signals reflected by the components of the reflectometer itself and by the components used to connect the DUT. The calibration is performed attaching, in place of the DUT some standard known components and measuring their reflected signals. For the array prototype return loss measurements the calibration was performed with a variable load, a variable short and a fixed short as the standard known components. Once connected the DUT, the signal reflected by all the others devices is already known by the calibration and then not accounted for. The calibration for the array prototype return loss measurements was performed at the end of the last straight waveguide section, being the last rectangular waveguide interface available for the connection of the calibration components.

The feed-horn array, as visible in Figure 5.21, is not provided with flanges, in order to maintain a certain flexibility of connection. The distance between every pair of feed-horn is in fact of 17.846 mm, smaller than the standard (UG387) flange whose diameter is 20 mm. Then a custom hexagonal thick plate was realized, with seven custom flanges, smaller than the standard, each one provided with a straight circular waveguide section, with the same diameter of the horns waveguides. This custom flanged plate was aligned to the array with the same spindle-system used to align the others plates of the array. The tightening of the flanged plate was realized removing six of the twelve array screws and replacing them with six longer screws, able to be tightened into the array head. In that way the six “original” non-removed screws ensure that no change has occurred in the array geometry.

To adapt the circular waveguide of the feed-horns to the standard WR10 waveguide, necessary for the measurements, a circular to rectangular adapter is required. For time reasons, an already available circular to rectangular (WR10) transition was used, provided with standard flanges. The diameter of the circular side of the transition is 2.98 mm, while the horns waveguides diameter is 2.40 mm. Then a circular to circular adapter was realized to match the two waveguides diameters. Also the adapter was realized with a standard (UG387) flange on the 2.98 diameter side, and the custom reduced

flange on the 2.40 mm diameter side. The waveguides chain to connect the feed-horns was then composed by the non-standard flanged plate, the circular waveguide-flange adapter and the circular to rectangular (WR10) transition. Being the reflectometer calibration performed at the end of the straight waveguide section, those components were not calibrated.

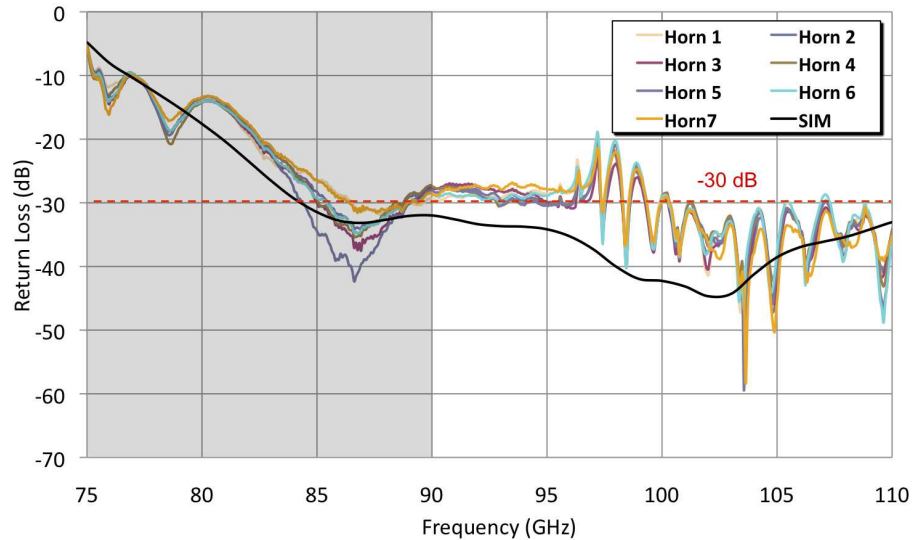


Figure 5.43: Measured return loss of the seven feed-horns, compared with the simulated (black) return loss. The gray region is out of the interested frequency band.

The return loss measurements of all the seven feed-horns are shown in Figure 5.43, compared with the simulated performance. The measurements lie above the simulated performance and, between 95 and 100 GHz, also above the requirement of -30 dB. The effects of the non calibrated components were partially removed filtering the data with the FFT, but this approach is often hard to control. Moreover in Figure 5.44 the feed-horns measured RL and the load termination performance are shown. As visible the feed-horns RL is partially dominated by the load performance, that lie above the feed-horn simulated RL.

Despite the limits of the experimental setup the measured RL are very similar between each others and around the level of -30 dB. To measure the expected RL of the feed-horn an experimental setup with better performance is required, but that is not yet available.

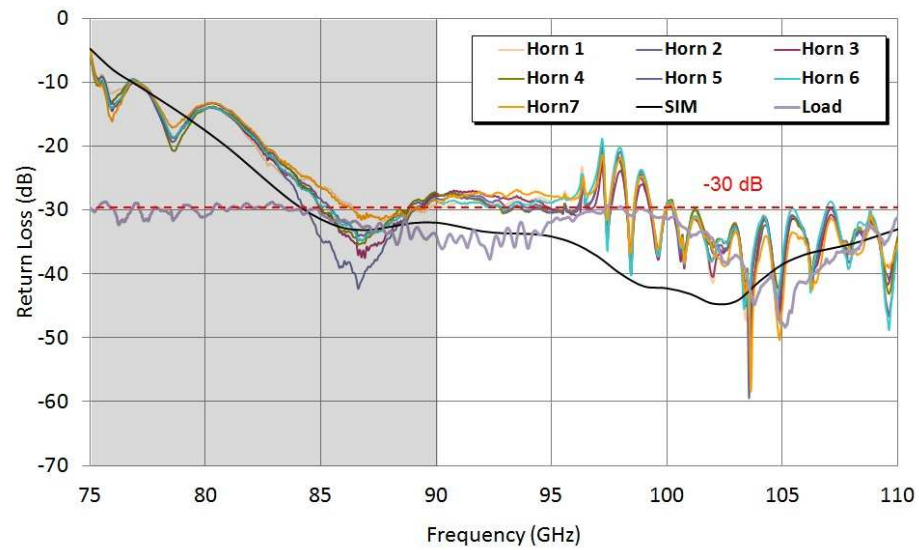


Figure 5.44: Measured return loss of the seven feed-horns, compared with the simulated (black) return loss and the load used for calibration (pink). The gray region is out of the interested frequency band.

Chapter 6

Conclusions

Forty-five years after its discovery, the **Cosmic Microwave Background** radiation is today a very powerful tool of cosmological investigation. Accurate measurements of the CMB temperature anisotropies provide a wealth of information about the Universe history and composition (baryons, dark matter, dark energy). CMB temperature anisotropies have been measured by many ground and balloon experiments as well as by the NASA satellites COBE¹ and WMAP². The third generation ESA satellite Planck³, launched in May 2009, will provide in few years foreground-limited CMB temperature anisotropy measurements and open the path to accurate measurements of CMB polarization anisotropies, that constitutes the target of future of CMB experiments.

The CMB polarization, generated by Thomson scattering of radiation with quadrupolar anisotropy on free electrons, gives direct informations on the last scattering surface, where it is generated. In particular the polarization allows to know when the last scattering occurred and the epoch of reionization, caused by the ignition of the first stars, when the photons were re-scattered. The CMB polarization can be predicted by the acoustic oscillation scenario of the Hot Big Bang model, in which the large scale structures are originated from primordial fluctuations by gravitational instability. Detection of the CMB polarization, particularly on small scales, then provides an important check on the acoustic oscillations of the Hot Big Bang model. The polarization brings informations on the different source of quadrupolar anisotropies that generate it. In particular the relative content of tensor and scalar perturbation T/S can be derived. It is related to the energy scale of the inflation epoch, occurred $\sim 10^{-34}$ seconds after the Big Bang [14]. The

¹<http://aether.lbl.gov/www/projects/cobe/>

²<http://map.gsfc.nasa.gov/>

³<http://planck.esa.int>

energy scale of the inflation is at a level of 10^{16} GeV, beyond any particle accelerator that will ever be built on Earth. Complementary informations can be obtained from polarization anisotropies with respect to the temperature anisotropies, breaking the cosmological parameters degeneracies and improving the parameters estimation. Polarization anisotropies can be represented on the celestial sphere by two modes, named E-mode and B-mode, according to their symmetry properties. The detection of B-modes would be a “smoking gun” for the cosmological background of gravitational waves, that are predicted by the Hot Big Bang model [8]. The CMB is just partially polarized, an amount $\leq 10\%$, corresponding to a signal of a fraction of μK . The measurements of the CMB polarization is then very difficult and currently at the beginning [4, 5], requiring great technological efforts for the next generation experiments.

Many experiments are currently planned to accurately measure the CMB polarization. First detection of E-modes and its correlation with the temperature anisotropy was published in 2003 by the DASI collaboration [13], while the most up-to-date measurements come from WMAP [24]. Because only less than 10% of the CMB is polarised, polarisation anisotropies are smaller compared to temperature anisotropies. E-modes, in particular, are at the μK level, while for B-modes the signal is expected to be much weaker and not even well theoretically constrained, although it is not expected to be larger than some fraction of μK [8].

Detection of such small signals call for ultra-high sensitivity instruments, constituted of large detector arrays with hundreds and even thousands of channels. A key element is represented by the availability of high performance antennas which represent the interface between the sky (or telescope) and the receiver. Precision polarization measurements require optical components with highly symmetrical optical response and losses not greater than $\sim 1\%$. Corrugated feed-horns match these requirements and are commonly used in most CMB experiments [cfr. WMAP and Planck].

Typical feed-horns manufacturing techniques include direct machining up ~ 40 GHz, and electroforming at higher frequencies. These methods can be limited by production time and costs when applied to large detector arrays with hundreds of feed-horns, as requested by future CMB polarization experiments. Therefore cheaper and quicker techniques are preferred.

In this work I have realized a prototype of array, composed by seven corrugated -dual profiled- feed-horns in W band (75-110 GHz), realized by means of the “platelet” technique. The platelet technique consists in the overlapping of metal plates with holes of the proper sizes in order to realize the electromagnetic profile of the feed-horns. The platelet technique allows for reduced times and costs with respect to other fabrication techniques, re-

alizing more elements at the same time by drilling several holes in each plate and ensuring adequate precisions, resulting suitable for mass production [30], [31], [32]. Machining feed-horns layers by layers allows to obtain any kind of optimized corrugated profile without difficulties. Besides an entire corrugation, with a tooth and a groove can be realized into each plate. A complex focal surface can be obtained with a series of sub-arrays or modules properly tilted to reproduce the required geometry. Particular care is required in the plate assembly and alignment system and for mass/volume control in order to minimize the weight. Recently the QUIET⁴ experiment started CMB polarization measurements using, for the first time, feed-horn array realized with the platelet technique [25].

The module realized in this work is designed for compactness, lightweight, reliability in cryogenic and space conditions with high electromagnetic performance. The module has an hexagonal shape with a central feed-horn surrounded by the other six elements. This symmetry is the best one for compactness of the single module and also of an array composed of such modules, located as an honeycomb lattice. The 23 Anticorodal plates that compose the module are assembled by twelve Ergal screws, displaced between the feed-horns, in order to ensure compactness and at the same time a uniform distribution of tightening force and pressure on the plates. For the same compactness reasons the assembling screws are tightened directly onto the last plate, that required a particular design, without using nuts and enhancing the compactness. This non-bonded solution, chosen here and in [31] to assemble the module, allows for simple and cheap manufacturing, with respect to bonded solutions as in [32], with the possibility to disassemble the module if needed. An external alignment system was adopted to align the plates. It does not contribute to the prototype weight and do not require extra. In order to reach the maximum compactness and lightweight the mechanical design of the module was optimized with a dedicated software tool, implemented for that purpose. It calculates the minimal and maximal dimensions for the holes on each plate. The prototype was realized with a CNC machine tool at the workshop of the Physics Department-University of Milan.

The prototype was tested for return loss and beam pattern in standard conditions at the “Istituto di Fisica del Plasma-CNR-Milano”. The beam pattern was measured for E, H, $\pm 45^\circ$ co-polar planes and $\pm 45^\circ$ cross-polar planes, at 90, 95, 100, 105 and 110 GHz for all the seven horns, for a total of 210 beam patterns.

Co-polar beam patterns measurements are in good agreement with the

⁴<http://quiet.uchicago.edu>

corresponding simulations and show very good repeatability for all the seven feed-horns at the five measured frequencies. In particular the directivity of all the seven feed-horns, at the five measured frequencies, shown very good agreement with the simulation, with differences <0.1 dB among the feed-horns. Some asymmetries were found on the left first side-lobe of the E-planes beam pattern at the level of -40 dB. These asymmetries need further investigation to be attributed exclusively to the feed-horns, but in any case they result compatible with the requirements.

Cross-polarization beam pattern measurement did not match the requirements, but at the same time they are not compatible with the relative co-polar measured performance. The low (-45 dB) level of expected cross-polarization requires an experimental setup with better performance to be properly measured.

The measured return loss is ≤ 30 dB over the entire 20% bandwidth for all four antennas, matching the requirements. The simulated RL shows a minimum level of -45 dB between 100 and 105 GHz, but the measurements include the RL of the necessary adapting waveguide components that have worst performance. To obtain RL measurements of the feed-horns new measurement, with appropriate setup calibration, would be necessary, in order to exclude the adapting waveguides RL contribution.

Also mechanical, vibrational and thermal performance were simulated by Thales Alenia Space Italia, that participates as main contractor in the ASI contract that funded this work. These simulations show good results in terms of mechanical margin of safety, indicating a possible space readiness for the prototype design and fabricating technology.

These results are very promising for the time and cost-effective mass production of large array of high-performances corrugated feed-horns for future CMB polarization experiments. The design of the realized prototype will be applied for the focal plane of the STRIP instrument on board of the ASI-LSPE experiment. The LSPE experiment is planned to measure the CMB polarization during a long-duration night flight over the Arctic Polar Circle in winter 2014-2015, with a sensitivity better than Planck in the range $\sim 20 < \ell < \sim 100$.

The advantages of this technique and design go beyond its application to CMB measurements and can be exploited in a wide range of mm-wave and sub-mm astronomical instruments. In particular, platelet techniques may prove appropriate for the **Sardinia Radio Telescope**⁵ and for the new generation of large interferometric arrays, such as ALMA⁶, which require high

⁵<http://www.srt.inaf.it/>

⁶<http://www.eso.org/sci/facilities/alma.html>

performance antennas (including polarization properties) over a large number of channels.

Acknowledgments

I would to thanks my PhD Tutor and Coordinator of the PhD school Prof. Marco Bersanelli, from which I'm learning the method and the approach of the researcher. Thank you for trusting in me accepting my tutoring and giving me the opportunity to accomplish this challenging work. The other person that has made possible this work and that I want to thanks is the chief of the Physics Department workshop Francesco Cavaliere, thank you for your helpfulness and for all that you have taught me.

Thanks to Cristian Franceschet that gave me a great help and contribution in this work, in particular for the coding and all the computer helps, but also for the every day support and companionship.

Thanks to Alessandro Simonetto and Ocleto D'Arcangelo of the IFP-CNR-Milano for their helpfulness and the work and time dedicated in the RF measurements.

Thanks to Arnaldo Bonati, Massimiliano Pecora and Luca Pagan of Thales Alenia Space, who collaborated to this work as the prime contractor of the ASI contract I /038/09/0, under which this work was realized.

Bibliography

- [1] W. Freedman et al. May 2001; *Final Results from the Hubble Space Telescope Key Project to Measure the Hubble Constant*, The Astrophysical Journal, Volume **553**, Issue 1, pp. 47-72.
- [2] D. Tytler, J. M. O'Meara, N. Suzuki, and D. Lubin, *Review of Big Bang nucleosynthesis and primordial abundances*, Physica Scripta Volume T, vol. **85**, pp. 12-31, 2000.
- [3] S. Burles, K. M. Nollett, and M. S. Turner, *Big Bang Nucleosynthesis Predictions for Precision Cosmology*, ApJ Lett., vol. **552**, pp. L1-L5, May 2001.
- [4] J. M. Kovac, E. M. Leitch, C. Pryke, J. E. Carlstrom, N. W. Halverson, W. L. Holzapfel; *Detection of polarization in the cosmic microwave background using DASI*, Nature **420**, 772 - 787 (19 Dec 2002).
- [5] E. M. Leitch, J. M. Kovac, C. Pryke, J. E. Carlstrom, N. W. Halverson, W. L. Holzapfel, M. Dragovan, B. Reddall, E. S. Sandberg; *Measurement of polarization with the Degree Angular Scale Interferometer*, Nature **420**, 763 - 771 (19 Dec 2002).
- [6] Fixsen, D. J.; Cheng, E. S.; Gales, J. M.; Mather, J. C.; Shafer, R. A.; Wright, E. L.; *The Cosmic Microwave Background Spectrum from the Full COBE FIRAS Data Set*; Astrophysical Journal **v.473**, p.576, 12/1996.
- [7] J. C. Mather, D. J. Fixen, R. A. Shafer, C. Mosier,² and D. T. Wilkinson, *Calibrator Design for the COBE Far Infrared Absolute Spectrophotometer (FIRAS)*, The Astrophysical Journal, **512**:511-520, 1999 February 20.
- [8] Wayne Hu, Martin White, *A CMB Polarization Primer*, New Astronomy, **2** (1997) 323.

- [9] S. Dodleson, *Modern Cosmology*, Academic Press, Elseiver
- [10] L. Page, G. Hinshaw, E. Komatsu, M. R. Nolta, D. N. Spergel, C. L. Bennett, C. Barnes, R. Bean, O. Doré, J. Dunkley, M. Halpern, R. S. Hill, N. Jarosik, A. Kogut, M. Limon, S. S. Meyer, N. Odegard, H. V. Peiris, G. S. Tucker, L. Verde, J. L. Weiland, E. Wollack, E. L. Wright; *Three Year Wilkinson Microwave Anisotropy Probe (WMAP) Observations: Polarization Analysis*, ApJS, **170**, 335 (2007).
- [11] G. Hinshaw, M. R. Nolta, C. L. Bennett, R. Bean, O. Doré, M. R. Greason, M. Halpern, R. S. Hill, N. Jarosik, A. Kogut, E. Komatsu, M. Limon, N. Odegard, S. S. Meyer, L. Page, H. V. Peiris, D. N. Spergel, G. S. Tucker, L. Verde, J. L. Weiland, E. Wollack, E. L. Wright; *Three-Year Wilkinson Microwave Anisotropy Probe (WMAP) Observations: Temperature Analysis*, ApJS, **170**, 288 (2007).
- [12] Jackson J.D., *Classical electrodynamics* 3ed., Wiley, 1999.
- [13] J.E. Carlstrom, J. Kovac, E.M. Leitch, C. Pryke, *Status of CMB polarisation measurements from DASI and other experiments*, 2003 New Astronomy Reviews **47** 953-966.
- [14] M. Bersanelli, D. Maino, A. Mennella; *Anisotropies of the cosmic microwave background*; Rivista del nuovo cimento, Vol. **25**, N. 9, 2002
- [15] C.L. Bennett et al., *First-Year Wilkinson Microwave Anisotropy Probe (WMAP) Observations: Foreground Emission*, 2003 ApJS, **148** 97
- [16] Benoit, A et al., *First detection of polarization of the submillimetre diffuse galactic dust emission by Archeops*, A&A,**424**, 571-582 (2004)
- [17] Smoot, G.F., et al.; *Structure in the COBE DMR First Year Maps*, 1992 ApJL,**396**, L1
- [18] P. de Bernardis et al.; *A Flat Universe from High-Resolution Maps of the Cosmic Microwave Background Radiation* Nature **404**:955-959,2000
- [19] A. T. Lee et al.; *A High Spatial Resolution Analysis of the MAXIMA-1 Cosmic Microwave Background Anisotropy Data*; 2001 ApJ **561** L1
- [20] Leitch et al.; *Experiment Design and First Season Observations with the Degree Angular Scale Interferometer*; 2002 ApJ **568** 28

- [21] A. Kogut et al. *First-Year Wilkinson Microwave Anisotropy Probe (WMAP) Observations: Temperature-Polarization Correlation*; 2003 ApJS **148** 161
- [22] A. C. S. Readhead et al.; *Polarization Observations with the Cosmic Background Imager*; Science, Vol. **306** no. 5697 pp. 836-844
- [23] F. Piacentini et al.; *A measurement of the polarization-temperature angular cross power spectrum of the Cosmic Microwave Background from the 2003 flight of BOOMERANG* Astrophys.J.**647**:833-839,2006
- [24] Jarosik N., et.al., *Seven-Year Wilkinson Microwave Anisotropy Probe (WMAP) Observations: Sky Maps, Systematic Errors, and Basic Results* 2011, ApJS, **192**, 14
- [25] QUIET Collaboration; *First season QUIET Observation: measurements of CMB Polarization Power Spectra at 43 GHz in the multipole range $25 \leq \ell \leq 475$* ; Astrophys.J. **741**:111, 2011.
- [26] Chiang, H. C. et al.; *Measurements of Cosmic Microwave Background Polarization Power Spectra from two years of BICEP data*; 2010, ApJ, **711**, 1123
- [27] The LSPE collaboration; *The Large-Scale Polarization Explorer (LSPE)*; 2012, in preparation
- [28] Ludwig, A.; *The definition of cross polarization* Antennas and Propagation, IEEE Transactions on, Vol. **21**, Issue 1. 1973.
- [29] Clarricoats P.J.B. and Olver A.D.; *Corrugated horns for microwave antennas* IEE Electromagnetic Wave Series 18. Peter Peregrinus Ltd.
- [30] F. Del Torto et al.; *W-band prototype of platelet feed-horn array for CMB polarisation measurements*, 2011 JINST **6** P06009
- [31] Miikka Kangas, Keith Copsey and Philip Lubin; *A Modular 100-GHz High-Gain Scalar Corrugated Nonbonded Platelet Antenna*, IEEE Antennas and Wireless Propagation Letters, **Vol.4**, 2005.
- [32] J. Gundersen, E. Wollack; *Millimeter-wave Corrugated Platelet Feeds*, Journal of Physics: Conference Series 2009, **155** 012005.
- [33] A. Gregorio et al.; *Planck LFI User Manual Document*; **PL-LFI-PST-MA-001**, August 2008.

- [34] L. Pagan; *Analisi termica e strutturale di una schiera di Feed-Horn*; **TASI-TECNOMM-DEL03**, Gen 2008.
- [35] *Space engineering - Threaded fasteners handbook*; **ECSS-E-HB-32-23A**, April 2012.